JAERI-Research
97-045

STUDY OF DENSITY FLUCTUATION IN L-mode AND H-mode PLASMAS ON JFT-2M BY MICROWAVE REFLECTOMETER

August 1997

Kouji SHINOHARA

日本原子力研究所
Japan Atomic Energy Research Institute

本レポートは，日本原子力研究所が不定期に公刊している研究報告書です。
入手の問合わせは，日本原子力研究所研究情報部研究情報課（〒319-11 茨城県那珂郡東海村）あて，お申し越しください。なお，このほかに財団法人原子力弘済会資料センター（〒319-11 茨城県那珂郡東海村日本原子力研究所内）で複写による実費頒布をおこなっております。

This report is issued irregularly.
Inquiries about availability of the reports should be addressed to Research Information Division, Department of Intellectual Resources, Japan Atomic Energy Research Institute, Tokai-mura, Naka-gun, Ibaraki-ken 319-11, Japan.

編集兼発行　日本原子力研究所
印　　刷　㈱原子力資料サービス

JAERI－Research 97－045

Study of Density Fluctuation in L-mode and H-mode Plasmas on JFT-2M by Microwave Reflectometer

Kouji SHINOHARA

Department of Fusion Plasma Research
Naka Fusion Research Establishment
Japan Atomic Energy Research Institute
Naka-machi, Naka-gun, Ibaraki-ken

(Received June 2, 1997)

We propose the model which can explain the runaway phase. The model takes account of the scattered wave which is caused by the denstiy fluctuation near the cut-off layer. We should take a new approach instead of the conventional phase measurement in order to derive the information of the density fluctuation from the data with the runaway phase. The complex spectrum and the rotary spectrum analyses are useful tools to analyze such data.

The density fluctuation in L-mode and H-mode plasmas is discussed by using this new approach. We have observed that the reduction of the density fluctuation is localized in the edge region where the sheared electric field is produced. The fluctuations in the range of frequency lower than 100kHz are mainly reduced.

Two interesting features have been observed. One is the detection of the coherent mode around 100kHz in H-mode. This mode appears about 10 ms after L to H transition. The timing corresponds to the formation of a steep density and temperature gradient in the edge region. The other is the enhancement of the fluctuations with the frequency higher than 300kHz in H-mode in contrast to the reduction of the fluctuations with the frequency lower than 100kHz.

Doctral Thesis Accepted in Department of Physics, Graduate School of Science, University of Tokyo in December, 1996.

The Doppler shift is observed in the complex auto-power spectrum of the reflected wave when the plasma is actively moved. We have confirmed that the movement of the plasma is appropriately measured by using the low pass filter. The reflectometer can be used to measure the density profile by using a low pass filter even when the runaway phase phenomenon occurs.

Keywords: Reflectometer, Density Fluctuation, Scattering, Complex Amplitude

JFT-2Mにおけるマイクロに波反射計を用いた L-mode, H-mode プラズマ時における密度振動の研究

日本原子力研究所那珂研究所炉心プラズマ研究部
篠原　孝司

（1997年6月2日受理）

反射計におけるrunaway phaseに関する実験事実が密度揺動による散乱で説明できるとするモデルを考案した。runaway phaseを含んだ反射計のデータの解析には複素スペクトル，複素相関を利用すべきである。また，散乱波の複素振幅における回転のイメージを見るのに回転スペクトルも有効である。

これらの解析法を用いてLH遷移時の計測を行った。まず，LH遷移による密度揺動の減少は，主として100kHz程度以下であり，プラズマ端に局在していることがわかった。この領域ではLH遷移の際，径方向電場のシアができることが居田らの荷電交換分光計測により確認されている。

これまでに報告されていない新しい二つの実験事実も観測された。一つはH-mode後しばらくして100kHz付近にcoherentなモードが観測されたことである。モードが発生する時刻は電子密度および電子温度のプロファイルがプラズマ端で急峻になる時刻に対応している。このcoherentなモードはプローブや磁気プローブにおいても観測されており，密度あるいは温度の非一様性によって駆動されるグローバルなMHD揺動と考えられる。もう一つはH-mode時に前述の100kHz程度以下の揺動が抑制されるのとは対照的に300kHz程度以上では揺動が増えているのが観測されたことである。これらは今後の解析によりH-mode時の物理現象に新たな知見を与えると思われる。

また，プラズマを垂直コイルにより動かしたときに反射層の動きが信号の複素スペクトルにDoppler shiftとして観測された。このことは信号の低周波成分のみを用いるとプラズマの散乱の影響を抑えることができることを意味し，数値的なlow pass filterを使用することで反射層の動きを測定することができる。

那珂研究所：〒311-01　茨城県那珂郡那珂町向山801-1
東京大学大学院理学系研究科により博士論文として受理された。（1996年12月）

Contents

目　　次

1. Introduction

1.1 Tokamak

The charged particle undergoes cyclotron motion along a magnetic field line. It seems that the plasma is confined in the system with a closed magnetic field line. However, a simple torus consisting of only closed toroidal magnetic field lines can not confine a plasma, as the curvature drift and the gradient B drift of the particles produce a charge separation which generates an electric field and this electric field drives an outgoing plasma flow across the toroidal field, where B means the magnetic field (see Appendix A about the terms of the coordinate). This process can be suppressed by introducing a poloidal magnetic field in the plasma. The resultant magnetic field line (composed of toroidal and poloidal components) is helically twisted and the particles moving along the field lines cancel the charge separation, so that the electric field does not grow [1].

Tokamak is one such toroidal confinement system and was proposed by the researchers in the Soviet Union in the 1950's [2]. The poloidal field of the helical magnetic field is produced by a plasma current flowing along the toroidal field in the tokamak system. The toroidal current is driven by magnetic induction using the electric transformer. The toroidal current also heats the plasma by ohmic heating.

1.2 Transport of Plasma

The observed electron energy confinement time is much less than the confinement time predicted by neoclassical transport theory in torus plasma. This phenomenon is called anomalous transport. The understanding of the physics of the anomalous transport and the physics of the control of the transport is one of the most important topics in the physics of the magnetic confined plasma. It is believed for a long time that the anomalous transport across the magnetic field lines may be due to electrostatic turbulence associated with pressure gradient or due to magnetic turbulence [3,4].

For example, the particle flux Γ by the electrostatic turbulence is expected to be described as,

$$\Gamma = \left\langle \tilde{n}\tilde{V} \right\rangle, \tag{1.1}$$

where $\tilde{n}$ is the density fluctuation, $\tilde{V}$ is the fluctuation of the flow of the plasma. It is considered that $\tilde{V}$ is determined by the electrostatic turbulence such as the drift wave

and can be described by $\tilde{V} = \tilde{E}/B$

Improved confinement regimes have been discovered such as H-mode [5], IOC (Improved Ohmic Confinement) [6], High β_p mode [7], VH-mode [8], NS (Negative Shear) mode [9], ERS (Enhanced Reversed Shear) mode [10] and their hybrid [11]. These are categorized by the way of the operation and their characteristic parameters. The source and mechanism of the transport are not yet understood. A leading candidate for the transport mechanism is low amplitude microturbulence in the plasma driven by electrostatic instabilities such as drift waves. These instabilities manifest themselves as localized fluctuations of physical quantities such as density, potential, and temperature in the plasma. Most of the transport theories assume that transport is determined by the local physical quantities. These are deduced by solving the equations whose parameters are homogeneous in the narrow region in comparison with the scale length of the global parameter. However some experimental results show that the transport changes globally in a very short time. It is a question whether the local or global physical quantities describe the mechanism of the transport. Thus it is important to measure the physical quantities with good spatial and time resolution in order to test the current theories as well as to construct a more appropriate and sophisticated theory. We must identify the drive and suppression mechanisms responsible for tokamak microturbulence in order to control turbulence and transport.

Presently the measurements with good spatial and time resolution are limited to the very edge or outside the separatrix [1] in a hot fusion plasma. However the recent topics of fusion plasmas relating to the enhanced confinement modes such as H-mode, ERS require a detailed measurement of the main hot plasmas.

Despite many observations made with wave scattering techniques, there exists a pressing need to develop a means of measuring plasma density fluctuations at longer wavelengths in the hot core plasma of tokamaks. Detailed studies with microwave scattering on large tokamaks indicate that the integrated fluctuation amplitude increases monotonically with decreasing wave number, and the bulk of the power spectrum is concentrated around low values of $K_\perp$, where $K_\perp$ is the component of the wave number perpendicular to the toroidal field [3]. In addition, nonlinear theories of instability-driven plasma turbulence indicates the need to determine the long-wavelength characteristics of the turbulent spectrum in order to have a clear understanding of the resulting transport.

1.3 L-mode and H-mode Plasmas

Ohmic heating is used as the source of initial heating in tokamaks. The resistivity η of the plasma decreases as the electron temperature T_e increases ($\eta \propto {T_e}^{-3/2}$), so that

[1] see Fig. A.2 in Appendix A

ohmic heating is limited to $T_e = 1 - 2$ keV range [1,12].

The ignition temperature ,which is the temperature at which the heating power by α-particle produced by the fusion reaction is equal to the power losses from plasma, is more than about 30 keV, therefore additional heating is required. Presently two methods are used. One is the injection of the wave such as ECRH (Electron Cyclotron Resonance Heating) [13], ICH (Ion Cyclotron Heating) [14]. The other is NBI (neutral beam injection) heating [15].

The energy confinement time

$$\tau_E \equiv W/(P_{in} - dW/dt)$$

initially became shorter than that for ohmic discharge when the additional heating was applied. Here P_{in} is the input power and W is the stored energy. This state of low confinement is now called L-mode. It seemed difficult to achieve the fusion plasma because of L-mode. In 1982, however, the ASDEX group [5] discovered a new state in which the energy confinement time was as long as in ohmic discharge. This state is called H-mode. It is observed that there exits a power threshold of NBI on the L to H transition. The power of NBI was below the threshold in the initial experiments.

The experimental signatures of the H-mode are a reduction in the H_α light emission, a decrease in edge density fluctuation levels, an increase in edge density and temperature gradients, increment in bulk energy and particle confinement times, and changes in the radial electric field profile [16–20].

The H-mode has aroused many experimental and theoretical interests. Now the H-mode is obtained not only in tokamaks, but also in the helical devices and the mirror devices. The observed bifurcation structure is explained in connection with the change of the edge electric field structure by Ito et al. and Shaing et al. [21,22]. The suppression of the microturbulence by the velocity shear is considered as the mechanism of the H-mode plasma [23]. The suppression of the microturbulence by the velocity shear is derived from the two-point evolution equation. It is considered that the sheared flow originates in the shear of the electric field and the flow is a $\boldsymbol{E} \times \boldsymbol{B} / B^2$ drift motion.

It is considered that the cause of H-mode exists in the region of $0.8 \lesssim r/a \lesssim 1$, where a is the minor radius. Thus information with good resolution of interior region of the plasma is needed.

1.4 Reflectometer

Langmuir and magnetic probes are the most popular diagnostic to investigate plasmas. Several kinds of probes can measure density, temperature, potential and magnetic field. They also have a good time and spatial resolution [20, 24, 25]. However they are applied

only to the plasma edge or the scrape-off layer as they suffer damages in hot plasmas and contaminate the plasmas.

Another effective diagnostic, the laser or microwave scattering is used for measuring wavenumber spectrum of the fluctuations in the core region [26–30]. This method revealed that the fluctuation increases as its wavelength becomes longer. However, the scattering method is unsuitable for the investigation of fluctuation with long wavelength ($\gtrsim$ 5cm), because such a measurement of small angle scattering needs large scattering volume as a result of which the spatial resolution reduces.

BES (Beam Emission Spectroscopy) can measure long wavelength density fluctuations and obtain K_θ and K_r spectrum of the density fluctuation simultaneously in the core plasmas [31, 32]. This method is attractive but the other diagnostics can suffer from the fact that a beam is used in order to acquire sample volume and the relatively large port is necessary to obtain the good time and spatial resolution because the emission power is small.

HIBP (Heavy Ion Beam Probe) [33] is also a powerful diagnostic. This measures density and potential fluctuations with the good time and spatial resolution. The drawback is that the acceleration system to inject the beam into the high magnetic field becomes very big and the implementation is difficult. For example, the beam energy of $\sim$ tens MeV is needed when the magnitude of the magnetic field is more than 5 T and the radius of the plasma is about 2 m.

Microwave reflectometry is thus one of the promising methods for measuring the radial density profile and/or the radial local fluctuations with long wavelength with high time resolution in the core plasmas as well as at the edge. Reflectometry is a technique based on the radar principle, with a response mainly sensitive to the plasma regions where the microwave are reflected. This method has been intensively used for ionospheric studies. The plasma density can be probed internally from the edge to the bulk plasma as the zone where reflection occurs depends on the local plasma density and can be varied simply by changing the incident wave frequency. The plasma is not contaminated as the probe wave of the reflectometer is a microwave with power of less than mW order. The microwave reflectometry is quite a simple diagnostic system and have easy access to the plasma. There is only the antenna, the vacuum window and the wave guide from the plasma to the wave detection system. The size of these components is a few centi-meters. This accessibility will prove to be useful in the next-step experimental reactor which will have many components such as the blankets, the radiation shield, the cryostat vessel and so on.

Reflectometry has thus become a commonly used diagnostic and the results and problems have already been reported [34, 35]. So here we review the reflectometer measurements in fusion devices.

1.4.1 Principle of Reflectometer

Reflectometry is a technique based on the radar principle. The relative movement of the cut-off is deduced from the change of the phase difference between the reference wave and the reflected wave (Fig. 1.1). The phase difference is computed by solving the wave equation [36, 37] . Here we use the one-dimensional equation,

$$\frac{d^2E}{dR^2} + \varepsilon k_0^2 E = 0. \tag{1.2}$$

The WKB solution of this equation is

$$E(R,t) = E_0 \exp(i\omega_0 t + i(k_0 \int^R \sqrt{\varepsilon} dR + \pi/4)), \tag{1.3}$$

where $\omega_0 = 2\pi f_0$ is a frequency of the launched wave. The round-trip phase difference is expressed by

$$\varphi(f_0) = 2k_0 \int_{R_{cut-off}}^{R_{antenna}} \sqrt{\varepsilon} dR + \pi/2. \tag{1.4}$$

Here k_0 is a wavenumber of the launched wave, $R_{antenna}$ is the position of the antenna, $R_{cut-off}$ is the position of the cut-off layer and ε is the dielectric constant. The dielectric constant differs for the O-mode ($\boldsymbol{B}_T \parallel \boldsymbol{E}$) and X-mode ($\boldsymbol{B}_T \perp \boldsymbol{E}$).

$$\varepsilon_O = 1 - \frac{f_p^2}{{f_0}^2} : \text{O-mode.} \tag{1.5}$$

$$\varepsilon_X = 1 - \frac{f_p^2}{f^2} \frac{{f_0}^2 - f_p^2}{{f_0}^2 - f_p^2 - f_{ce}^2} : \text{X-mode,} \tag{1.6}$$

$$f_p = (n_e e^2/\varepsilon_0 m_e)^{1/2}/2\pi, \tag{1.7}$$

$$f_{ce} = eB/2\pi m_e, \tag{1.8}$$

where ε_0 is the permittivity of vacuum. The wave is reflected at the cut-off where $\varepsilon = 0$.

In the O-mode case, the cut-off exists at the density,

$$n_e(R_{cut-off}) = n_c \equiv \frac{4\pi^2 \varepsilon_0 m_e f^2}{e^2}. \tag{1.9}$$

The density profile is determined by solving the Eq. 1.4. In O-mode, it is solved by using Able inversion,

$$R_{cut-off} = \frac{c}{\pi} \int_0^{f_{cut-off}} \frac{1}{2\pi} \frac{d\varphi}{df} \frac{df}{\sqrt{f_{cut-off}^2 - f^2}} \tag{1.10}$$

But in the X-mode case, the absolute position of the cut-off is determined by solving Eq. 1.4 [38].

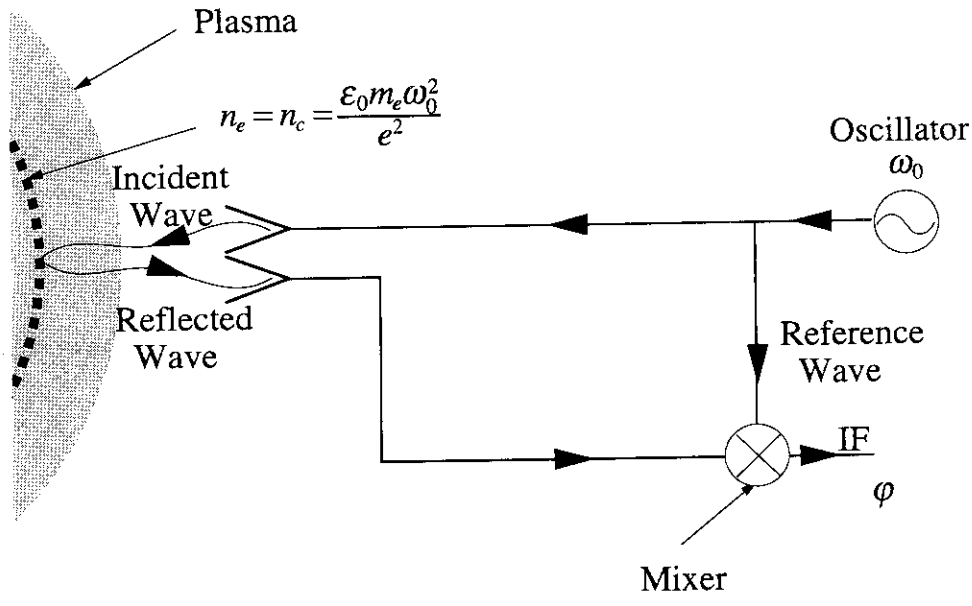

Figure 1.1: Principle of reflectometer

The relation between the displacement of the cut-off layer, $\Delta R_{cut-off}$, and the change of the phase difference between the reflected wave and the reference one due to the displacement of the cut-off layer, $\Delta\varphi$, can be approximated as follows:

$$\Delta R_{cut-off} = \frac{c}{4\pi f\bar{\mu}}\Delta\varphi, \tag{1.11}$$

$$\bar{\mu} \equiv \frac{1}{R_{antenna}-R_{cut-off}}\int_{R_{cut-off}}^{R_{antenna}}\sqrt{\varepsilon(f,R)}dR, \tag{1.12}$$

where $\bar{\mu}$ is referred as the mean refractive index. A value of $\bar{\mu}=0.6$ can be used in our cases [36]. When $L_n^{-1}=\frac{1}{n_e}\frac{dn_e}{dr}$ at the cut-off layer can be considered to be constant, local density fluctuations at the cut-off layer, $\tilde{n}_e/n_e$, can be expressed as

$$\frac{\tilde{n}_e}{n_e} = \frac{c}{4\pi f\bar{\mu}L_n}\Delta\varphi. \tag{1.13}$$

Local density fluctuations $\tilde{n}_e/n_e$ at the position of cut-off layer is able to be estimated by the measurement of $\Delta\varphi$.

In this way, the relative positions of the cut-off layers with the different densities can be measured and the density profile can be reconstructed if the source frequency is swept. Alternatively, movements of the cut-off layer with a specific density can be measured if the source frequency is held constant.

1.4.2 Profile Measurement

We need an accurate profile of the physical quantity such as temperature and density to understand the turbulence because the inhomogeneity becomes the driving source of the turbulence such as a drift wave. The density profile can be determined by using Langmuir probe, interferometer and Thomson scattering method. Probe measurement is difficult in the hot plasma; namely inside separatrix. The interferometer has a poor spatial resolution because it measures the line integrated value. (Multichannel interferometer can improve the spatial resolution by using Abel inversion. Abel inversion needs the assumption of the poloidal symmetry.) It is difficult to measure the time evolution with the short time interval, $\lesssim$ 100 ms, by using Thomson scattering method. The reflectometer has advantages about these points. Since the first data of TFR (the Tokamak of Fontenay aux Roses) was presented [39], many researchers installed the reflectometer in order to measure the density profiles [37,38,40–58].

Most of the reflectometers have used BWO (Backward Wave Oscillator) or YIG (Yttrium-Iron-Garnet) as the swept oscillator. Some reflectometers use IMPATT (Impact Avalanche Transit Time) oscillator [53], HTO (Hyperabrupt Varactor Tuned Oscillator) [59], which can be swept faster. It is necessary to sweep the frequency in the shorter

time than the typical time scale of the density fluctuation because the phase is disturbed by the fluctuations.

The phase can be obtained in many different systems:

In the case of FM (Frequency Modulation) radar technique, the frequency is swept linearly and the round trip delay is converted to an easily measured beat frequency, so that this technique can be called self-modulated heterodyne [41]. The change of phase of the wave with the beat frequency is measured. In this system the reference wave can be obtained in three ways: The first way is to use the delay line which has the same length with the total path length of the way through which the signal wave goes and comes back. The second way is to tune the length of the waveguide so as to make the beat frequency equal to the sweeping frequency. The third way is to use another oscillator whose frequency is same with the beat frequency in the absence of plasma. If we use the beat frequency of such a no plasma condition as the reference, we do not need the reference wave and can apply the digital complex demodulation (CDM) analysis software [56]. In the case of a two-frequency reflectometer, the reflectometer launches two different frequency signals into the plasma and then measures the difference of their individual phase delays after reflection from the plasma [48]. These detection method is homodyne which consists of one oscillator.

In the heterodyne system, the change of phase of the wave whose frequency is equal to the frequency difference between the main oscillator and the local oscillator is measured. and the signal-to-noise ratio increases because the power of the reference wave can be large by using the local oscillator. The system needs the oscillators which produce the frequency difference with high accuracy and stability. However, it is difficult to obtain broadband oscillators which satisfy the condition. Thus four types of approaches are used in order to use the heterodyne detection system in the wide range of frequency: The first one is a multichannel reflectometer [49], in which the frequency is swept but the range is narrow. We can easily use the conventional heterodyne detection in each channel. The profile is reconstructed by interpolating the each group delay. The second one is to use a system with multipliers which make harmonics of the fundamental frequency of the oscillator with high accuracy [59]. The third one is a feedforward tracking system. This system consists of multiple heterodyne systems. The oscillator with the frequency of the incident wave , $\gtrsim$ tens GHz, need not have very high accuracy because the wave with this frequency is downconverted by the oscillator with the lower frequency, $\lesssim$ a few GHz, which has a high accuracy [60]. This oscillator with the lower frequency is easily available. The fourth one is a AM (Amplitude Modulation) reflectometer. The envelope whose frequency is same with amplitude modulation is detected by a diode detector at the last stage. Before this stage, the local oscillators can be added to use the heterodyne

detection system [61].

We can reconstruct the density profile if we have obtained the phase using one of the above systems. However the fluctuations disturb the measured phase and the reconstruction is not straightforward. Usually the reconstruction involves iterative approaches in order to measure the "mean" density profile and needs long computing time. Sanchez et al. [50] proposed to use a Neural Network algorithm. Neural Networks need a long computing time for the training process but once that stage is over they can be used for reconstruction with a reduced number of operations.

The system mentioned above measure the phase difference. Another system which is based on quite a different concept is the pulse radar technique [62–67] . The concept of this method is similar to the time-of-flight measurement. The measured quantity is the time which the pulse takes to go and come back. There are two ways of measuring density profile by this method. One way is via a multichannel system [66]. The pulse is produced by turning the microwave oscillator on during a short time, $\sim$ 500 ps. The cut-off layer is determined by the frequency of the microwave oscillator. The other way is to use an ultrashort pulse, $\sim$ 2 ps [65]. Such an ultrashort pulse contains many Fourier components. Each Fourier component of the incident wavepacket is reflected from a different cut-off layer. By separating the different frequency components of the reflected wavepacket and obtaining the time-of-flight measurement for each component, the density profile can be determined with just one source and a single set of measurements.

Results of the density profile measurements by the reflectometer are listed below: Bottollier-Curtet et al. have observed that the application of the LHCD results in a peaking of the profile due to an increase of the density near the magnetic axis [38]. Wagner et al. show the time evolution of the density profile of L-mode and ELM [16]. Doyle et al. show the density profile of OH, L-mode, H-mode plasmas [47]. Sips et al. show the effect of gas-puffing on the density profile [49]. Sips et al. and Kim et al. show the time evolution of the density profile throughout the L to H transition [49,56]. Skibenko et al. and Hirsch et al. report the results of the Stellarator which has a complex magnetic field [51,58]. In such a condition, both the O-mode and X-mode reflected waves can exist. Hirsch et al. also show the profile of an ECRH plasma [58]. Most reflectometers have their antenna at only low field side because of the accessibility. Manso et al. show asymmetry in the behavior of the profile when the MARFE occurs [57].

1.4.3 Density Fluctuation Measurement

Density fluctuation has been measured by using reflectometer [43,46,58,66,68–85] . There are two major approaches to measure the profile of the density fluctuation. One

is a multichannel arrangement and the other is a broadband step-by-step frequency-swept arrangement. The former is more advantageous as regard the time resolution and the robustness for the spurious microwave production coming from the various microwave components as each channel can be optimized. However its weakness lies in the cost and the reduction of the launched power because of the character of the microwave combiners such as directional coupler. The latter, on the other hand, has exactly the opposite advantage and disadvantages to the former.

Results of the density fluctuation measurements are below:

Hanson et al. report that the simple mixing length estimates are not appropriate in ECH plasma of ATF and that a comparison with a more detailed estimate for the pressure gradient driven resistive interchange turbulence yields reasonable agreement with the results [77].

The comparison with probe or HIBP has been performed [73,77,82] .

Hamberger et al. have demonstrated the existence of electrostatic fluctuations whose amplitude and spectra can explain the observed anomalous particle loss [69]. Many reflectometers report that the observed fluctuation has drift wave properties [70,78] .

The time evolution of the edge density fluctuations at the L to H transition has been reported [75,86] . The authors regard the fluctuation of the homodyne signal as the density fluctuation but the reason is not shown in their paper. The system is multichannel. The fluctuation of the homodyne signal coming from the small cut-off density, $\lesssim 1\times10^{19}\mathrm{m}^{-3}$, is reduced at the L to H transition, whereas the reduction of the fluctuation of the homodyne signal coming from the large cut-off density, $\sim 2\times10^{19}\mathrm{m}^{-3}$, is delayed from the L to H transition. They say that this result means the turbulence suppression occurs primarily in a limited edge region. Their system is homodyne and the movement of the cut-off layer can not be estimated. The width of the edge region is not estimated from the position of the cut-off layer when the fluctuation of this cut-off layer is reduced.

Sips et al. report the existence of an inward propagating density pulse after a sawtooth collapse. By considering this result in a 1 D numerical transport model including diffusive and convective terms, the cross field particle diffusion coefficient D_p has been estimated [87].

The broadening of the injected radio frequency (RF) line in the frequency spectra detected during the lower hybrid experiment in ASDEX has also been studied by Schubert et al. [88].

Pulse radar technique can also measure the density fluctuation because the repetition rate of the system is 500 kHz. This repetition rate is determined by a time-to-amplitude converter. RTP has a four channel pulsed radar system. The disruption induced by the pellet ablation has been observed. It shows that the edge profile does not change about

2 ms after a disruption and the plasma disappear 6 ms after the disruption.

The reflectometer systems of ASDEX, CCT, DIII-D also have the antenna at the high field side (CCT has more antennas at top and bottom). Manso et al. (ASDEX) [57] report that perturbations of the ELM coincide at both high and low field sides with the beginning of the H_α emission at the divertor. The reflectometer of CCT and DIII-D show asymmetry characteristic of the fluctuations at L to H transition. [86,89] .

The correlation measurement is important in order to understand the physics of the transport. This topic is also researched [46,69,73,77,78,82,90–94].

Cripwel et al. show that the measurements on JET under specific ohmic plasma condition give a wave phase velocity of 500 km/s and a correlation length in the range 2 $< l_c <$ 4cm [90]. Costley et al. show correlation increases from OH to L-mode [46]. There is also an increase as the NB injected power is increased.

Mazzucato et al. report the correlation of OH and NB heated plasma in both edge and core region [78]. In OH plasmas, fluctuations in the drift wave frequency range have been observed with long radial scale lengths ($\sim$ 4 cm) and fluctuation levels vary from less than 0.1 % in the plasma core to $\sim$ 1% at r/a $\sim$ 0.8. In NB heated plasmas, fluctuations in the outer plasma region exhibit very broad frequency spectra which bear little resemblance to drift wave frequencies and appear uncorrelated on a scale length of $\sim$ 4 cm. On the contrary, in the central region of Supershot plasma [95], low amplitude ($<$ 0.1 %) fluctuations with very long ($\sim$ 15 cm) correlation lengths and frequencies in range of energetic ion bounce frequencies have been observed.

Estrada et al. use another method of correlation measurement involving homodyne detection and based on the slow sweeping of one oscillator while the other remains at a fixed frequency [73,94].

Recently, a major topic is the improvement of the confinement of the plasma with a reversed magnetic shear. Mazzucato et al. reports about this topic [84]. There are two types of plasmas with a reversed magnetic shear: ERS (enhanced reversed shear) mode and RS (reversed shear) mode. These shear profiles are very similar just before bifurcation. However reflectometer measurement shows that the characteristics of density fluctuation differ each other after the bifurcation. The suppression of turbulence in the ERS mode is consistent with the suppression of turbulence by the $\boldsymbol{E} \times \boldsymbol{B}$ velocity shear.

Another recent area of study regards the TAE mode (Toroidal Alfven Eigen mode). This instability is enhanced by the presence of high energetic ions. In fusion plasma, the confinement of alpha particles is a key issue, and TAE may deteriorate the confinement. Deuterium-Tritium experiment is carried out in TFTR to study the physics of TAE. Nazikian et al. enumerate the results of this experiment and also refer the contribution

of the reflectometer as the tool to investigate the core plasma. The n=3 TAE mode is clearly observed at $r/a \sim 0.42$, here n is the toroidal mode number, however no coherent mode activity is observed at $r/a \sim 0.57$ or at larger radii [85].

It must be also mentioned here that the results of Ref. [43, 71, 73–76, 90] is obtained from a simple homodyne system. So in their data, the fluctuation of the reflected power and the phase are not separated.

Reflectometer has some unanswered questions as a diagnostic tool. One of them is a spatial resolution. A controlled laboratory plasma experiment has been performed in order to investigate this question [96,97]. The ion acoustic wave with various wavenumber has been used as the perturbation. The reflected wave brings back the information of the perturbation at the cut-off layer independent of the wavenumber of the perturbation. The result is contradictory with the prediction by Bretz [98].

1.4.4 Other Applications

The correlation reflectometer is mainly used in order to understand the transport. The poloidal correlation reflectometer of FT-2 has been used to measure the current profile by identifying the mode number of MHD activity [99].

The magnetic shear suppresses MHD instability. A controlled magnetic profile is one of the requirements to obtain fusion plasma. Thus a monitor of the total magnetic field profile is needed. The application of existing techniques to measure internal fields such as polarimeter to an ignition device will be extremely difficult because of the limitation of the access to the fusion plasma. The reflectometer can be a suitable alternative technique because the cut-off layer of the wave with X-mode polarization is related not only to the density profile but also to the magnetic field. This idea has been experimentally confirmed by Costley et al. [46].

This capability of magnetic field measurement is also used by Mase et al. [100]. Mase et al. have estimated the magnetic fluctuation and specified Alfvén ion-cyclotron wave.

RF (radio frequency) current drive is an attractive method by which we can control the current density profile and also obtain steady-state of long pulse operation. However, there is not enough experimental data to understand RF wave physics issues, such as wave trajectory, heating mechanisms, RF wave deposition profile and wave number. The reflectometer is used as the monitor of the RF heating by using its localized and nonperturbing feature [101].

Conway et al. have proposed another density fluctuation measurement. The technique uses the distorted-mirror model [83]. The coherent reflection coefficient and the incoherent reflection coefficient have been measured. The density fluctuation has been estimated from these coefficients.

1.4.5 Runaway Phase Phenomena

Problems of the reflectometer have been reported. One is the rapid change of the reflected power [102–104], and another is the runaway phase phenomena, which are sometimes referred as phase shift or phase ramp. [49,77,81,84,102–107].

The runaway phase is a phenomena in which the phase difference between the reflected wave and the reference wave increases monotonically and can not be explained by the movement of the cut-off layer. Reflectometers, except those that use the pulse radar method, generally measure the phase difference according to the geometrical optics approximation. The runaway phase is a problem related to the essence of the reflectometer diagnostic. The relation between runaway phase and the poloidal rotation has been investigated by Brañas et al. [106,107].

Two-dimensional simulation also shows that the poloidal rotation and the misalignment of the antenna can cause the runway phase [108].

The data with the runaway phase have been analyzed mainly by two methods until now. One method uses the low pass filter or the averaging. This method is applied to the signal before the phase is calculated. The filtered or averaged signal is expected to reflect the slow movement of the cut-off. The other method uses only the data in the period when the runaway phase does not exist. Reasonable results have been obtained by using these methods.

However these methods have drawbacks. The former cannot measure the fluctuations because the cut-off frequency of the low pass filter is lower than that of the frequency of the typical fluctuation or the averaging time is longer than the inverse of the frequency of the typical fluctuation. In the latter case, it is difficult to measure the fluctuations, whose frequency is mainly less than 100 kHz, with the good frequency resolution because the length of the period when there does not exist the runaway phase is short. These two methods are based on the geometrical optics even though the runaway phase phenomena cannot be explained from the image of the geometrical optics. The reason why the geometrical optics can be used in the situation when these methods are used must be shown, however the reason has not been accounted for until now.

The method of analysis, especially the method of fluctuation analysis, during the period of the runway phase has not been yet established.

1.4.6 Simulation

Many simulations have been performed not only in one dimensional scheme [98,109–116] but also in two dimensional scheme [117–120].

There are many unanswered questions about the feature of the localized measurement

because the scale length of the physical phenomena in the fusion plasma is comparable to the wave length of the incident wave. The feature of the localized measurement is one of the most frequently discussed subjects.

The results of the simulations show that the phase response strongly depends on the radial wavenumber, the position, the shape and the size of the fluctuation and the localization is guaranteed when the radial wavenumber of the fluctuation is small. Fanack et al. has performed the simulation related to the subject of the localization [116]. They say they can reproduce the "non wavenumber dependence" experimental results [96, 97] by considering the sharp shape of the fluctuation.

Theoretical treatments of sensitivity and resolution of correlation reflectometry presented by Bretz and Hutchinson [98, 109], led to the conclusion that the accuracy of correlation measurements can not be better than $\sim 4\lambda_0$, where λ_0 is the wave length of incident wave in vacuum.

However experimental results often show the correlation length to be less than λ_0. Using the random phase screen model, Mazzucato and Nazikian show that this phenomenon is caused by the large fluctuations [93, 121]. Bruskin et al. show that this discrepancy between the experimental results and the previous one dimensional theoretical prediction comes from the two dimensional effect [122].

RFP (Reversed Field Pinch), helical devices and small aspect ratio tokamak have high sheared magnetic field. Coupling between the O-mode and X-mode and the simultaneous reflections from the O-mode and X-mode cut-off layer in the plasma with such magnetic field must be considered. Mode coupling can be also useful for the magnetic fluctuation measurement. These have been discussed in Ref. [123–126]. The analysis method when the simultaneous reflection occurs has been also proposed and examined by Nagatsu et al. [127]. They use maximum entropy method (MEM) in order to separate the two beat signals coming from the O-mode and X-mode cut-off layer.

One dimensional simulation of the ultrashort-pulse reflectometer has been also reported [128].

1.5 Purpose of This Paper

The purpose of this paper is the establishment of a method to analyze the data with the runaway phase phenomena. This widens the scope of application of the reflectometer as a diagnostic to measure the density fluctuation and profile.

In this paper, we firstly have analyzed the data by method based on the geometrical optics. Here also we have observed the problems such as the runaway phase phenomena

and the rapid change of the reflected power.

Secondly we discuss the relation between the runaway phase and the scattering. The runaway phase can be explained by the scattering by the density fluctuation. The fluctuation measurement by using the reflectometer should be analyzed as the data of the scattering wave. The rotary spectrum and the complex spectrum analysis are proposed as the tools.

Thirdly the density fluctuations in L-mode and H-mode plasmas are discussed. The data is analyzed from the point of view that the reflected wave bring back the information of the density fluctuation as the scattered wave. It is also confirmed from this point of view that the low pass filtering method is effective, when the density profile is estimated from the data with the runaway phase.

2. Instrument

2.1 JFT-2M

JFT-2M (JAERI Fusion Torus - 2 Modified) [129] is a medium-sized tokamak with a D-shaped vacuum vessel of major radius 1.31 m made of stainless steel of 25 mm thickness. The inside wall and top divertor are completely covered while the outside wall is partially covered with the graphite plates in order to reduce the metal impurities. The bottom divertor is modified to improve a divertor performance with a closed configuration. The divertor and baffle plates for the closed configuration are made of stainless steel to study a transport of high-Z impurity in the scrape-off layer (SOL).

Both circular or D-shaped limiter and single or double null divertor configuration is available. The minor radius, a, is 0.35 m for full size D-shaped limiter discharge and 0.26 m for the smallest divertor configuration. The available toroidal field is $B_T < 2.2$ T.

There are three additional heating systems. They are NBI whose maximum input power into the torus is 1.6 MW, ECRH system of 60 GHz whose maximum generation power is 1 MW and the fast wave heating system of 200 MHz.

Main diagnostics are conventional magnetic measurements, FIR interferometer with vertical path and 2 mm microwave interferometer with horizontal path for line averaged electron density $\bar{n}_e$ measurements, ECE (Electron Cyclotron Emission) system using the second harmonics of the electron cyclotron frequency for the electron temperature T_e measurement, and soft/hard X-ray measurement for the electron energy distribution measurements, TV thomson scattering system for the electron density and temperature profile measurements, charge-exchange spectroscopy system for the plasma rotation and the ion temperature measurements, TOF (Time-of-Flight) system for the ion energy distribution measurement, visible and vacuum ultraviolet spectrometers for impurity analysis, probes on the divertor plate, in the SOL or the edge plasma for the electron density, temperature and potential measurements, bolometer arrays for radiation monitor, and infrared camera system for the power flux measurement on the divertor plate.

In this paper, we discuss the L-mode and H-mode plasmas. Some interesting works about these modes on JFT-2M have been reported in Ref. [130–136].

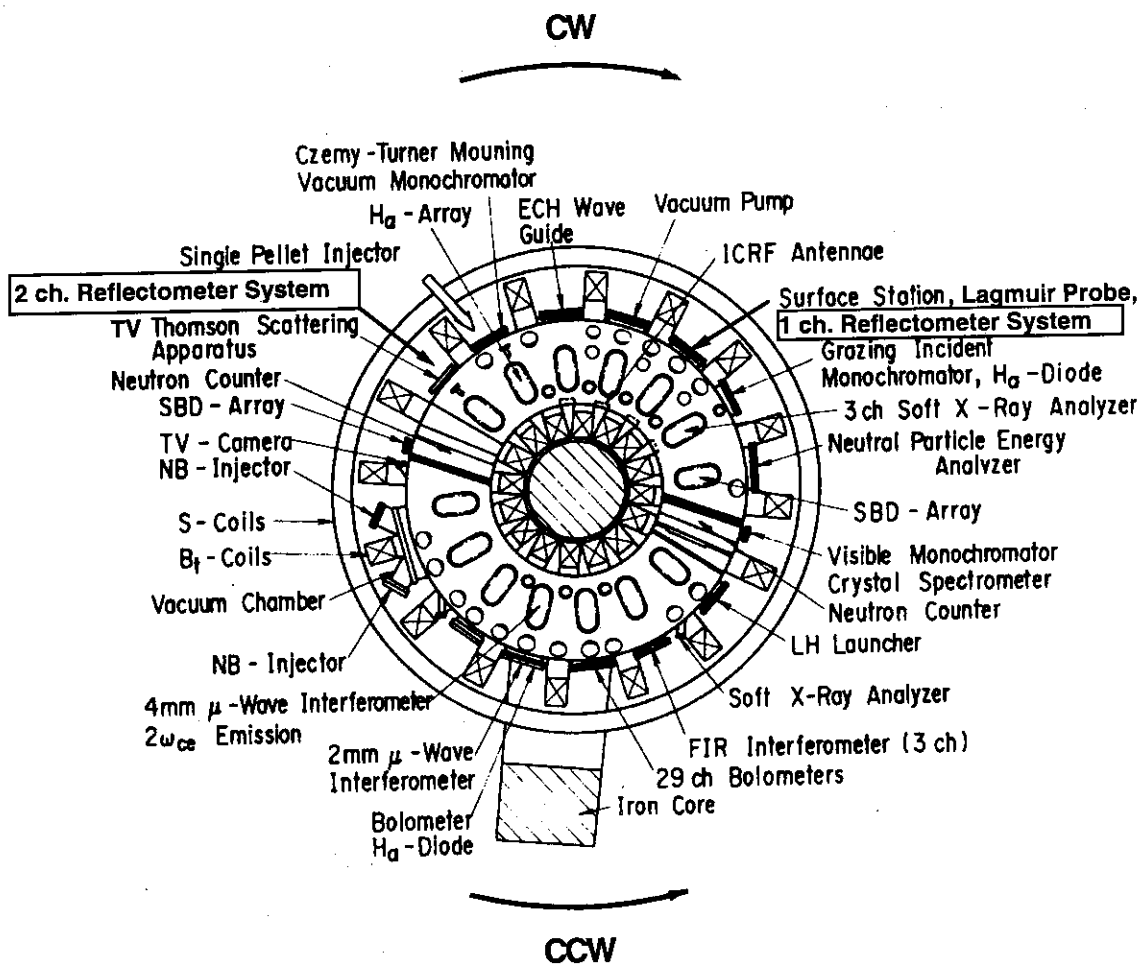

Figure 2.1: Top view of JFT-2M device and the arrangement of the plasma diagnostics.

2.2 Reflectometer

2.2.1 Homodyne System

Figure 2.2 shows the schematic diagram of the installation of the antenna on the JFT-2M tokamak. Two antennas are used; one is for launching the probe wave and the other is for receiving the reflected wave. The probe wave with the frequency of 50 GHz, amplitude of 10 mW, and with the electric field parallel to the horizontal plane (O-mode) is launched. As the ratio of the magnitude of the poloidal magnetic field to that of the toroidal one is less than 6.5 %, the X-mode component of the launched wave is negligible. The cut-off density is $3.1 \times 10^{19}\mathrm{m}^{-3}$. The cut-off layer is located at $r/a = 0.2 - 0.8$ (where a is the minor radius on the mid-plane) in the steady OH phase or L-mode phase of the typical discharges of JFT-2M tokamak. The cut-off layer moves to $r/a \gtrsim 0.9$ in the H-mode phase due to the change of density profile. The transmission loss of the microwave in the free space reduces the signal to noise ratio. The distance between the tip of an antenna and the most outer flux surface is as close as 46 mm in the case of limiter discharge and 30 - 100 mm in the case of divertor discharge. The launching path and the receiving path have their own vacuum windows. The vacuum window is made of sapphire glass whose thickness is 0.3 ± 0.02 mm and they are welded at the vacuum interface. A plate of stainless steel installed between two antennas prevents the launched wave from directly entering the receiving antenna.

Schematic view of the homodyne reflectometer system is shown in Fig. 2.3. A solid state Gunn oscillator is used. The Gunn oscillator is easy to handle and is insensitive to the strong magnetic field.

The quadrature phase detection is used for the measurement of the phase difference φ between the reflected wave and the reference. The quadrature phase detection system consists of two balanced mixer systems and one phase shifter.One balanced mixer system is made of two single ended mixers, one magic tee and one differential DC amplifier whose bandwidth and gain is 10 MHz and 60 dB, respectively. The reflected and the reference wave are mixed in a single ended mixer. As the linear envelope detection is employed, the mixer diode is biased by the reference wave with power of 3 mW. The linear envelope detection is more sensitive than the square-law detection [137]. The power of the reflected wave is much smaller than that of the reference. The output of the mixer diode consists of a large offset ($\sim$100 mV) and a small signal ($\sim$ a few μV). The large offset component can be canceled by differentially amplifying these two outputs of single ended mixers, because only signal outputs from the two mixers have a phase difference of π with each other due to the characteristic of the magic tee. A phase shifter produces the $\pi/2$ difference of phase between the two reflected waves which come into the mixers. The output of one balanced mixer system is proportional to $\sqrt{P_R}\cos\varphi$ and the other $\sqrt{P_R}\sin\varphi$ [137]. Here P_R is the

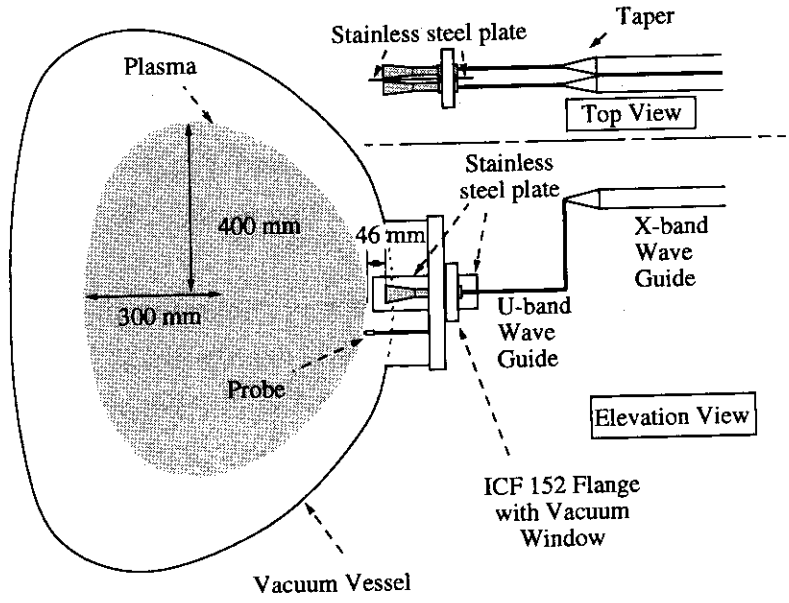

Figure 2.2: Arrangement of the antenna of 1 channel reflectometer system in the vacuum vessel of the JFT-2M. Two antenna are placed side by side in the toroidal direction. The probe wave is launched into the mid-plane of the plasma. A plate of stainless steel installed between two antennas prevents the launched wave from directly entering the receiving antenna. The position of the Langmuir probe is also shown. The probes and the antenna of the 1 channel reflectometer system are separated by 10 cm both in the toroidal direction and vertical direction.

power of the reflected wave.

Two signals are recorded on the memory of the ADC (Analog-Digital Converter) whose capacity is 512 k samples with the sampling rate from 500 k samples/s to 25 M samples/s. Typically the sampling rate of 5 M samples/s is used. The data window is about 100 ms.

The memorized data are subsequently transformed to the time series of P_R and φ by using work station. We consider that the sampling rate is high enough for the phase not to change more than π during a period between two sequential data when we track the time evolution of the phase as shown in Fig. 2.4.

The outputs of two balanced mixer systems is calibrated in order to improve the accuracy of measurement. The two raw outputs is expressed by $A_1\sqrt{P_R}\cos(\varphi+\delta)+B_1$ and $A_2\sqrt{P_R}\sin\varphi+B_2$, respectively. The values of A_1 and A_2 depends on the performance of the mixers. The value of δ is the deviation from the $\pi/2$ phase difference. The values of B_1 and B_2 are the residual offset components of the outputs of the single ended mixers. The calibration is carried out as follows:

1. The output of the calibrated oscillator fixed on 50 GHz + 100 kHz is fed to the quadrature phase detection system instead of the reflected wave. (see Fig. 2.3.)
2. Two signals of the two balanced mixer systems are acquired in the same way as the signals coming from the reflected wave are acquired.
3. The auto-power spectrums and the cross-phase are calculated from two signals.
4. The values of A_1 and A_2 are obtained from the amplitude of the peak at the frequency of 100 kHz.
5. The value of δ is obtained from the cross-phase at the frequency of 100 kHz.
6. The values of B_1 and B_2 are obtained from each average of the two time series.

The calibrated data are obtained by using these values as follows:

$$\begin{pmatrix} x_c \\ y_c \end{pmatrix} = \frac{1}{\cos\delta}\begin{pmatrix} 1 & \sin\delta \\ 0 & \cos\delta \end{pmatrix}\begin{pmatrix} (x_r - B_1)/A_1 \\ (y_r - B_2)/A_2 \end{pmatrix}, \tag{2.1}$$

where a pair of x_r and y_r is the raw outputs of two balanced mixer systems and a pair of $x_c(=\sqrt{P_R}\cos\varphi)$ and $y_c(=\sqrt{P_R}\sin\varphi)$ is the calibrated data. The calibration is carried out every ten shots, because the balanced mixer systems are subject to changes in the values of B_1 and B_2 over a long period of time.

Two kinds of tests have been performed for the purpose of verifying the reflectometer system itself. One test is as follows: the reflecting mirror made of copper was placed in front of the antenna. The distance between the antenna and the mirror were changed

from 0 to 2000 mm. When one signal from one balanced mixer was plotted in the x direction and the other was plotted in the y direction, the data point rotated by the value of 2π every 3mm in a distance from the antenna to the mirror. This fact agrees with the principle of the reflectometer, which shows that the phase increases by the factor of 2π when the reflector moves by the factor of $\lambda_0/2$.

The other test uses a copper reflector which was oscillated by an audio speaker with the frequency of 200 Hz in order to test the dynamic characteristic of the reflectometer. The signals from two balanced mixers were acquired and processed in the same way with the measurement of the density fluctuations. The auto-power spectrum of the phase data acquired in this test have a peak at 200 Hz. This test is an overall check of the reflectometer system. We have confirmed that both the hardware and the software components of the reflectometer system work properly.

2.2.2 Heterodyne System

It is important to know the offset level accurately in order to obtain phase accurately when the reflected power becomes small. The phase accuracy is less than 10 degree when the reflected power is 1 μW owing to above mentioned calibration. This method of calibration has a drawback that we frequently waste the discharge on performing the calibration.

In order to overcome this drawback, we upgrade the reflectometer system to the heterodyne system. Figure 2.5 shows the block diagram of the system. The frequency of the probe wave is 50 GHz, the same as that of the homodyne system and 50 MHz is the frequency difference between the probe wave and the wave generated by the local oscillator, namely IF(intermediate frequency). Here we label the output of the mixer which mixes the reference wave and the wave generated by the local oscillator as the reference output and the output of the mixer which mixes the reflected wave and the wave generated by the local oscillator as the signal output. The reference output is stationary and its frequency is $f_{IF} = 50$ MHz, ($\sqrt{P_{ref}}\sin(2\pi f_{IF}t)$). The signal output includes the phase and amplitude of the reflected wave in the carrier wave whose frequency is f_{IF}, ($\sqrt{P_{sig}}\sin(2\pi f_{IF}t+\varphi)$) . These two outputs are fed into the phase sensitive detector through an AC amplifier. The inputs of this phase sensitive detector are $\sqrt{P_{ref}}\sin(2\pi f_{IF}t)$ and $\sqrt{P_{sig}}\sin(2\pi f_{IF}t+\varphi)$ and the outputs are $\sqrt{P_{sig}}\cos\varphi$ and $\sqrt{P_{sig}}\sin\varphi$. The outputs of $\sqrt{P_{sig}}\cos\varphi$ and $\sqrt{P_{sig}}\sin\varphi$ are the same with the outputs of the quadrature phase detection of the homodyne system. The quadrature phase detection is performed in the range of the downconverted frequency. The same system with the homodyne system in processing the signal is used. The AC amplifier between the mixer and the phase sensitive detector is effective in suppressing the change of the offset level of the mixer. The phase accuracy of this system is less than

1 degree when the reflected power is 1 μW without the calibration.

The heterodyne system usually has a phase lock loop system or a super heterodyne system in order to be unaffected by the fluctuation of the IF. Our system has neither but the frequency of Gunn oscillators are quite stable and the fluctuation of the frequency is less than a few MHz which is allowed by the phase sensitive detector. The wave transmission system and antennas is same with the homodyne system because the frequency of the launched wave has not been changed.

2.2.3 2 channel Heterodyne System

The delay of the reduction of the density fluctuation at the L to H transition has been observed by the 50 GHz fixed frequency, 1 channel system as mentioned later. From Langmuir probe measurement, the edge turbulence reduces at the same time when the intensity of H_α signal reduces. The profile of the turbulence reduction at the L to H transition is an interesting topic because the turbulence seems to be the cause of the anomalous transport and the essence of the improvement of the H-mode plasma seems to exist in the edge region. In order to investigate the profile of the turbulence reduction at the L to H transition, we have constructed the frequency tunable 2 channel heterodyne reflectometer system. The tunable range of the frequency of the incident wave is from 28 to 50 GHz. The corresponding cut-off density is from 0.97 to 3.10 $\times 10^{19}\mathrm{m}^{-3}$. The cut-off layer of $0.97 \times 10^{19}\mathrm{m}^{-3}$ exists in the edge region where the probe measurement is performed.

Figure 2.6 shows the block diagram of the 2 channel reflectometer system. The system consists of three reflectometer systems. One is a U-band system and the other two are Ka-band systems. The U-band system comes from a fixed frequency, 50 GHz, 1 channel reflectometer system as mentioned above. One Ka-band system and the U-band system are exchanged by the waveguide switch according to our point of interest.

Here U-band and Ka-band are the categories into which the microwave components are classified. The suitable range of the frequency of U-band is $40-60$ GHz. The suitable range of the frequency of Ka-band is $26.5-40$ GHz.

The frequency of the launched wave is changed from 28 to 50 GHz by changing the Gunn oscillator which is a narrowband, $\sim$ 3 GHz, mechanically tunable one. This type of oscillator has higher power of $\gtrsim$ 100mW, higher stability and is cheaper than other tunable oscillators.

The Ka-band system consists of almost the same components as the U-band system. Ka-band components are "oversized" components for waves in the frequency range of the U-band. The waves in the frequency range of the U-band can pass through the Ka-band isolators or other components for which isolation is important. In the Ka-band system

which is used with U-band system, we have installed a low pass filter which rejects the waves with higher frequency than that in the Ka-band.

We measure signals which has smaller power than the output power of the oscillator by -60 dB typically. It is also important to avoid cross talk caused by the leak of the higher power waves. We have reduced such kind of the cross talk to a negligible level for our electrical signal processing system by covering the components with a microwave absorber.

A combination of heterodyne and quadrature phase detection is used in order to measure the time evolution of the phase difference and the amplitude of the reflected wave in the same way as a 1 channel heterodyne system. The IF is stable if we do not change the frequency of the incident wave. The tunable system often changes the frequency. The IF drifts a few MHz for about 20 $\sim$ 30 minutes after the frequency has been changed. It is expected that the operation frequency is frequently changed in this system. The IF is changed from 50 MHz to 150 MHz in order to increase the tolerance to the stability of the IF. The IF signals are filtered by using low pass filter with an attenuation of -40 dB at the 300 MHz because the signals with higher frequency than IF include cross talk with other channels and the spurious higher harmonics caused by the mixer.

Figure 2.7 shows the antenna system of the 2 channel heterodyne reflectometer, which is different from the previously mentioned antenna system in which the U-band was used and the waves of the Ka-band could not propagate. The Ka-band antenna is set outside the vacuum vessel because Ka-band components are larger than U-band components and it is difficult to set the antenna system inside the vacuum vessel.

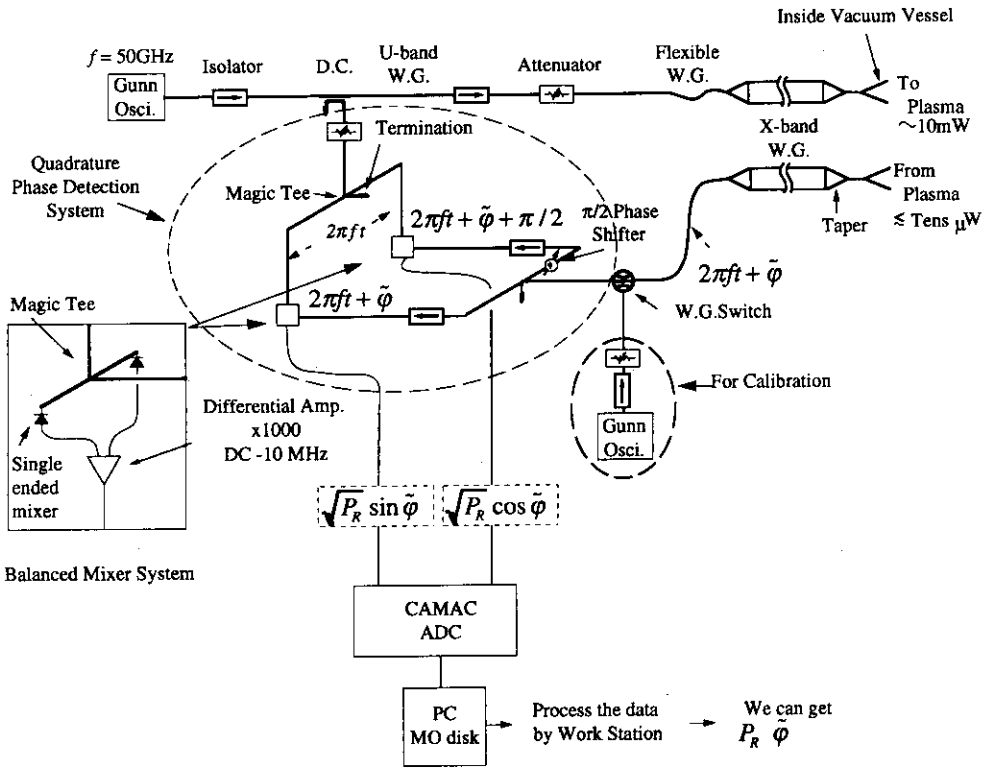

Figure 2.3: Block diagram of the JFT-2M reflectometer system.

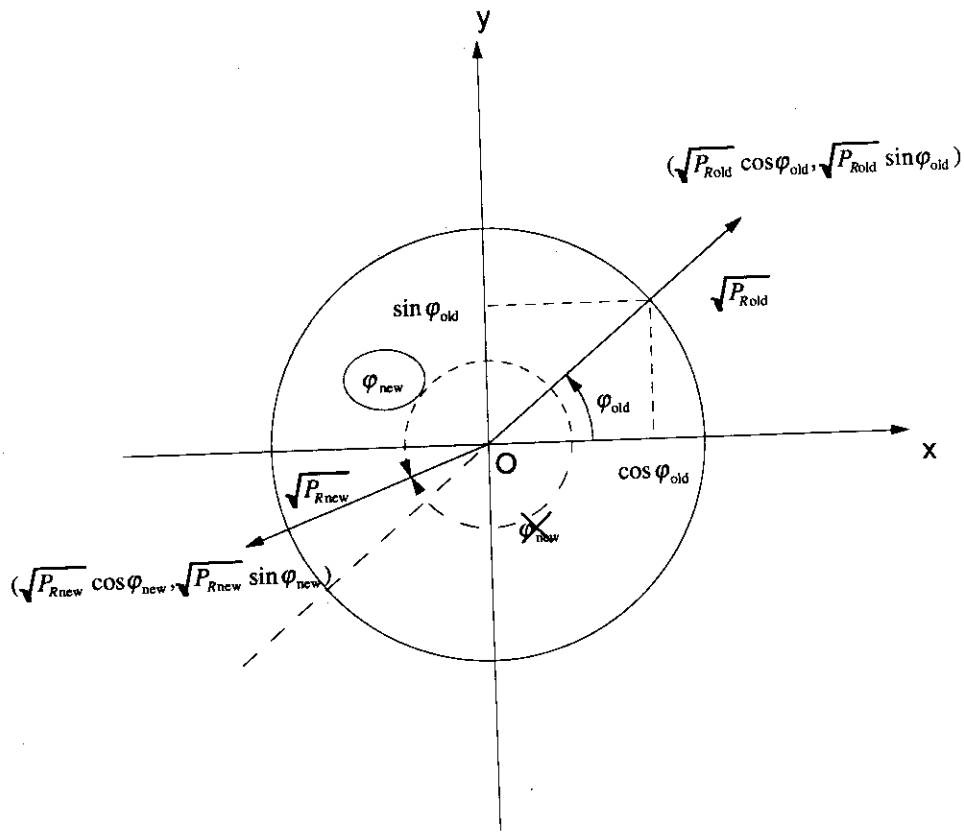

Figure 2.4: Procedure of the determination of the time evolution of the phase and the power. We assume that the phase does not change more than π during a period between two sequential data.

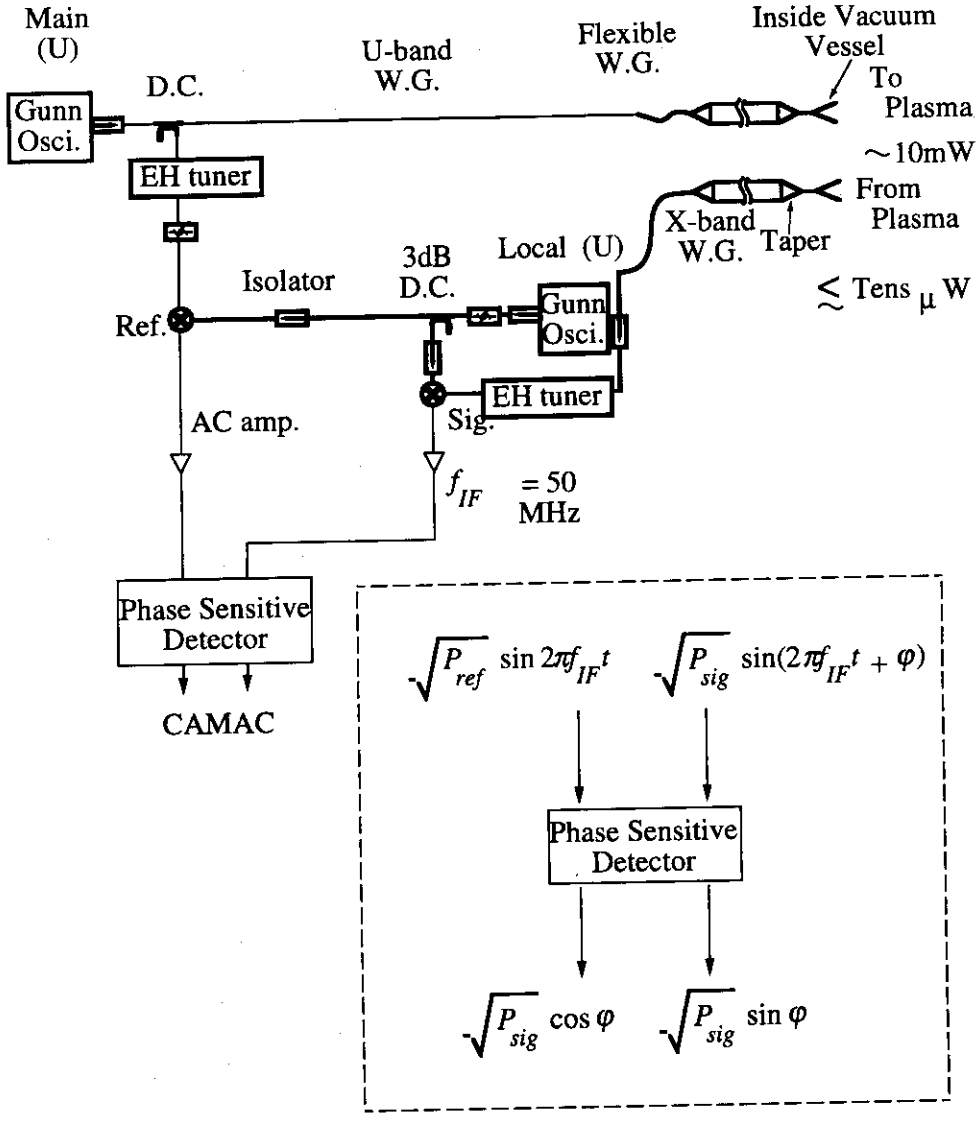

Figure 2.5: Block diagram of the JFT-2M heterodyne reflectometer system. The phase sensitive detector outputs $\sqrt{P_{sig}}\cos\varphi$ and $\sqrt{P_{sig}}\sin\varphi$. These data are acquired by ADC of CAMAC with the sampling rate of 5 M samples/s.

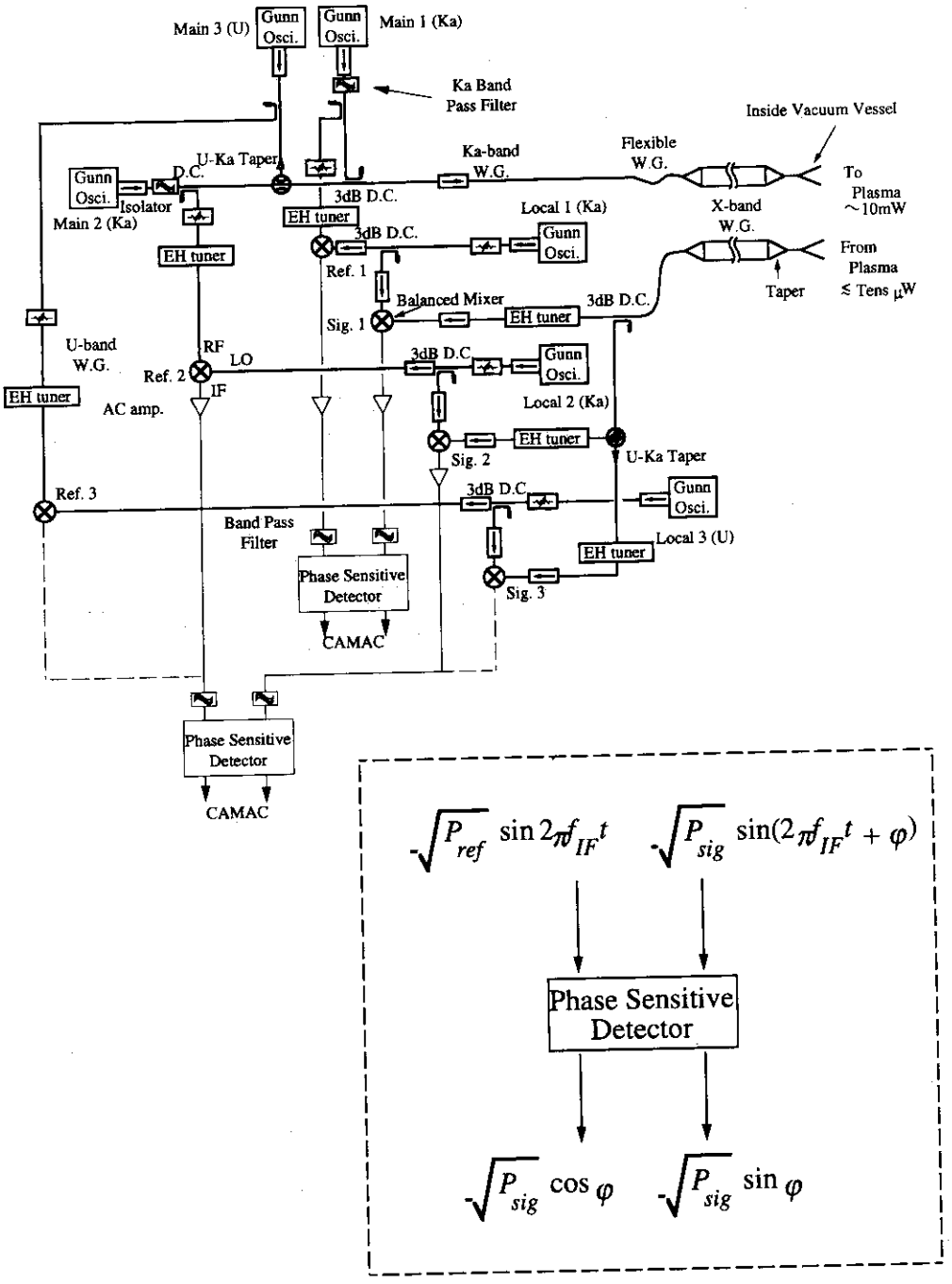

Figure 2.6: Block diagram of the 2 channel reflectometer system.

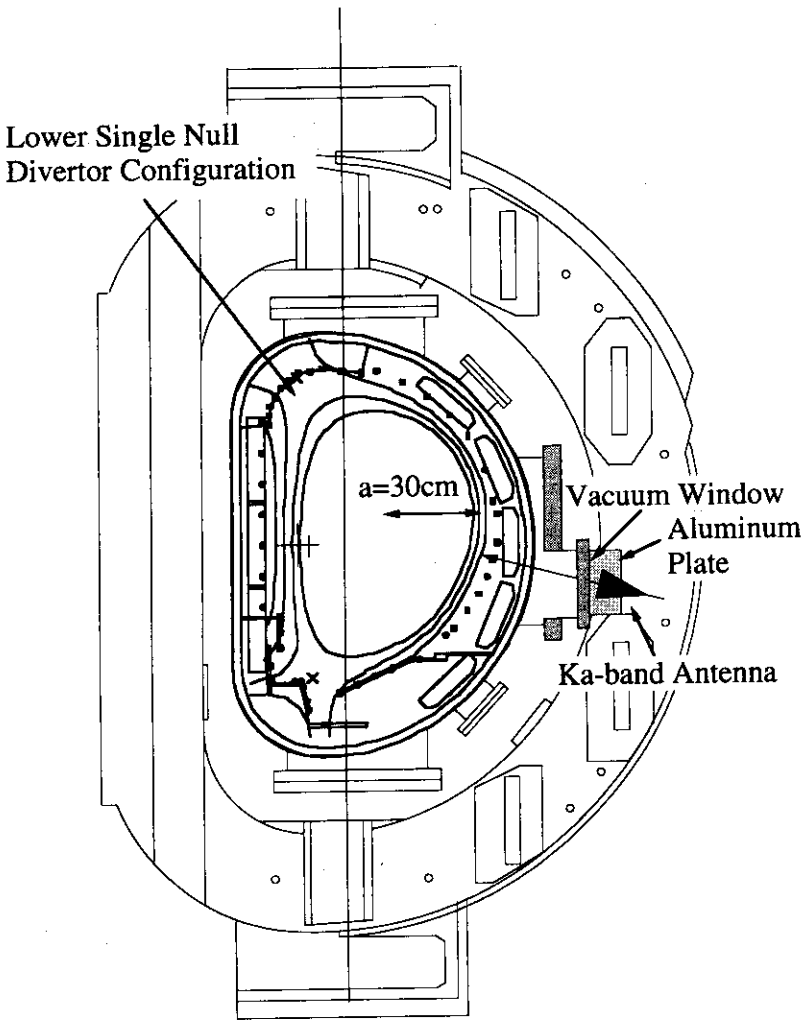

Figure 2.7: Arrangement of the O-mode 2 channel heterodyne reflectometer system. Two antennas are set in the toroidal direction outside the vacuum vessel. A aluminum plate has been installed between two antennas in order to prevent the launched wave from entering the receiving antenna directly

3. Experimental Results of Runaway Phase

3.1 Homodyne System Results

3.1.1 Typical Results

A typical result is shown in Fig. 3.1. The toroidal field is about 1.2 T. The electron cyclotron resonance of the launched wave does not exist in the plasma in this toroidal field. The plasma current ($I_p = 230$ kA) and the radial position of plasma center are kept constant from 450 ms to 850 ms. The minor radius grows till about 500 ms and remains almost constant at $a \sim 27$ cm to the end of the discharge. The time evolution of line integrated density, $\int n_e dl$, measured by the microwave interferometer on the mid-plane is shown in Fig. 3.1(a). The line averaged electron density $\bar{n}_e$ reaches a cut-off density of the launched wave (3.1×10^{19} m^{-3}) at about 600 ms. The neutral beam (NB) of 600 kW (co: 320 kW,counter: 280 kW)is injected from 700 ms to 900 ms, where co-injection means the direction of the NB injection is parallel to the direction of the plasma current and counter injection means the direction of the NB injection is anti-parallel to the direction of the plasma current. The L to H transition is characterized by the reduction of the intensity of the H_α line emission (Fig. 3.1(b)). The L to H transition occurred at about 730 ms and the H to L transition occurred at about 850 ms.

Figures 3.1(c) and (d) show the time evolutions of the received power, P_R, and the phase, φ, respectively, measured by the reflectometer. The phase and the power before 50 ms and after 970 ms is those of the wave reflected from the wall facing the antenna because there is no plasma in this period. The power of the reflected wave changes by a large amount of about 30 dB in a very short period of about 10μs like a burst. It should be noted that the monotonic decrease appears in the time evolution of the phase. The total change in the phase reaches a maximum of about −10000 radian between 600 and 700 ms, which corresponds to the displacement of the cut-off layer by 10 m. This displacement is much larger than the minor radius (a $\sim$ 0.3 m). The slope of the time evolution of the phase becomes steeper when $\bar{n}_e \gtrsim 2.8 \times 10^{19}$m^{-3}. Such phenomena as this have been observed at several reflectometer systems on ATF [77,91], JET [49], JIPP TII-U [103], W7-AS [81] and TFTR [84] and are called runaway phase phenomena.

The runaway phase begins from the early time, $\gtrsim$ 100 ms, of the discharge. The cut-off layer does not exist from 0 ms to about 400 ms. The runaway phase occurs even if there is no cut-off layer. This means the mechanism of the runaway phase does not need a cut-off

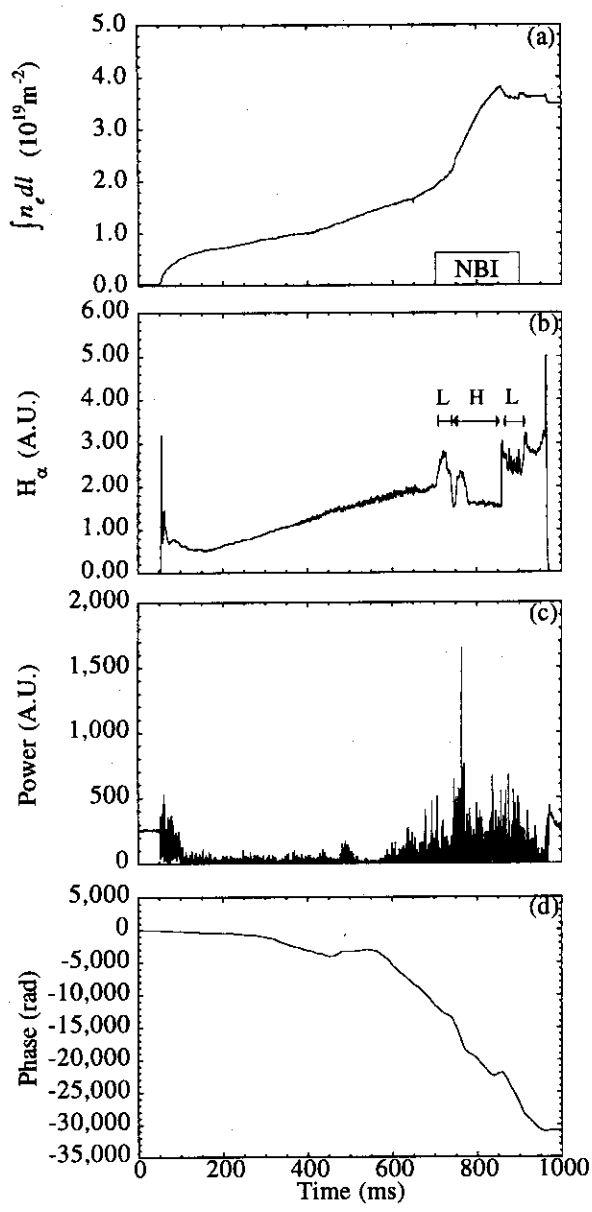

Figure 3.1: Measured signals in the H-mode discharge. (a) Time evolution of line integrated density, $\int n_e dl$, measured by microwave interferometer. The minor radius remains almost constant at $a \sim 27$ cm from about 500 ms to the end of the discharge. The line averaged electron density $\bar{n}_e$ is 3.1×10^{19} m^{-3} at about 600 ms. (b) Time evolution of the intensity of the H_α line emission. L/H transition occurred at about 730 ms and H/L transition occurred at about 850 ms. (c) and (d) show the time evolutions of the received power P_R, and the phase φ, respectively. B_T= 1.2 T. I_p=230 kA. The discharge gas is D_2. The configuration is the lower single null.

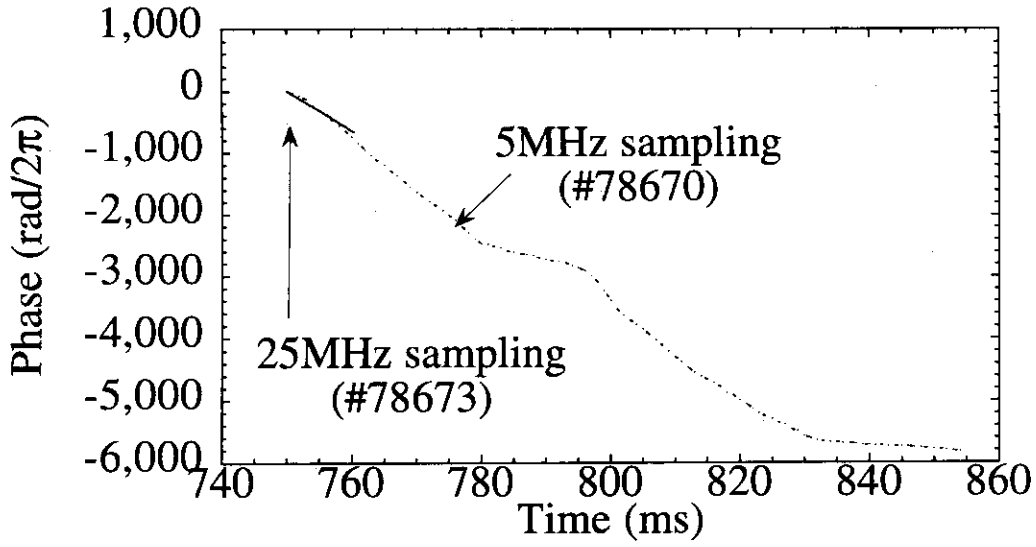

Figure 3.2: The data is sampled by the sampling rate of 25 M samples/s. The runaway phase phenomena have been observed in the same way in the same discharge condition.

layer.

The runaway phase does not happen in the following cases:

Case 1. There is no plasma, although a strong magnetic field exists.

Case 2. The microwave oscillator is stopped. The signal in this case shows noise of electric circuits and radiation from plasma.

Case 3. Microwave is not injected into plasma. In this case, the radiation is detected by the heterodyne detection system.

Case 1 indicates that a strong magnetic field does not have a serious effect on the detection system and the magnetic field is not the cause of the runaway phase. Case 2 shows the runaway phase is not caused by the noise described above or bugs of the program which calculates P_R and φ. Case 3 shows that the runaway phase is not caused by the radiation of the plasma. The runaway phase does not result from simple mistakes of the system. It is essential that the microwave is injected and received.

The runaway phase phenomena have been observed even with very fast sampling rate of 25 M samples/s as shown in Fig. 3.2. It is possible to deny that the phenomena result from the fact that there are very fast changes of phase and that the failures of reading phase happen due to the low sampling frequency.

3.1.2 Non-runaway Phase Period

Observing the phase data in detail, there are periods when the phase does not run away, and the phase just fluctuates as seen in the region marked by the circle in Fig. 3.3.

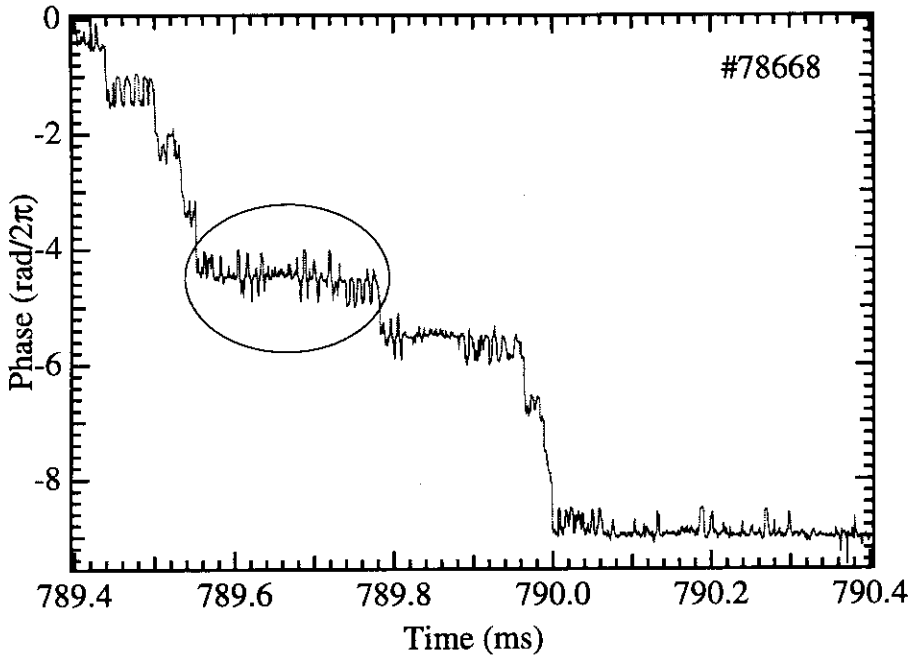

Figure 3.3: Time evolution of the phase in the extended time scale. Sampling rate is 5 M samples/s. The runaway phase phenomena do not occur during the region enclosed by the circle. The step-like runaway phase occurs in this figure, however it is not a discontinuous jump. There are some points between the consecutive step.

It is noted that the runaway phase seems to occur like a step function in this figure, but the phase changes gradually in another time range as shown in Fig. 3.4.

3.2 Heterodyne System Results

3.2.1 Experimental Results

The accuracy of the measurement has been increased by using heterodyne system. However, the runaway phase phenomena and the fast and large change of the reflected power have also been observed in heterodyne system. We have confirmed that these phenomena are inherent in neither homodyne system nor heterodyne system. This fact has been confirmed by the homodyne system and the heterodyne system which have the common wave transmission system and antennas.

3.2.2 Detection of Movement of Plasma

We can actively move plasma radially by controlling the vertical field. It is expected that the cut-off layer moves radially with a little change of the density profile on this movement. We have moved plasma radially in order to check whether the reflectometer see the movement of the cut-off layer. The calculated phases have showed the runaway

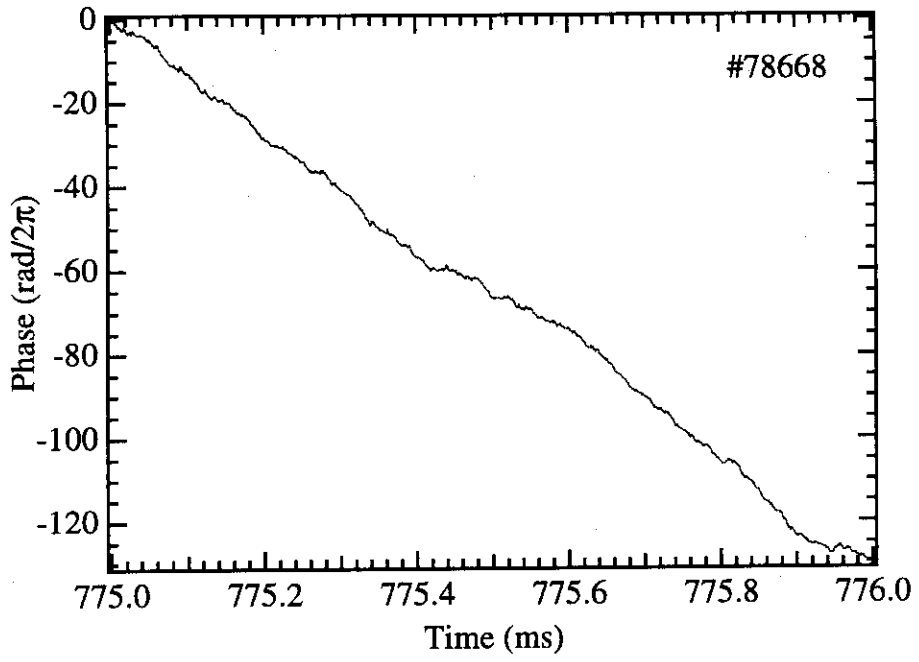

Figure 3.4: The runaway phase does not consists of only step-like structure.

phase phenomena and we can not see the movement of the plasma at a glance. The movement of the plasma has been buried under the large runaway. We can obtain the change of the phase corresponding to the movement of the plasma in fragments, namely non-runaway phase data. We have used the method of connecting these fragments as one approach to measure the movement of the plasma. As another approach, the low pass filter has been used as used in JET [49].

Method of Connecting Non-runaway Phase Data

Figure 3.5 (a) shows the time evolution of the position of the magnetic axis. The plasma has been actively moved outward 10 mm at the center from 800 ms to 830 ms. Figure 3.5 (b) shows the time evolution of the phase which has been constructed by connecting the non-runaway phase data. The movement of the plasma was detected from 800 ms to 815 ms. This is one indication that the reflectometer receives the "reflected wave" coming from the cut-off layer during non-runaway phase period even though it is difficult to regard the received wave as only the "reflected wave" at the cut-off layer when the runaway phase occurs.

The phase is reconstructed by just connecting the fragments of the non-runaway phase data. Some points in the edge of that fragment can suffer from the effect of the runaway phase and deviate from the trend of the each fragment. The sequential fragment has been connected to the deviating point when the reconstruction has been performed. The reconstructed phase suffer from such a few deviating points and is not "smoothly" connected.

For example, we can see such effects at 808 ms in Fig. 3.5 (b). The sequential fragment can also have such deviating points and the direction of the deviation often reflect the direction of the runaway phase. Because of the deviating points caused by the runaway phase, the reconstruction failed when the original phase has strong runaway phase, for example from 820 to 860 ms. Thus this method of just connecting the non-runaway phase data has scope for improvement.

Low Pass Filtering Result

It has been said that we must avoid the effect of the fluctuation when the density profile measurement is performed by the reflectometer. To do this, low pass filtering method, smoothing method, time averaging method and shot averaging method have been used. We have used numerical low pass filtering method. The measured couple of data, $\sqrt{P_R}\cos\varphi$ and $\sqrt{P_R}\sin\varphi$, are filtered, respectively. The cut-off frequency is changed from 0.1 kHz to 100 kHz. The amount of runaway phase decreases and the movement of plasma is revealed clearly as the cut-off frequency decreases. The movement of plasma cannot be detected when the cut-off frequency becomes less than 0.3 kHz. This is reasonable because the movement toward the antenna by 10 mm in 10 ms corresponds to a change of the fringe by 0.3 fringes/s, which is detected as a Doppler shift of 0.3 kHz. Figure 3.6 (a) shows the time evolution of the position of the magnetic axis again. Most plausible result has been obtained when the cut-off frequency is 1 kHz as shown in Fig. 3.6 (b). We can see the movement of the plasma from 800 to 818 ms. The plasma moved toward the antenna and was in the H-mode during this period. The H to L transition occurred at about 815 ms. The turbulence caused by L-mode has disturbed the signals and it has become impossible to measure the movement of the plasma. We can see the change of the phase from 750 ms to 790 ms which does not have the corresponding movement of the magnetic axis. This movement of the cut-off layer corresponds to the change of the density profile caused by the L to H transition. This movement of the cut-off layer is consistent with the change of the density profile measured by TV thomson scattering system.

3.3 Results of 2 channel Heterodyne System

3.3.1 Experimental Results

We have changed the oscillator from the fixed frequency oscillator to the frequency tunable oscillator. We have also modified the antenna arrangement from the inside of the vacuum vessel to the outside as mentioned in Chapter 2. The runaway phase has not disappeared though the frequency has been changed from 28 to 48 GHz. This means

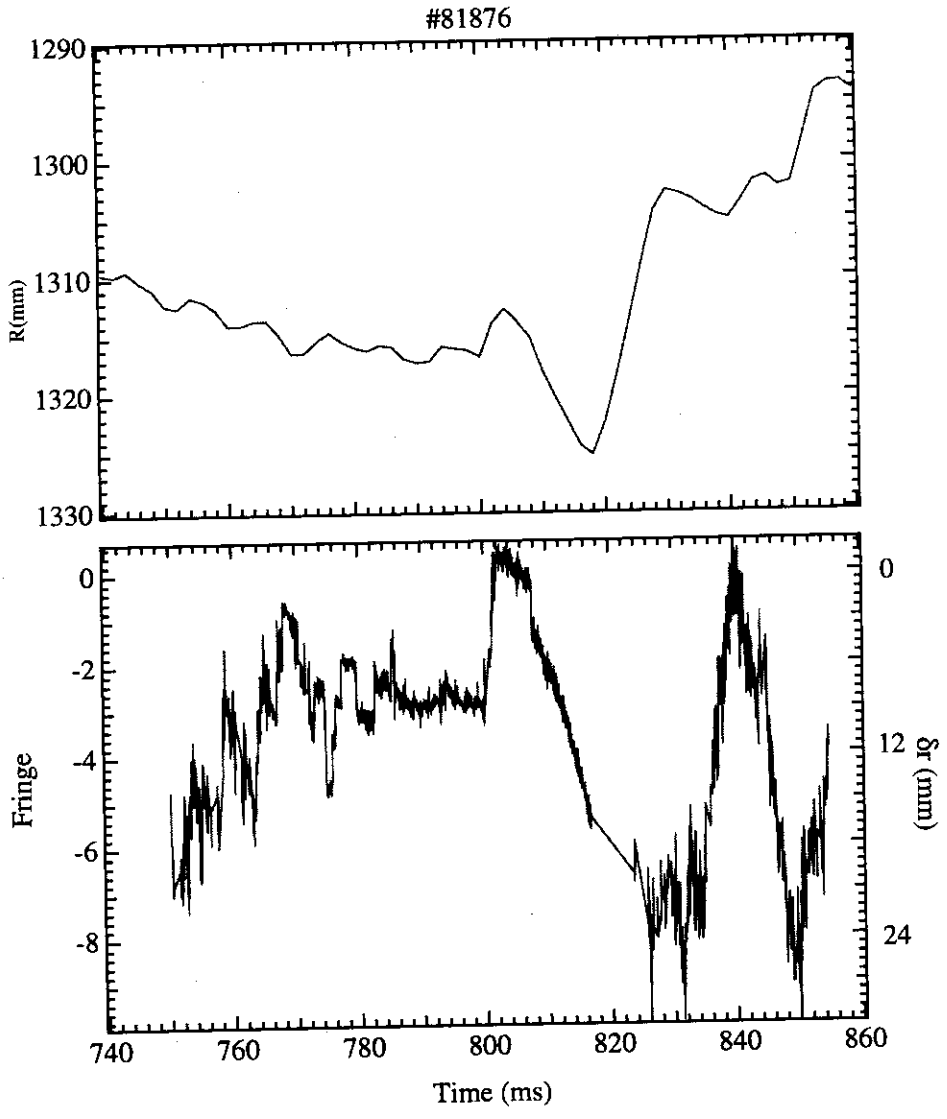

Figure 3.5: (a) shows the time evolution of the position of the magnetic axis. The plasma has actively moved outward 10 mm at the center from 800 ms to 830 ms. (b) shows the time evolution of the phase which has been constructed by connecting the phase data without the runaway phase. The movement of the plasma as shown in (b) has been detected from 800 ms to 815 ms.

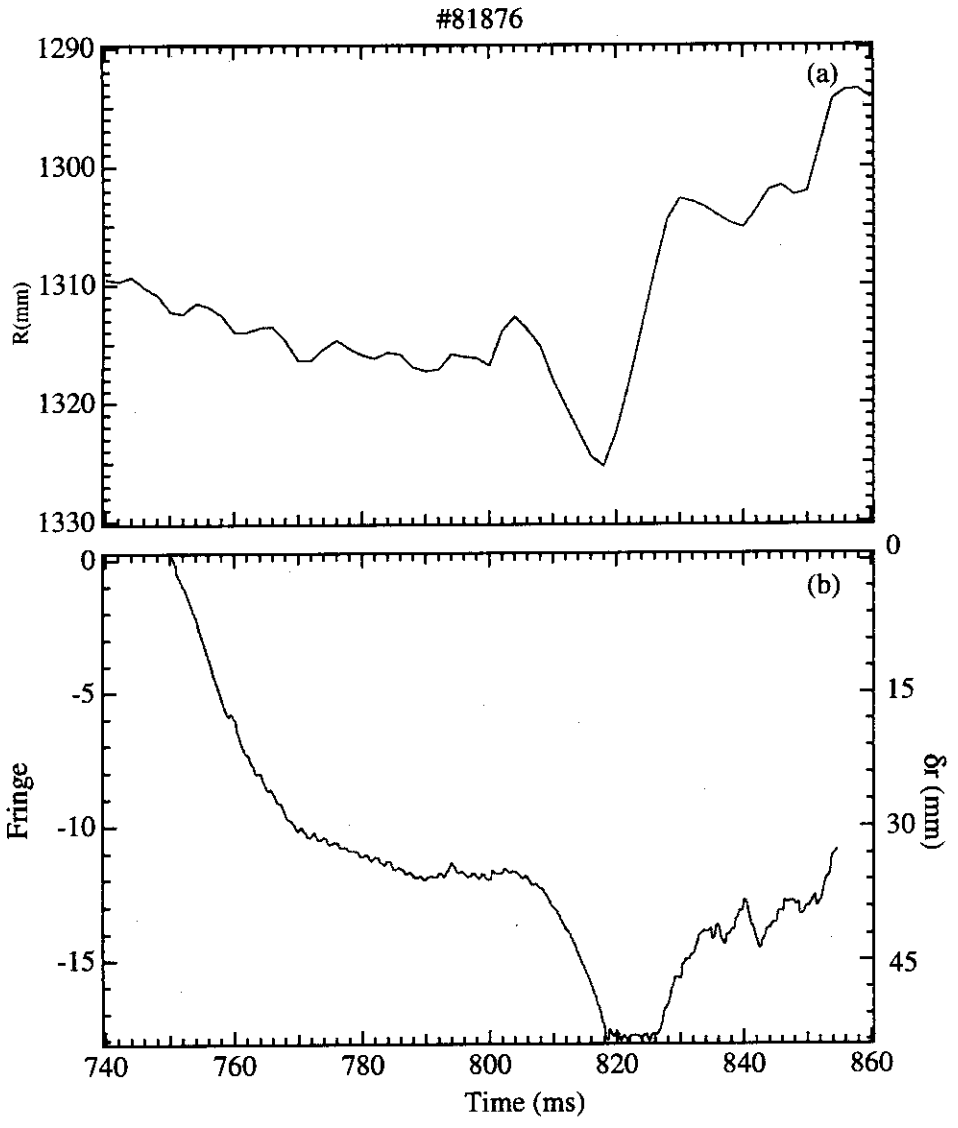

Figure 3.6: (a) shows the time evolution of the position of the magnetic axis. (b) Time evolution of the phase obtained by using the data filtered by the low pass filter. The cut-off frequency is 1 kHz.

the runaway phase is not peculiar to the particular frequency. The runaway phase has not disappeared though the angle of the antenna has been also changed. This means the cause of the runaway phase is not a trivial misalignment of the antenna.

3.3.2 Dependence of Runaway Phase on B_T

It is expected that the runaway phase phenomena is caused by the interaction between the incident wave and the plasma. This interaction always need the fluctuations of the plasma. The characteristic of many instabilities of plasma which cause fluctuations is changed when the toroidal magnetic field B_T are changed.

The dependence of runaway phase on the toroidal field is measured in the OH phase. The frequencies of the launched wave are 37 and 38.5 GHz. The corresponding cut-off densities are $1.70 \times 10^{19}\mathrm{m}^{-3}$ and $1.84 \times 10^{19}\mathrm{m}^{-3}$, respectively. The results are shown in Fig. 3.7. The sign of the change of the phase, namely the direction of the runaway phase, changes when the toroidal field is reversed and the degree of the runaway phase, which is defined as the change of the phase per milli-second, is proportional to the toroidal field.

To conclude that the degree of the runaway phase is proportional to the toroidal field is inconsistent with the fact that The phase velocity of the drift waves are inversely proportional to the toroidal field when the runaway phase is assumed to be caused by the drift waves. For example, the electron diamagnetic drift velocity is described in the form,

$$-\frac{T_e}{en_e}\frac{\hat{\boldsymbol{B}} \times \nabla n_e}{B},$$

and $B \sim B_T$ in tokamak, where e is the elementary charge, B is the amplitude of the magnetic field, n_e is the electron density, T_e is the electron temperature and $\hat{\boldsymbol{B}}$ is the unit vector in the direction of the magnetic field.

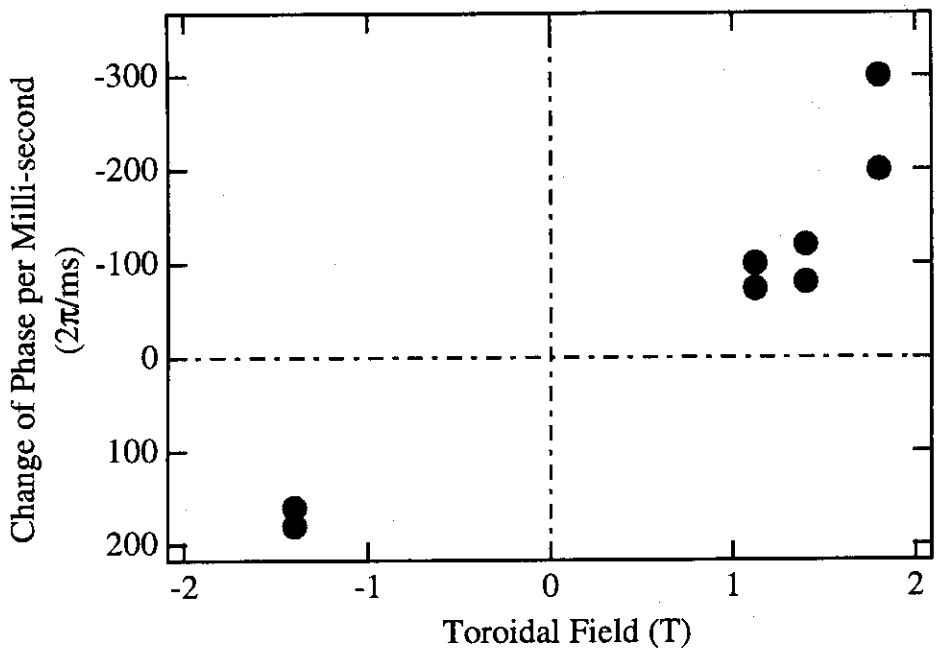

Figure 3.7: Toroidal magnetic field dependence of the runaway phase phenomena. The vertical axis is the change of fringes of the runaway phase in a milli-second. The degree of the runaway phase is proportional to the toroidal field B_T. B_T is negative when the direction of the toroidal magnetic field is counter clock-wise (CCW) viewing from the top of the torus and positive when the direction is clock-wise (CW) (see Fig. 2.1) . The direction of the I_p is always CW. The frequencies of the launched wave are 37 and 38.5 GHz.

4. Analysis

4.1 Runaway Phase Phenomena

4.1.1 Observed Characteristics

The phenomena of runaway phase do not depend on a specified detection systems. We have checked this by using two most major kinds of detection system. Our heterodyne system is the simplest. More complicated reflectometers such as AM (amplitude modulation) system [107], super heterodyne system [103], PLL (phase lock loop) heterodyne system [49] also suffer from the runaway phase phenomenon.

The step-like runaway phase can be often seen in H-mode phase, however the most of the runaway phase occurs in the gradual manner in OH phase and L-mode phase. Fig. 4.1 shows details of a typical runaway phase. The runaway phase is not step-like or "fringe jump". Instead the phase gradually changes. The amplitude is relatively small when a fast change of the phase occurs, but the level of the small amplitude is well above the noise level of the reflectometer system, 50 mV, which is a feature of the fast change of the power of the reflected wave.

The movement of the plasma has been detected when we process the data set of cosine and sine by low pass filter.

These facts suggest that the reflected wave can be expressed as the sum of two components; one being a WKB solution Eq. 1.3 and the other a series with each term having a frequency $\omega_0 + \Omega_s$. The waveform at the detector is expressed in the form,

$$E_R = E_0 \exp(i\varphi_0) + \sum_s E(\Omega_s) \exp i(\Omega_s t + \varphi_s), \tag{4.1}$$

because the detector excludes the high frequency component $\exp(i\omega_0 t)$ whose frequency ω_0 is same with that of the incident wave. Here φ_0 is $\varphi(f_0)$ in Eq. 1.4, the values of $E(\Omega_s)$ and φ_s are the amplitude and initial phase of the wave with the frequency of $\omega_0 + \Omega_s$, respectively. We measure the real part of the above expression as cosine and the imaginary part as sine.

The runaway phase can occur when the contribution of the term(s) other than the first term is larger than that of the first term, i.e. $E(\Omega_s) > E_0$.

For example, if we assume the following expression:

$$E_R = \exp(i\varphi_0) + 1.2 \times \exp i(\omega_1 t + \varphi_1), \tag{4.2}$$

the simulated time evolution of the phase and amplitude is shown in Fig. 4.2 (we set $f = \omega_1/2\pi$ 100 kHz.). This waveform is very similar to the waveform of the typical

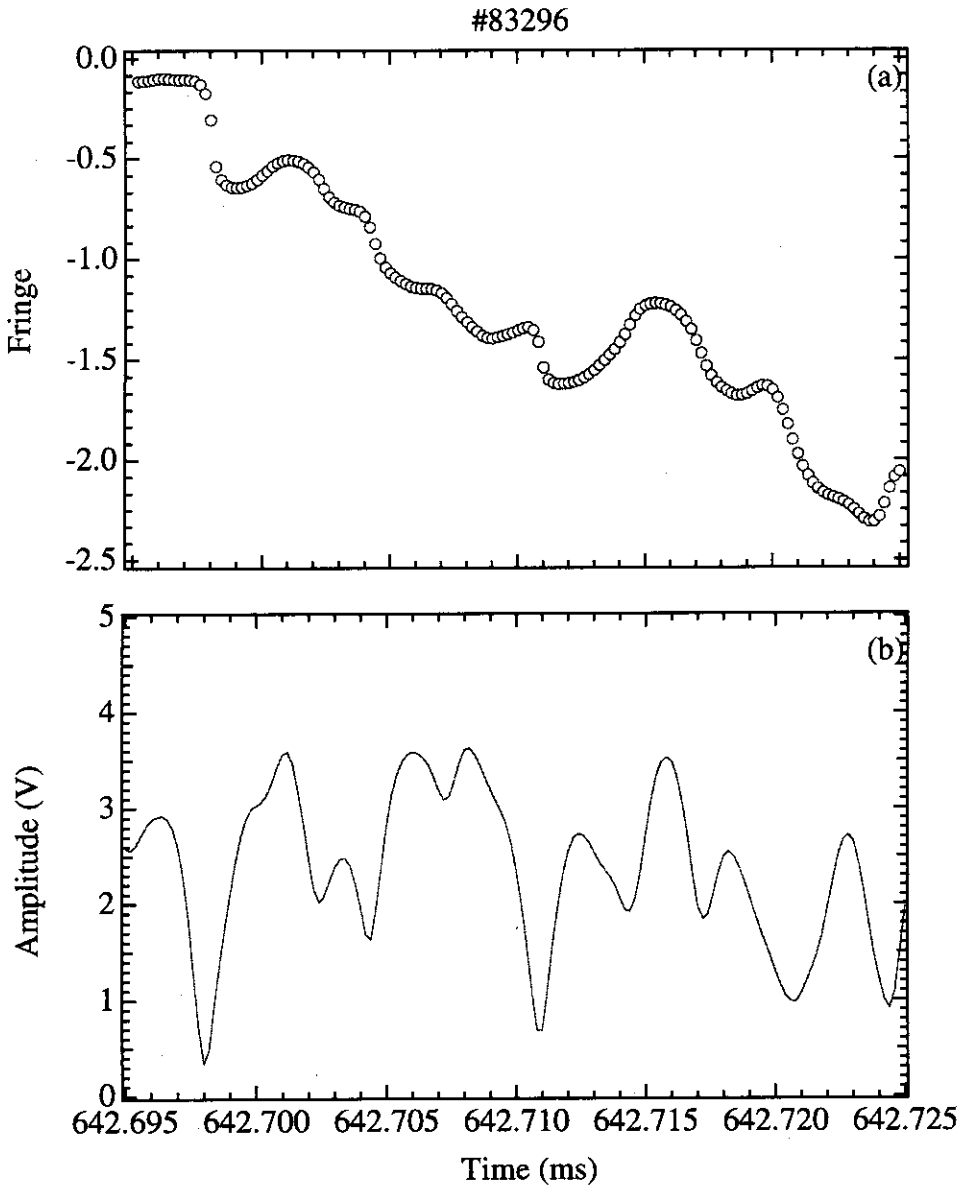

Figure 4.1: Typical gradual runaway measured by the reflectometer. (a) shows the change of the phase by the fringe. (b) shows the change of the amplitude of the reflected wave. The runaway phase is not "fringe jump". The phase gradually changes. The amplitude is relatively small when the fast change of the phase occurs, but the level of the small amplitude is enough above noise level of the reflectometer system.

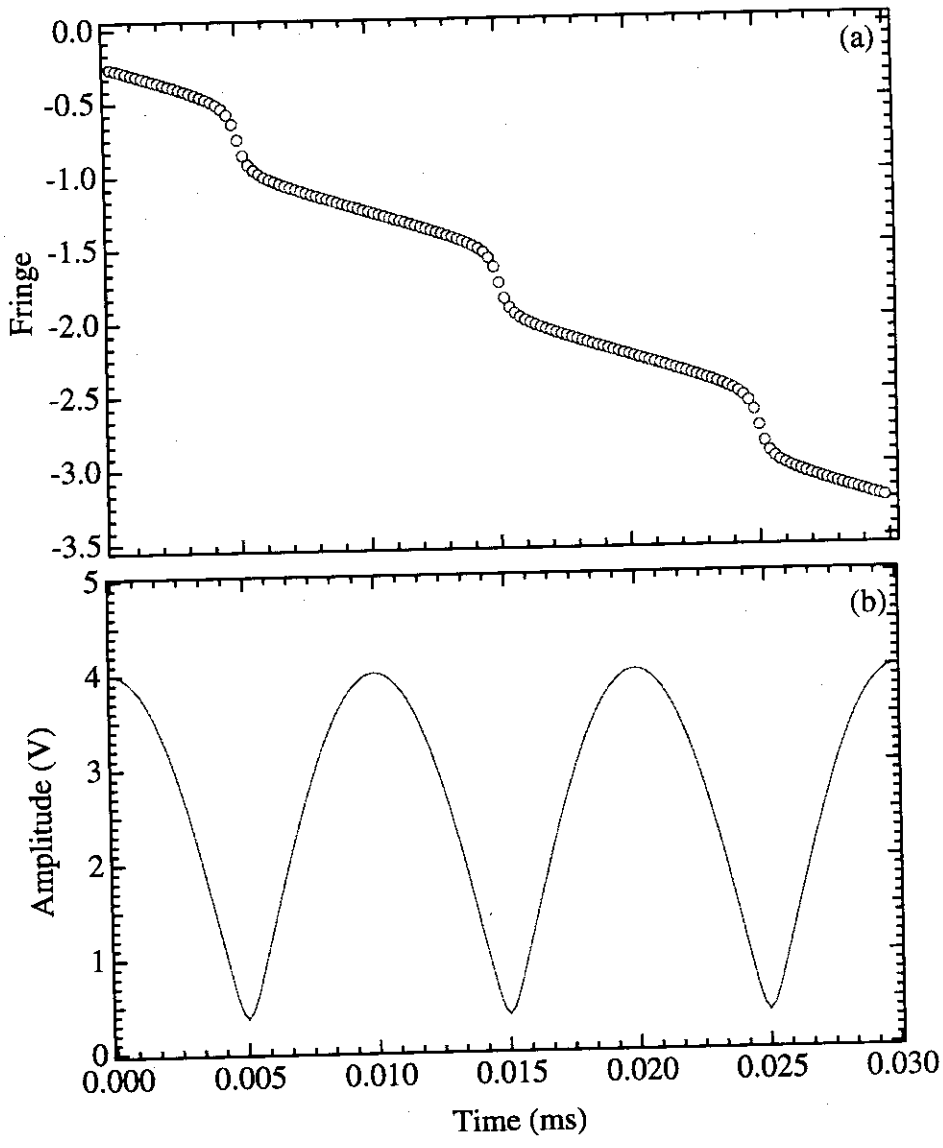

Figure 4.2: The simulated time evolution of phase, (a), and amplitude, (b). The phase change is shown by the fringe.There exist periodical fast changes as the phase changes. The period is $2\pi/\omega_1 = 10\mu$s. The amplitude is relatively small at that time but is enough above the noise level of the experiment.

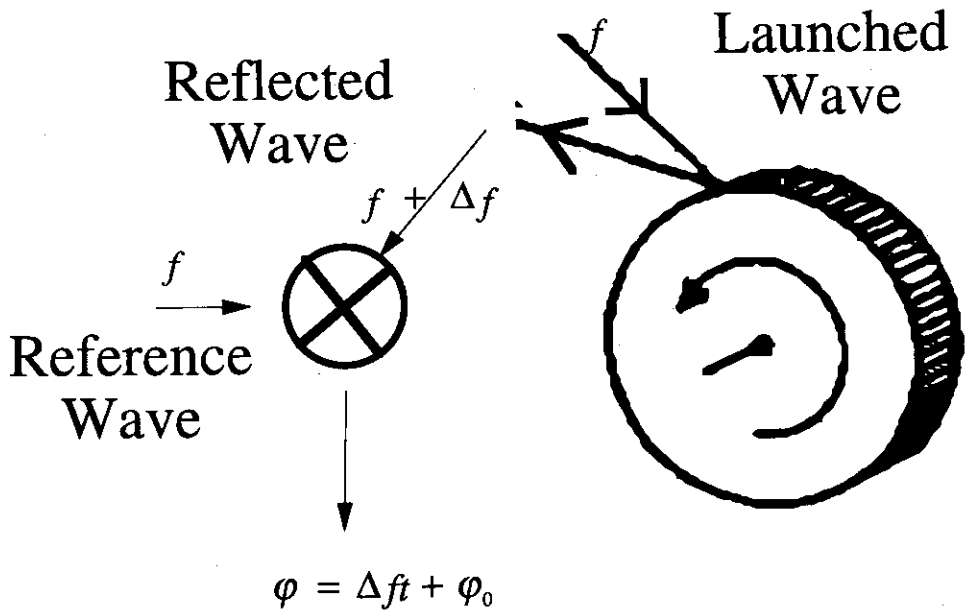

Figure 4.3: Principle of Doppler wheel. This is also called the rotating grating. The wave or light is launched into the rotating grating. The wave is reflected by the reflector coming, in this figure, and goes back to the wave source. The frequency of the reflected wave is upshifted by the Doppler effect.

gradual runaway phase as shown in Fig. 4.1. The change of the simulated amplitude also resembles the observed change of the reflected wave.

We can see the change of the phase of the first term, if we process Eq. 4.1 with the low pass filter whose cut-off frequency is less than ω_1. This means the slow movement can be seen by using the low pass filter and is consistent with our results.

The expression of Eq. 4.1 is plausible when there is the scattering of the density fluctuation because the frequency of the scattered wave is changed by the frequency Ω_s of the fluctuation. In this situation, the first term comes from the normal reflected wave, other terms come from the scattering.

It may be considered that the cause of the runaway phase is a Doppler shift due to a rotating structure like a Doppler wheel (Fig. 4.3). However, the results of the 50 GHz homodyne/heterodyne system can not be explained by this model because the antenna is set on the very mid-plane (see Fig. 2.2) and the beam width of the incident wave at the cut-off layer is as narrow as $\sim$ 3cm. Further, the runaway phase phenomena have been observed even in the early time of the discharge, when there is no cut-off layer.

The treatment of Eq. 1.13 is inappropriate. We reconsider the principle of the reflectometer and the interaction between the wave and the plasma. Next the appropriate treatment of the data with the runaway phase is discussed and applied to the experimental data. We call the normal reflected wave, i.e. the first term of Eq. 4.1, as the coherent

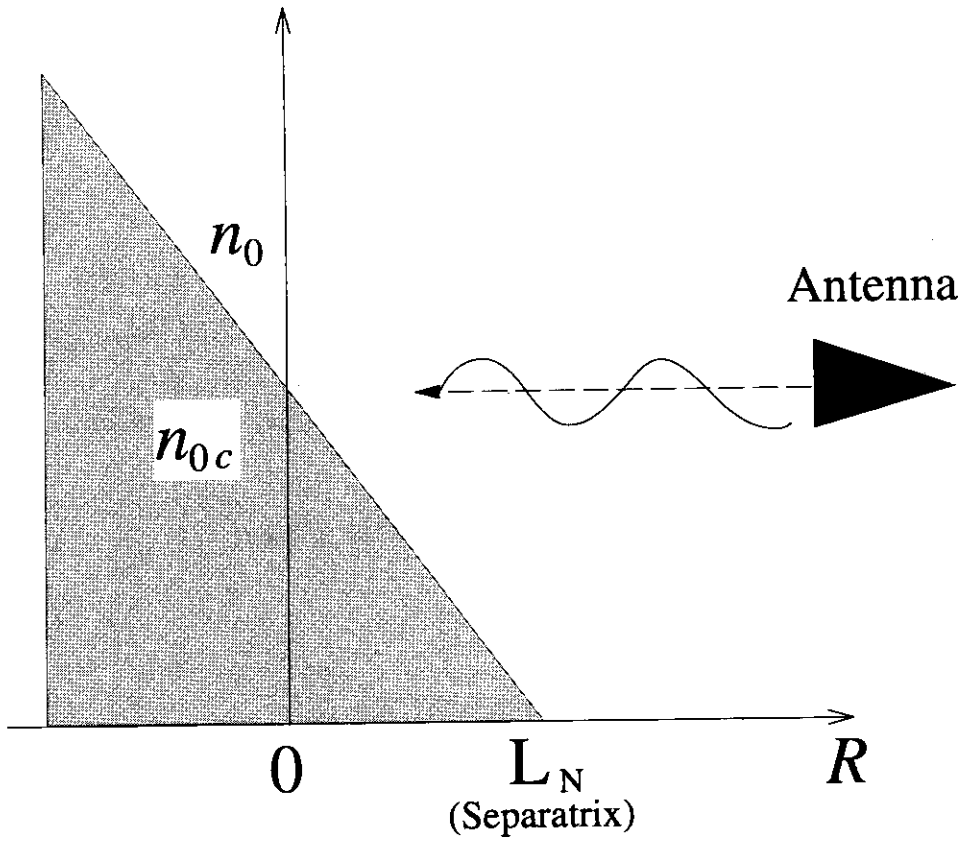

Figure 4.4: Assumed density profile.

wave and others, i.e. the other terms of Eq. 4.1, as the incoherent waves.

4.1.2 Formalism of the Reflected Wave

Born Approximation

Equation 1.13 coming from geometrical optics cannot express the runaway phase. The fluctuation of the phase difference is proportional to the density fluctuation. The phase changes only around the zero level and does not increase or decrease monotonically.

We investigate the effect of the density fluctuation on the reflected wave by solving Eq. 4.3 using the Born approximation.

$$\frac{d^2E}{dR^2} + (\varepsilon_O + \tilde{\varepsilon})k_0^2 E = 0. \tag{4.3}$$

Here ε_O is the dielectric constant of plasma for O-mode in the situation in which the density profile is written as $n_0 = n_{0c}(1 - R/L_N)(R < L_N)$ and $n_0 = 0(R \geq L_N)$, where n_{0c} is the cut-off density (Fig. 4.4). This is a good approximation as seen from the density profile measured by TV thomson scattering system. $\tilde{\varepsilon}$ is the perturbed dielectric constant induced by the density fluctuations. We set $E = E_0 + E_s$. E_0 is the coherent wave and E_s is the perturbed incoherent wave by fluctuations.

When we assume $\varepsilon_O \gg \tilde{\varepsilon}$ and $E_0 \gg E_s$, we can obtain the two equations of the first Born approximation:

$$\frac{d^2E_0}{dR^2} + \varepsilon_O k_0^2 E_0 = 0, \tag{4.4}$$

$$\frac{d^2E_s}{dR^2} + \varepsilon_O k_0^2 E_s = -\tilde{\varepsilon} k_0^2 E_0. \tag{4.5}$$

The solution of Eq.4.4 can be expressed using the Airy functions A_i, B_i [138]. We express this solution by $E_{0v}\psi_1$, E_{0v} being the amplitude of the electric field of the launched wave, according to the expression of Ref. [109].

Eq. 4.5 is solved by using the method of Variation of Parameters, the solution being given by

$$E_s(R,\omega_s) \sim c(R)\int_{-\infty}^{R} \tilde{\varepsilon} {k_0}^2 E_0 \frac{\psi_1}{W} dx \qquad (R \gg L_N) \tag{4.6}$$

$$= c(R) E_{0v} {k_0}^2 \int_{-\infty}^{R} \tilde{\varepsilon} \frac{\psi_1^2}{W} dx \tag{4.7}$$

$$= 4\pi c(R) r_0 E_{0v} \int_{-\infty}^{R} \tilde{n}(x, \omega_s - \omega_0) \frac{\psi_1^2}{W} dx \tag{4.8}$$

where $r_0 = e^2/4\pi\varepsilon_O m_e c^2$, the classical electron radius, W is the Wronskian of the solution of Eq. 4.4 and $c(R)$ is a linear combination of the Airy functions normalized to unit amplitude in the vacuum region. The scattered wave $E_s(R,\omega_s)$ mainly brings back the information of the density fluctuation in the vicinity of the cut-off layer [139] because ψ_1^2/W is swelling in the vicinity of the cut-off as shown in Fig. 4.5. Equation 4.8 shows us that the perturbed wave by the density fluctuation is essentially the scattered wave. The ensemble average of $E_s(R,\omega_s){E_s}^*(R,\omega_s')$ gives the selection rule of the wavenumber. In WKB approximation, the selection rule become $K = 2k_0\sqrt{x/L_N}$, where K is a wavenumber of the density fluctuation. This is the Bragg condition in the 1 D scheme because the wavenumber of launched wave become $k_0\sqrt{x/L_N}$. If we use the Airy functions coming from the Born approximation, the selection rule is not so well-defined. But the contribution of the low K holds large in the vicinity of the cut-off layer [112, 140].

At this point we try to correlate the result of the Born approximation, Eq. 4.8, and the intuitive result obtained from the geometrical optics, Eq. 1.13.

When $E_0 \gg E_s$ in the Born approximation, the phase of $E = E_0 + E_s$ is expressed by

$$\tilde{\varphi} = \mathrm{Im}[E_s(x,\omega_s)/E_0]$$

$$= -2k_0^2 \mathrm{Re}\left[\int \tilde{\varepsilon}\frac{\psi_1^2}{W} dx\right]. \tag{4.9}$$

Theoretical analysis has been done by using this expression [109, 122]. When we change ψ_1^2/W to $1/2\sqrt{\varepsilon_O}k_0$, we obtain the expression,

$$\tilde{\varphi} = -2k_0 \int \tilde{\varepsilon}\frac{1}{2\sqrt{\varepsilon_O}} dx$$

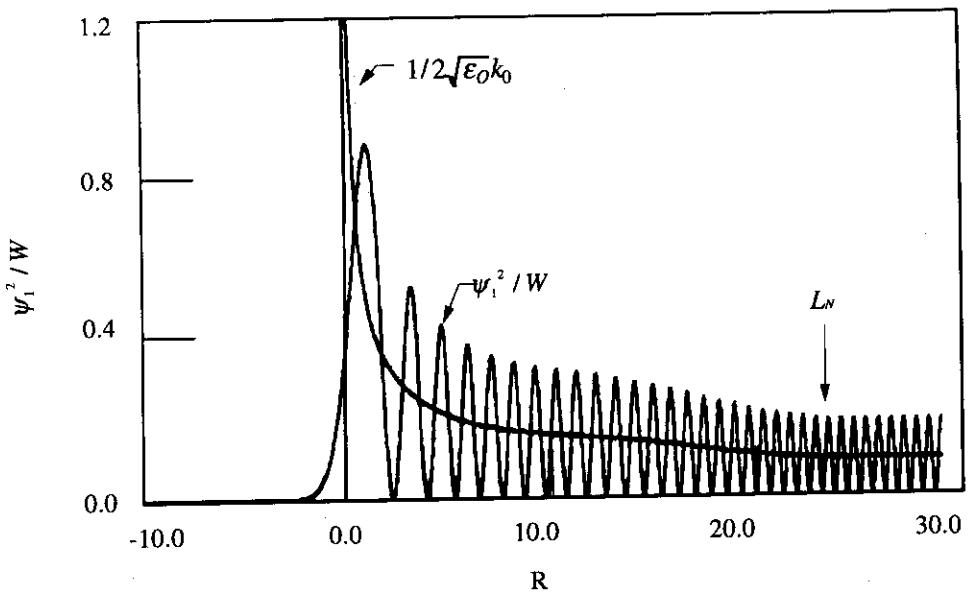

Figure 4.5: The weighting function ψ_1^2/W is compared with the corresponding WKB approximation $1/2\sqrt{\varepsilon_O}k_0$. ψ_1^2/W swells in the vicinity of the cut-off, R = 0. R is normalized by the wavelength in this figure. (quoted from Ref. [109])

$$= -2k_0 \int \sqrt{\varepsilon_O + \tilde{\varepsilon}}dx + 2k_0 \int \sqrt{\varepsilon_O}dx. \tag{4.10}$$

The waveform of ψ_1^2/W and $1/2\sqrt{\varepsilon_O}k_0$ are as shown in Fig. 4.5. The last expression of Eq. 4.10 has the form based on geometrical optics (Eq. 1.4).

It is plausible that the runaway phase comes from the scattering of the density fluctuation, but the condition of $E_0 \gg E_s$ in the above scheme prevents the occurrence of the runaway phase phenomena.

It is difficult for the runaway phase to exist in the one dimensional scheme even if $E_0 < E_s(\Omega)$, because $E_s(\Omega) = E_s(-\Omega)$ in this scheme and the complex amplitude of

$$E_0 + E_s(\Omega)e^{i\Omega t+\varphi_+} + E_s(-\Omega)e^{-i\Omega t+\varphi_-} \tag{4.11}$$

draws the line, $y = tan((\varphi_+ + \varphi_-)/2)(x - E_0)$, on the Gaussian plane as shown in Fig. 4.6. Here $E_s(\Omega)$ is the Fourier component with the frequency, $\Omega = \omega_s - \omega_0$, of the reflected wave at the detector. Some noise on the experiment can trigger the fringe jump in the bipolar direction because the noise broaden the above line as shown in Fig. 4.6, but the runaway phase phenomena in which the phase increase in a one-sided direction does not occur.

Therefore, for the runaway phase to occur, the following conditions must be satisfied:

$$E_s \gtrsim E_0, \tag{4.12}$$

$$E_s(\Omega) \neq E_s(-\Omega). \tag{4.13}$$

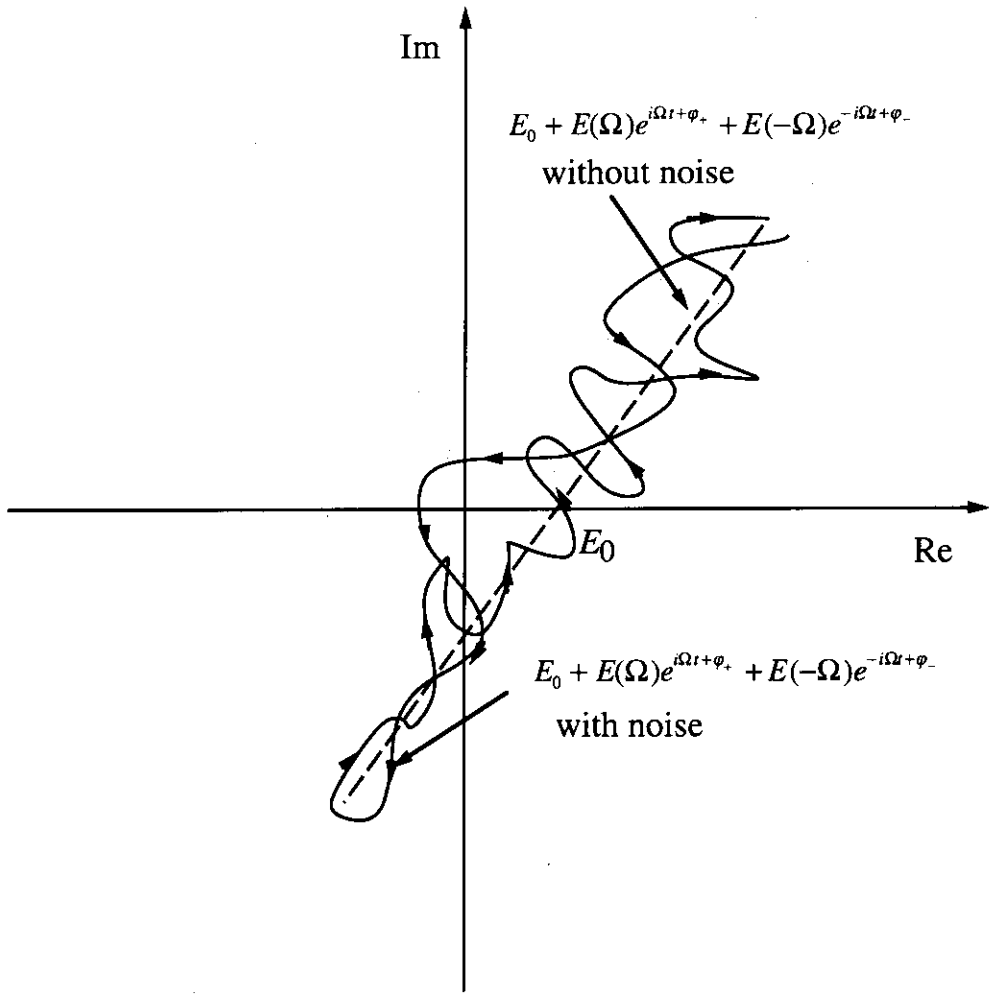

Figure 4.6: Trajectory of the $E_0 + E_s(\Omega)e^{i\Omega t+\varphi+} + E_s(-\Omega)e^{i\Omega t+\varphi-}$ without noise is drawn by the dashed line. Here $E_s(\Omega) = E_s(-\Omega)$ and $E_s > E_0$. The movement on this trajectory does not increases the fringe. Trajectory of the $E_0 + E_s(\Omega)e^{i\Omega t+\varphi+} + E_s(-\Omega)e^{i\Omega t+\varphi-}$ with noise is drawn by the solid line. The noise can cause the fringe jump in the situation of $E_s > E_0$. The fringe increases by one fringe in this figure.

We now investigate a three dimensional scheme from the view point of the basic process of the scattering in order to achieve these conditions.

Scattered Wave

The electron temperature is about 1 keV in the plasma of JFT-2M. The value of v_{th}/c is less than 0.05, where v_{th} is the electron thermal velocity and thus the relativistic effect is negligible. In this situation, the electric field radiated by the accelerated electron is

$$E_s(\boldsymbol{R}\ ,t) = -\frac{e}{c}\left[\frac{\hat{\boldsymbol{R}}\ \times(\hat{\boldsymbol{R}}\ \times\dot{\boldsymbol{\beta}}\ )}{R}\right]_{retarded}, \tag{4.14}$$

where $\boldsymbol{\beta}\ = \boldsymbol{v}\ /c, \hat{\boldsymbol{R}}\ = \boldsymbol{R}\ /R$ [27, 29, 141] . The acceleration of the electron by the incident wave, $\boldsymbol{E_i}\ (\boldsymbol{x}\ ,t) = \boldsymbol{E_i}\ e^{i\boldsymbol{k}_0\cdot\boldsymbol{x}\ -i\omega t}$, is $\dot{\boldsymbol{\beta}}\ = \frac{e}{mc}\boldsymbol{E_i}\ e^{i\boldsymbol{k}_0\cdot\boldsymbol{x}\ -i\omega t}$. Substituting this into Eq. 4.14, multiplying this by the distribution function and integrating this, we get the scattered wave,

$$\boldsymbol{E_s(R,t)}\ = \frac{r_0}{R}\int_V d^3r n(\boldsymbol{r}\ ,t')\hat{\boldsymbol{R}}\ \times[\hat{\boldsymbol{R}}\ \times\boldsymbol{E_i}\ (\boldsymbol{r}\ ,t')], \tag{4.15}$$

where t' is retarded time. By performing a Fourier transform in time, we obtain,

$$\boldsymbol{E_s}\ (\boldsymbol{R}\ ,\omega_s) = [\hat{\boldsymbol{R}}\ \times(\hat{\boldsymbol{R}}\ \times\hat{\boldsymbol{E_i}}\ )]\frac{r_0}{2\pi R}\int_{-\infty}^{\infty}\tilde{n}(\boldsymbol{r}\ ,\omega_s-\omega_0)\boldsymbol{E_i}\ (\boldsymbol{r}\ ,t)d\boldsymbol{r}\ . \tag{4.16}$$

If we use the wave near cut-off as the incident wave $\boldsymbol{E_i}\ (\boldsymbol{r}\ ,t)$, this equation describes the scattered wave at the cut-off.

The ratio of the amplitude E_s of the scattered wave by the density fluctuation $\tilde{n}(\boldsymbol{K}\ ,\Omega)$, to the amplitude $E_{non-scattered}(\equiv({E_0}^2+{E_s}^2)^{1/2})$ of the reflected wave when there is no scattered wave by the density fluctuation is given by

$$\begin{aligned}\left|\frac{E_s}{E_{non-scattered}}\right| &\sim r_0\lambda_0\,|\tilde{n}(K,\Omega)|\,A_i(z\approx 0)L_{scatter}/2\\ &= \frac{r_0\lambda_0 n_c L_{scatter}A_i(z\approx 0)\sqrt{2}}{2}\left.\frac{\tilde{n}(K,\Omega)}{n_c}\right|_{rms}\\ &\sim 10\left.\frac{\tilde{n}(K,\Omega)}{n_c}\right|_{rms},\end{aligned} \tag{4.17}$$

where λ_0 is the vacuum wavelength of the incident wave, $L_{scatter}$ is the characteristic length of the scattering volume in the direction to which the wave propagates,

$$\left.\frac{\tilde{n}(K,\Omega)}{n_c}\right|_{rms} \equiv \sqrt{\left\langle\left|\frac{\tilde{n}(K,\Omega)}{n_c}\right|^2\right\rangle}.$$

We have used no approximation about the amplitude such as the Born approximation, $E_s \ll E_0$. We can achieve the condition of Eq. 4.12, but we can not use the expression of

Eq. 4.17 in the region where the density fluctuation is relatively large, because the ratio of Eq. 4.17 exceeds 1 when the density fluctuation is larger than 10 %. The reason is that the amplitude of the incident wave, which is scattered by the fluctuation, is fixed in the estimation of the integral over the scattering volume. The amplitude of the incident wave will be smaller as the incident wave propagates in the scattering volume. Taking this effect into consideration by renormalization, we estimate the ratio to be,

$$\left|\frac{E_s}{E_{non-scattered}}\right| \sim 10\left.\frac{\tilde{n}(K,\Omega)}{n_c}\right|_{rms} \Big/ \left[\left(10\left.\frac{\tilde{n}(K,\Omega)}{n_c}\right|_{rms}\right)^2+1\right]^{1/2}, \tag{4.18}$$

which does not exceed 1.

Equation 4.18 produces,

$$\left|\frac{E_s}{E_0}\right| \sim 10\left.\frac{\tilde{n}(K,\Omega)}{n_c}\right|_{rms}. \tag{4.19}$$

When the density fluctuation level is larger than 10 %, the runaway phase can occur because Eq. 4.12 is satisfied. This density fluctuation level can explain the reason why the density fluctuation level estimated by the phase data in the non-runaway phase period has been limited to about 10 % in our case. The runaway phase occurred and the method could not be used when the density fluctuation level exceeded 10 %.

As the equation of $E_s(\Omega) = E_s(-\Omega)$ is satisfied, one dimensional scattering does not cause the runaway phase as mentioned above. However usually $E_s(\Omega)$ is not equal to $E_s(-\Omega)$ in two-dimensional scattering case. When the incident wave $E_i(\boldsymbol{k_0}, \omega_0)$ is scattered by the density fluctuation $\tilde{n}(\boldsymbol{K}, \Omega)$, the scattered wave $E_s(\boldsymbol{k^s}, \omega_s)$ fulfill the following condition:

$$\begin{cases} \omega_s = \omega_0 + \Omega \\ k^s_\perp = K_\perp \end{cases} \tag{4.20}$$

or

$$\begin{cases} \omega_s = \omega_0 - \Omega \\ k^s_\perp = -K_\perp \end{cases}, \tag{4.21}$$

where $k^s_\perp$ is the component of $\boldsymbol{k^s}$ perpendicular to $\boldsymbol{k_0}$, $K_\perp$ is the component of $\boldsymbol{K}$ perpendicular to $\boldsymbol{k_0}$ [29]. $E(\Omega) \neq E(-\Omega)$ if $\tilde{n}(K_\perp) \neq \tilde{n}(-K_\perp)$. The position and direction of the antenna decide the $\boldsymbol{k^s}$ to be detected and the corresponding frequency shift caused by the density fluctuation $\tilde{n}(\boldsymbol{K}, \Omega)$. This is the principle of the conventional scattering system.

The antenna has a finite aperture and the microwave beam has a finite beam width. The scattered waves of $E_s(\Omega)$ and $E_s(-\Omega)$ caused by the same fluctuation with relatively small wavenumber $K_\perp$ can be completely detected as shown in Fig. 4.7. However as the wavenumber becomes larger, the corresponding scattered waves of $E_s(\Omega)$ and $E_s(-\Omega)$ can be partially detected, as the waves partially move out of the field of view of the antenna. In this case, the slight tilting of the cut-off layer produces the condition of

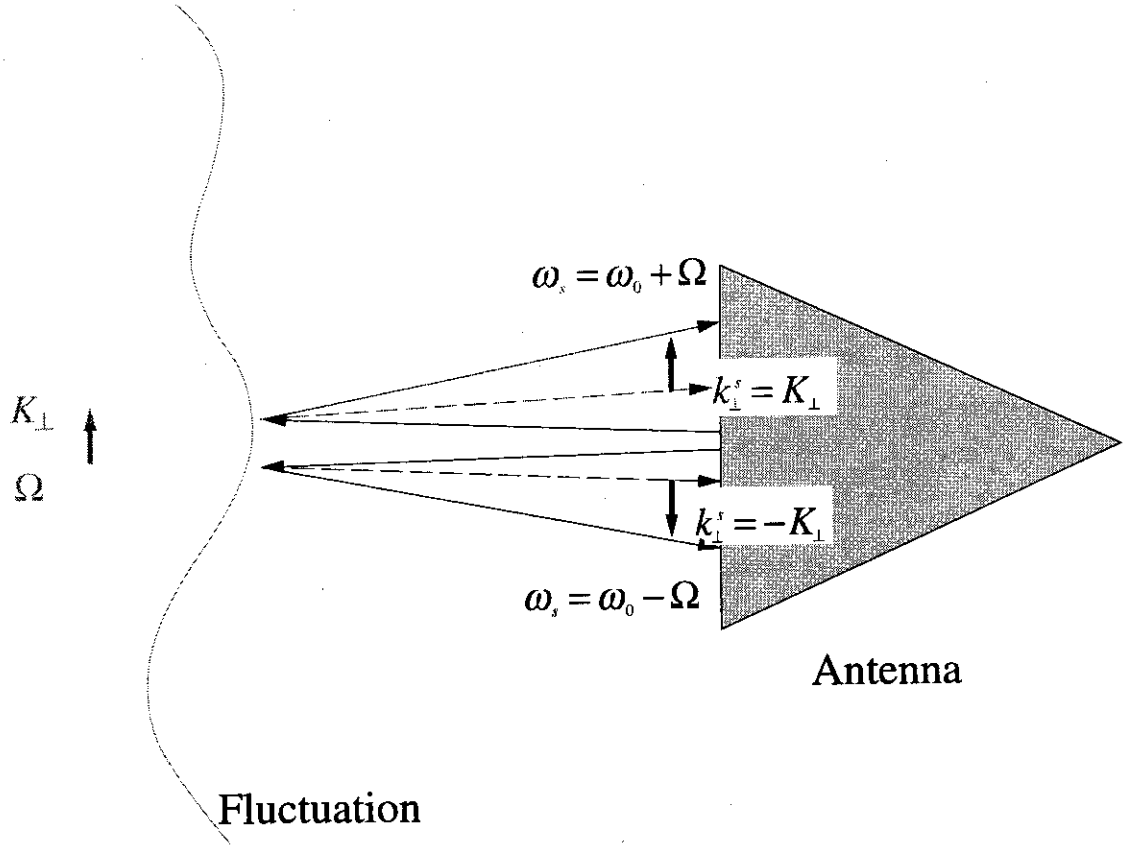

Figure 4.7: The antenna has a finite aperture and the microwave beam has a finite beam width. The scattered waves of $E_s(\Omega)$ and $E_s(-\Omega)$ caused by the same fluctuation with relatively small wavenumber can be completely detected. However as the wavenumber becomes larger, the corresponding scattered waves of $E_s(\Omega)$ and $E_s(-\Omega)$ can be partially detected, as the waves partially move out of the field of view of the antenna.

$E_s(\Omega) \neq E_s(-\Omega)$. The situation is unavoidable in the realistic experimental environment. Here the situation is referred to as the "microscopic" misalignment and the situation in which only one of $E_s(\Omega)$ or $E_s(-\Omega)$ is detected as the "macroscopic" misalignment. The Doppler wheel system is an example of "macroscopic" misalignment.

There are two-dimensional simulations that show that the fluctuations with $K_\perp$ cause the runaway phase [108, 117]. They have stated that misalignment of the antennas could result in the runaway phase. The situation of their simulation is the "macroscopic" misalignment.

Some people say the "macroscopic" misalignment is essential to the runaway phase. They consider the runaway phase will disappear and the correct measurement can be performed in the correct alignment.

This statement is not correct. The correct measurement can not be performed even if the correct alignment is established. The runaway phase phenomena occur under two conditions. One is $E_s > E_0$, which is the result of relatively large density fluctuations. The other is $E_s(\Omega) \neq E_s(-\Omega)$ due to the misalignment of the antenna. Thus even if the perfect alignment is established, the effect of the scattered wave, $E_s > E_0$, remains and the trajectory of the data set which consist of cosine and sine draws a line as mentioned above (Fig. 4.6). In this case, the reflected power varies largely in time and the change of the phase does not show the density fluctuation correctly. Therefore the correct measurement is not possible even if the runaway phase looks like to disappear due to the correct alignment.

However we need not discard such data. We can treat the data as the signal of the scattered wave even though the runaway phase phenomena occur. And even in this case, the localization of the reflectometer holds because of the swelling effect of the incident wave near the cut-off.

4.1.3 Runaway Phase without Cut-off Layer

Scattering can occur if the Bragg condition is satisfied [112, 140]. The incident wave propagates with the wavelength $\lambda_0/\sqrt{\varepsilon} \sim 1 - 1.5\lambda_0$ when there is no cut-off layer. The Bragg condition is satisfied if there are density fluctuations with the wavelength of $\sim 0.5 - 0.75\lambda_0$. In this situation, there is no coherent component and all the received signals consist of the waves scattered by the density fluctuations. The received signals cause the runaway phase.

4.1.4 Desired Arrangement of Antenna

We conclude that the runaway phase is caused by the wave scattered by the large density fluctuations propagating in a direction perpendicular to the direction in which the incident wave is propagating. In order to avoid the effect of the density fluctuations, the arrangement of the antenna must satisfy the following condition:

$$R \geq \frac{k_0}{K_{\perp,min}} L_{antenna}, \tag{4.22}$$

where R is the distance between the cut-off layer and the antenna, $L_{antenna}$ is the characteristic length of the antenna aperture, k_0 is the amplitude of the wavenumber of the incident wave, $K_{\perp,min}$ is the minimum wavenumber of the incoherent wave, whose amplitude is greater than the amplitude of the coherent wave, perpendicular to the $\boldsymbol{k}_0$. It corresponds to the wavenumber of the density fluctuation which cause this incoherent wave. In this condition, the two-dimensional effect such as the runaway phase and the large change of the reflected power can be reduced by avoiding the effect of the wave scattered by the density fluctuations with $K_{\perp,min}$.

$L_{antenna}$ is usually about $10\lambda_0$. The distance between the cut-off and the antenna needs 1 m if $\lambda_{\perp,min}(= 2\pi/K_{\perp,min})$ is 0.1 m.

4.1.5 Interpretation of Non-runaway Phase Period

The trajectory of the complex amplitude, $E(\Omega)e^{i\Omega t+\varphi_+} + E(-\Omega)e^{-i\Omega t+\varphi_-}$, of the scattered wave in the Gaussian plane does not show an arc shape. Its trajectory is an ellipse or a line. This non-arc shape is observed in the trajectory of the reflected wave in the non-runaway phase period as shown Fig. 4.8.

The arc shape is the characteristic of geometrical optics. Geometrical optics describes the global movement of the plasma; namely the global changes of the dielectric constant ε_O rather than the perturbation of the dielectric constant $\varepsilon_O + \tilde{\varepsilon}$.

The precursor of the sawtooth crash causes the perturbation with poloidal mode number $m = 1$,which leads to the global change of the density profile. The arc shape is observed when the precursor of the sawtooth occur as shown in Fig. 4.9.

The same arch shape is observed when plasma moves if there is no runaway phase, as shown in Fig. 4.10

In the non-runaway phase period, the feature of the Born approximation is clearly revealed. The reflected wave consists of the coherent component which is explained by the geometrical optics and the relatively small incoherent wave which is caused by the density fluctuation,

$$E_R = E_0 \exp(i(\omega_0 t + \varphi_0)) + \sum_s E(\Omega_s) \exp i((\omega_0 + \Omega_s)t + \varphi_s). \tag{4.23}$$

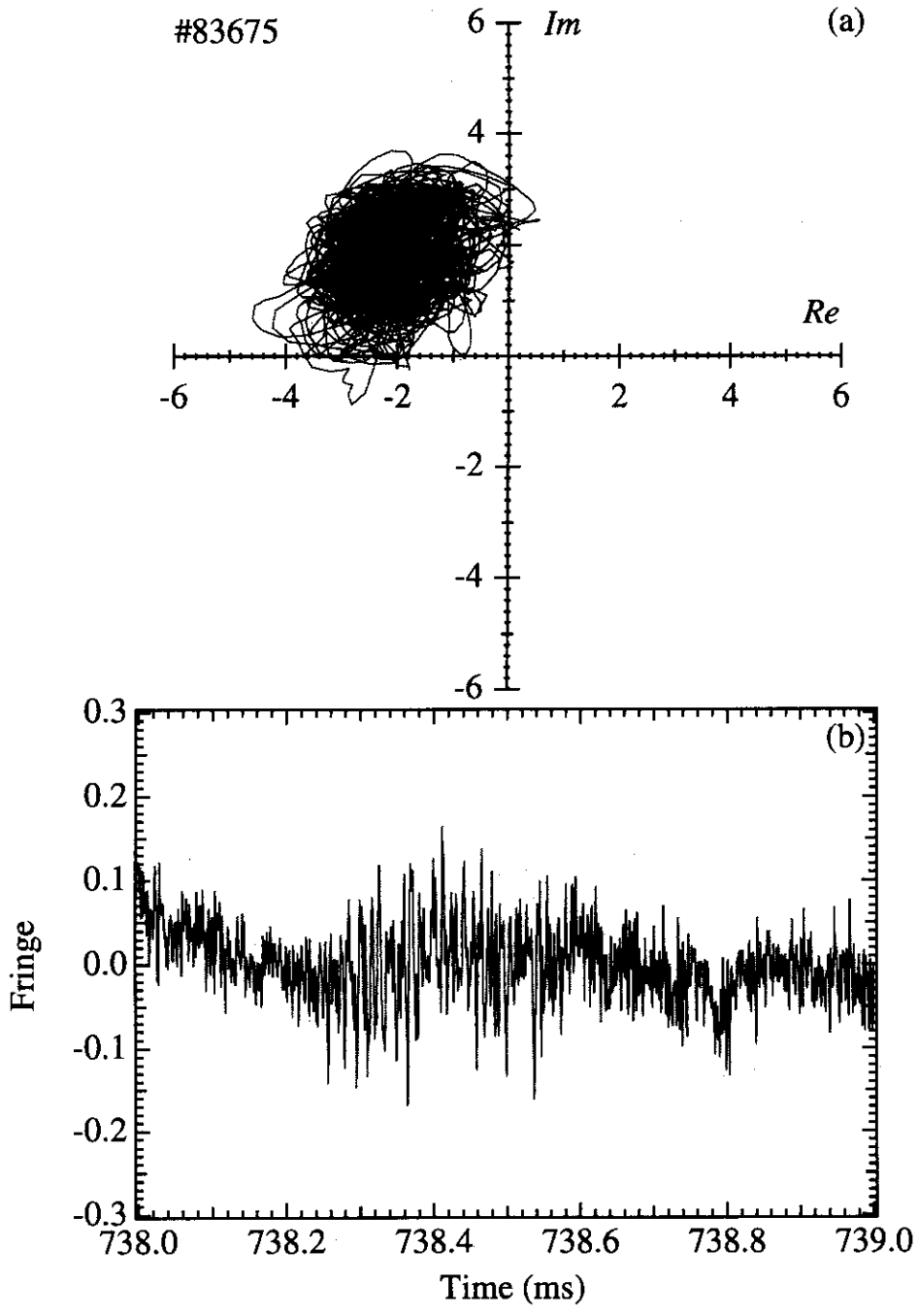

Figure 4.8: (a) Trajectory of the complex amplitude in the non-runaway phase period. (b) Time evolution of the phase in the same period as in (a). The cut-off density is $1.84 \times 10^{19}\mathrm{m}^{-3}$.

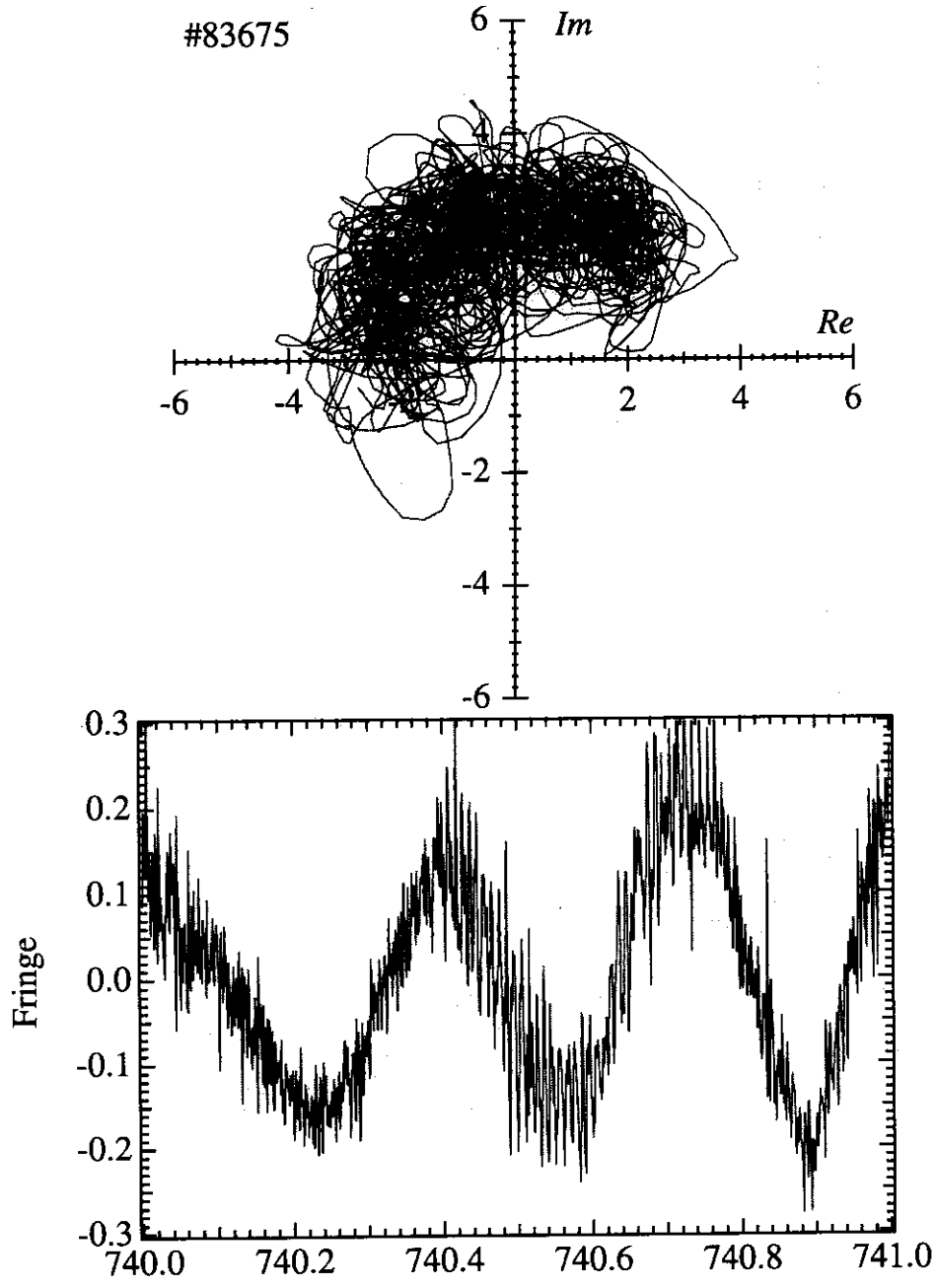

Figure 4.9: (a) Trajectory of the complex amplitude when the precursor of the sawtooth occurs. (b) Time evolution of the phase in the same period as in (a). The cut-off density is $1.84 \times 10^{19}\mathrm{m}^{-3}$.

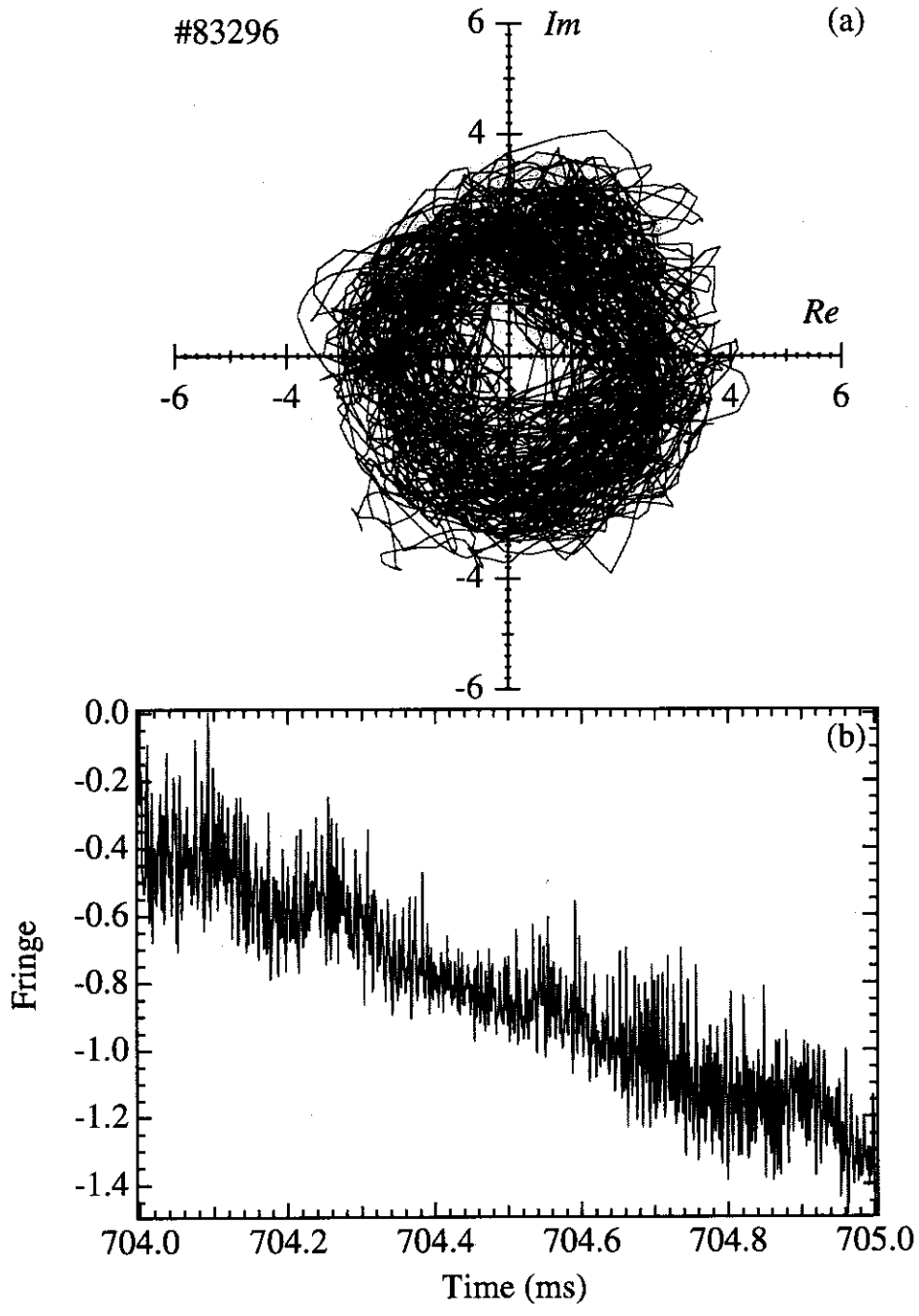

Figure 4.10: (a) Trajectory of the complex amplitude when the plasma moves. (b) Time evolution of the phase in the same period as in (a). The plasma has been actively moved by about 8mm in this period. This movement corresponds to the change of the phase by 1 fringe. The cut-off density is $1.79 \times 10^{19}\mathrm{m}^{-3}$.

However, the fluctuations of the phase of the reflected wave can be considered as the density fluctuations as mentioned above (Eq. 4.9 and 4.10). The analysis using the data of the non-runaway phase is consistent with the interpretation of the runaway phase.

4.2 Spectrum Analysis of the Reflected Wave

Following our earlier arguments, we should treat data as a scattered wave. The homodyne signals, $\sum_{\Omega=-\infty}^{\infty} E(\Omega)\cos(\Omega t+\varphi_\Omega)$, give us some information about the density fluctuation. However, the important quantity to measure the density fluctuation is $E(\pm\Omega)$. $E(\Omega)$ and $E(-\Omega)$ cannot be separated in the homodyne signal. In order to separate them to obtain $E(\pm\Omega)$, we must treat two independent signals, $\sum_{\Omega=-\infty}^{\infty} E(\Omega)\cos(\Omega t+\varphi_\Omega)$ and $\sum_{\Omega=-\infty}^{\infty} E(\Omega)\sin(\Omega t+\varphi_\Omega)$; namely we must treat the complex amplitude, $\sum_{\Omega=-\infty}^{\infty} E(\Omega)\exp i(\Omega t+\varphi_\Omega)$. The rotary spectrum and complex spectrum are tools for our purpose.

The rotary spectrum is convenient to analyze the rotating structure of the vector data (see Appendix C). We can see the spectrum characteristic of the runaway phase.

One of the results in the runaway phase period is shown. Figure 4.11(a) shows the clockwise (CW) spectrum $S_{CW}(f)$ and the counter clockwise (CCW) spectrum $S_{CCW}(f)$ of the reflected wave. If the "macroscopic" misalignment of the antenna causes the runaway phase phenomena, the Doppler shift of about 30 kHz would be detected. It is expected that the highest peak of the spectrum appears around 30 kHz and the peak appears in only one of the $S_{CW}(f)$ or $S_{CCW}(f)$. However, such a peak is not observed. Figure 4.11 (b) shows the difference between CCW spectrum and CW spectrum, $S_{CCW}(f)-S_{CW}(f)$. The asymmetry around 100 kHz cause the phase to advance predominantly in one direction. Figure 4.11 (c) shows the rotary coefficient $C_R(f)$. The value of $|C_R(f)|$ becomes 1 when either $E(\Omega)$ or $E(-\Omega)$ is equal to 0. The rotary coefficient $C_R(f)$ is not zero more than about 100 kHz. This fact is consistent with the model of Eq. 4.1, in which it is considered that the scattered wave brings back the information of the density fluctuation, rather than the model based on the geometrical optics, because $|C_R(f)|$ is always equal to 0 in geometrical optics except in the case of "macroscopic" Doppler shift.

The complex spectrum is the complex version of the conventional spectrum analysis (see Appendix D). The scattering feature can be detected because the positive and negative frequencies are separated in the complex spectrum unlike the spectrum of the real data. The coherence of two reflected signals from different cut-off layer can be also measured.

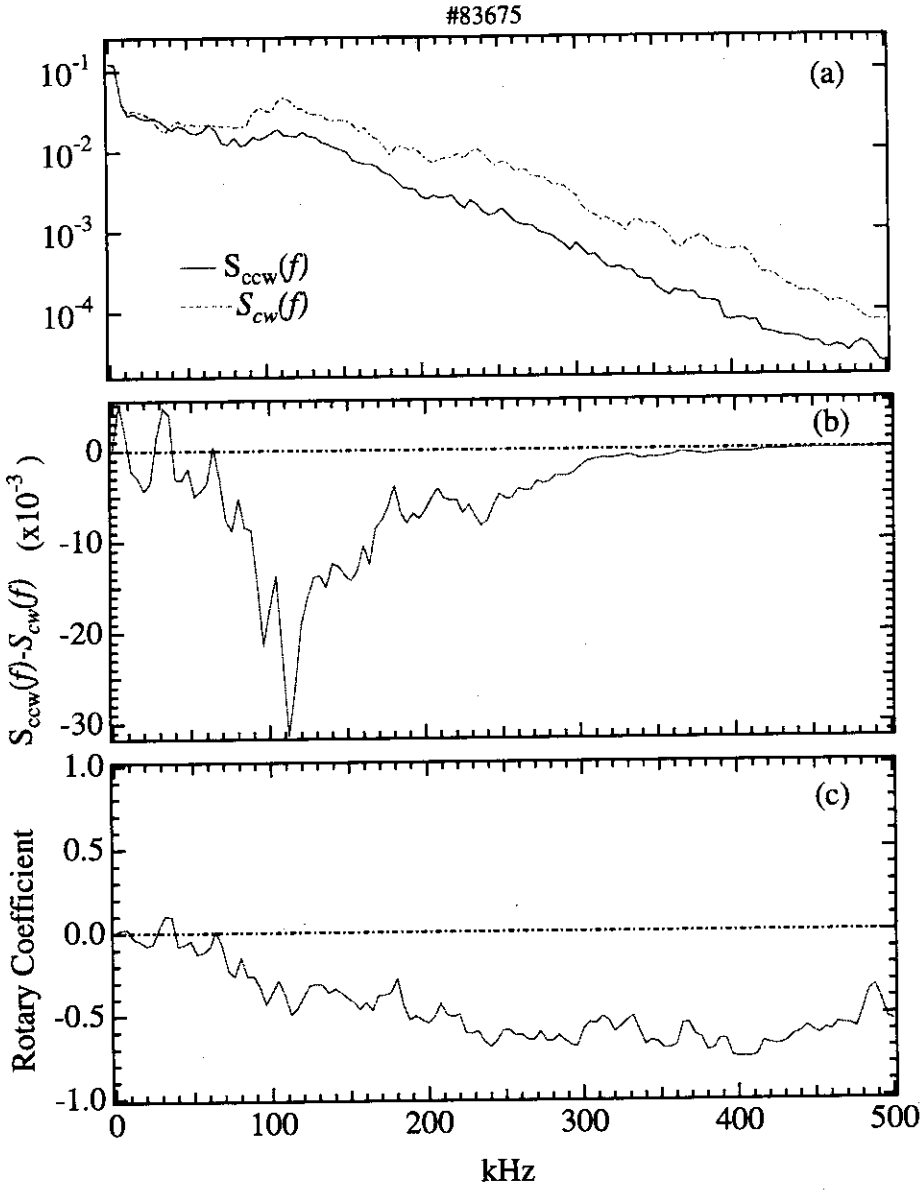

Figure 4.11: Rotary spectrum. (a) shows $S_{CW}(f)$ and $S_{CCW}(f)$ of the reflected wave by the log scale. (b) shows $S_{CCW}(f) - S_{CW}(f)$ by the linear scale. (c) shows rotary coefficient $C_R(f)$.

The fluctuation level can be estimated by rewriting Eq.4.18 as follows:

$$\left.\frac{\tilde{n}(\Omega)}{n_c}\right|_{rms} \approx 0.1 \left|\frac{E_s(\Omega)}{E_{non-scattered}}\right| \Big/ \left(1 - \left|\frac{E_s(\Omega)}{E_{non-scattered}}\right|^2\right)^{1/2} . \tag{4.24}$$

If almost all of the scattered waves are received by the antenna, the density fluctuation level can be estimated considering the square root of the integrated complex auto-power spectrum density of the all frequency above the white noise level as a denominator of $E_s(\Omega)/E_{non-scattered}$ in Eq.4.24, and the square root of the integrated complex auto-power spectrum density in the noticed range of frequency as a numerator.

4.3 Characteristic of Spectrum when Plasma Moves

We have measured the to-and-fro motion of the plasma by using a low pass filter.

At first, the complex auto-power spectrum is shown in Fig. 4.12(a) as the image plot for the case where all the to-and-fro motion can be detected. Here, brightness is used as an indicator of the power and is decreasing from white to black as the power is decreasing. Thus the white path shows the trajectory of the highest peak. There is the Doppler shift which corresponds to the movement of the plasma. The peak frequency of the received wave is shifted in frequency by a frequency of +0.5 kHz, corresponding to the movement of the plasma by 4 mm in a milli-second toward the antenna and -0.5 kHz corresponding to the movement of the plasma back the original position. It is reasonable that the movement of the plasma is detected by using the low pass filtering whose cut-off frequency is 1 kHz.

Our system will detect the Doppler shift if there exists a "macroscopic" misalignment of the antenna. However, such a kind of the Doppler shift is not observed though this data also show the runaway phase phenomena, so that there is not the "macroscopic" misalignment in our case.

The spectrum does not show the shift of the peak frequency and the other low frequency components are relatively high as shown in the period from 709 to 725 ms of Fig. 4.13(a) in the case where the to-and-fro motion cannot be detected. The coherent components have been buried by the incoherent components in this case.

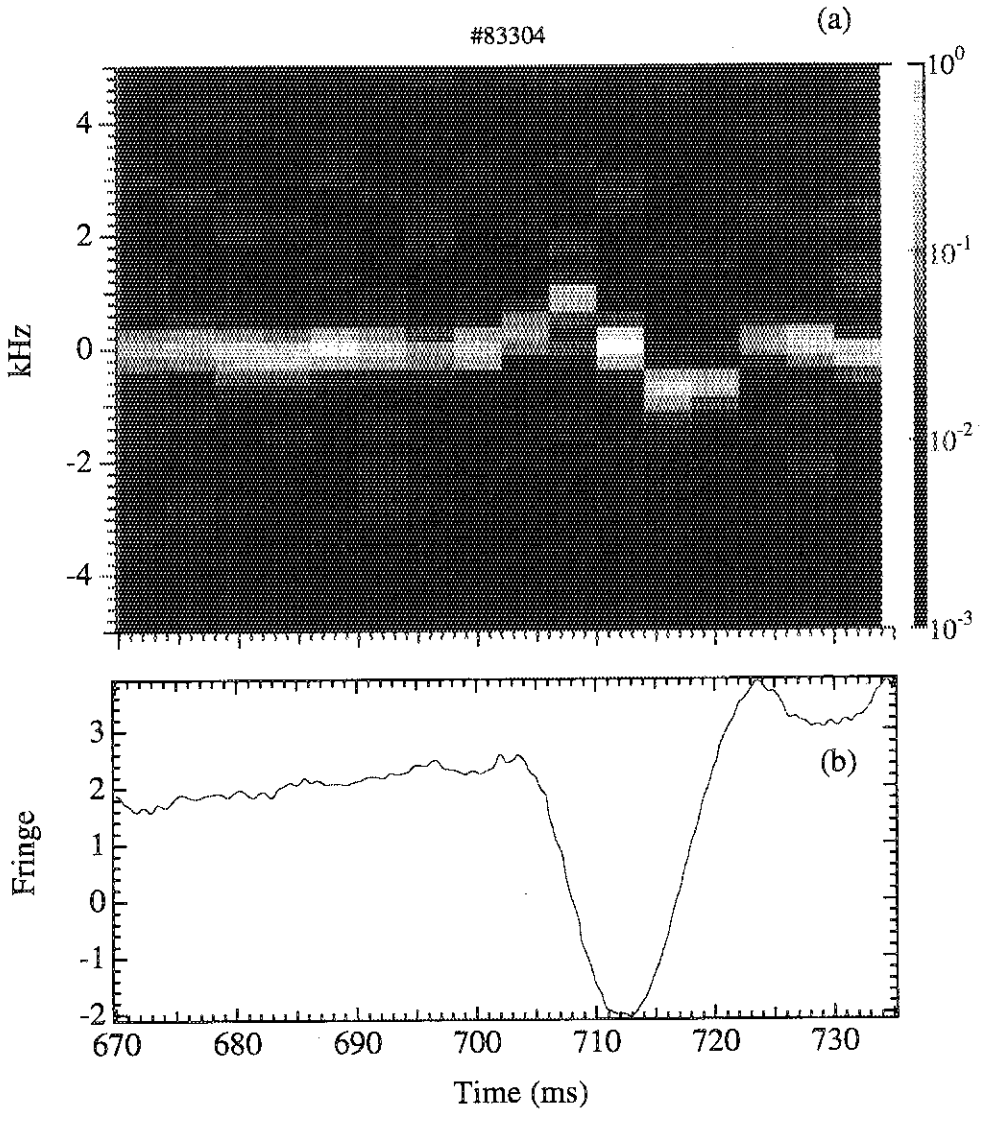

Figure 4.12: (a) is the image plot of the complex auto-power spectrum in the case where all the to-and-fro motion can be detected. The power is log-scaled. Power is indicated by the brightness, white being the maximum and black the minimum. The right label shows the exponent when the base is 10. (b) is the change of phase obtained by using the data filtered by a low pass filter whose cut-off is 1 kHz. The change of phase corresponding to the movement of the plasma is detected during 700 to 720 ms.

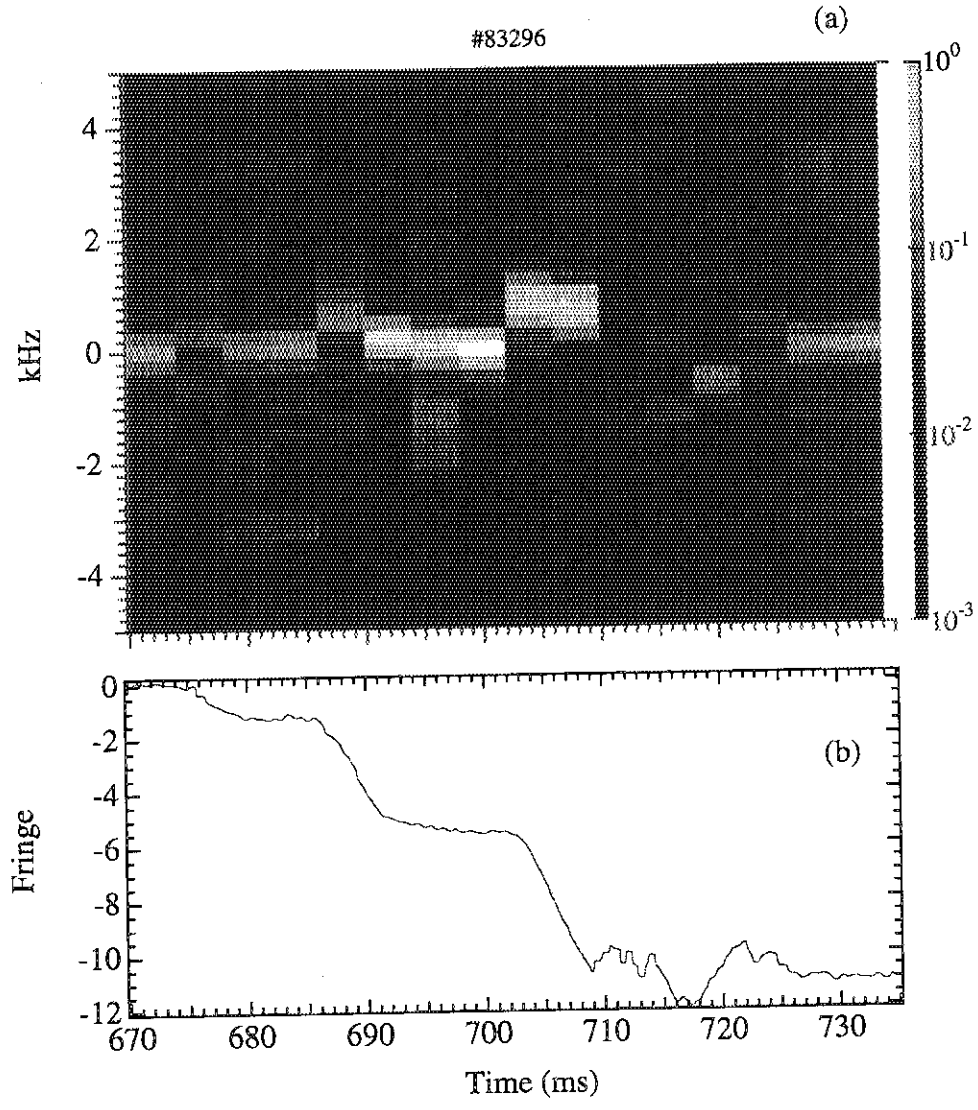

Figure 4.13: (a) is the image plot of the complex auto-power spectrum in the case where the to-and-fro motion cannot be detected. (b) is the change of phase obtained by using the data filtered by a low pass filter whose cut-off is 1 kHz. The change of phase corresponding to the movement of the plasma is partially detected during 700 to 709 ms. The change during 675 to 695 ms is caused by the change of the density profile at L to H transition.

5. Density Fluctuation in L-mode and H-mode

The transport is improved at the L to H transition. It is considered that the microturbulence dominates the transport of the fusion plasma, so that the H-mode would relate to the suppression of the microturbulence. The suppression of the microturbulence by the velocity shear is considered as a mechanism of the H-mode plasma [23]. It is considered that the sheared flow originates in the shear of the electric field.

Density fluctuations in L-mode and H-mode have been observed by reflectometer on JFT-2M tokamak. At first, the density fluctuation is estimated by the conventional method based on geometrical optics. In order to avoid the runaway phase effect, we have used the data in the non-runaway phase period. Next we apply the method proposed in Chapter 4 to the data. This method can be applied not only to the data in non-runaway phase periods but also to the data including the runaway phase. The results obtained by this new method are consistent with those obtained by using the data in the non-runaway phase periods.

5.1 Radial Profile of the Density Fluctuation

The probe can measure the density fluctuation with high time and spatial resolution in the edge region of less than about 1 cm inside the separatrix. The reflectometer, on the other hand, can measure the density fluctuation in the interior region of plasma and does not contaminate the plasma. The consistent data obtained by using these two different methods can give more reliable radial profile of the density fluctuation.

The density fluctuation profiles were measured in the edge, $r/a \gtrsim 0.9$, by Langmuir probes [142]. The probes were fixed at 3 cm outside the separatrix. The plasma was moved to the probe by 4 cm transiently and engulfed the probes. As the result, the probes are inserted 1 cm inside the separatrix. The probes and the antenna of the 1 channel reflectometer system are separated by 10 cm both in the toroidal direction and vertical direction as shown in Fig. 2.2. The density fluctuations were measured by the reflectometer in the same discharge. The density profile measured by the TV Thomson scattering [143] is used in order to decide the value of L_n required in Eq.1.13 and the position of the cut-off layer,r.

The fluctuation levels measured by the reflectometer and the Langmuir probes are similar at the same radial position in the H-mode case, shown in Fig. 5.1. The fluctuation level measured by the reflectometer is nearly same as the extrapolated value at $r/a \sim 0.8$

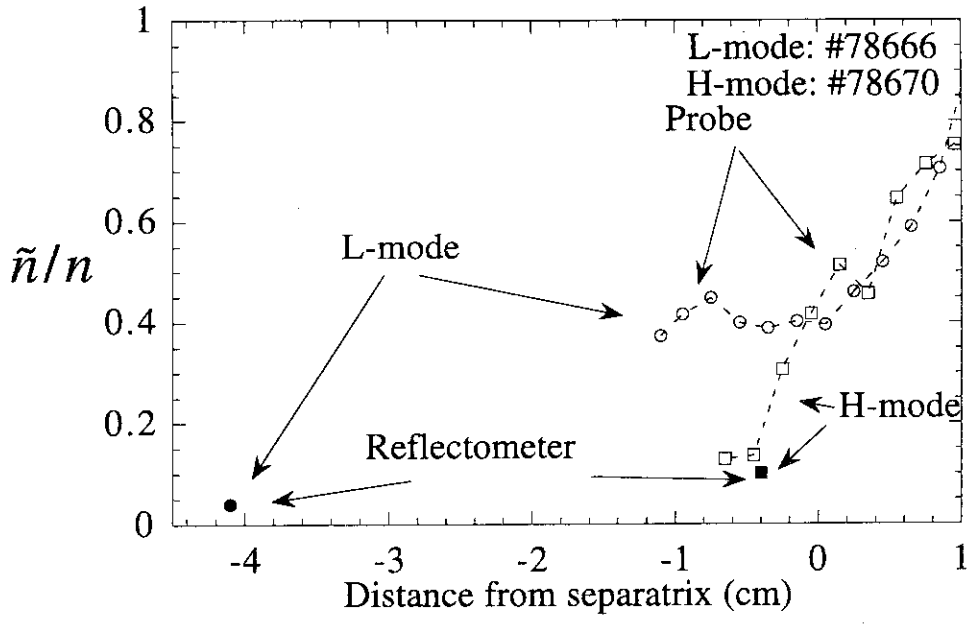

Figure 5.1: The fluctuation levels measured by the reflectometer and Langmuir probes are similar at the same radial position in the H-mode plasma. The fluctuation level measured by the reflectometer is nearly same as the extrapolated value at $r/a \sim 0.8$ of the density fluctuation profile obtained by probes in L-mode.

of the density fluctuation profile obtained by the probes in the L-mode case. The density fluctuation measured by the reflectometer did not change when the probe was inserted into the plasma.

The auto-power spectrum of the density fluctuation measured by the reflectometer have been also compared with that measured by the probes in Fig. 5.2. The comparison has been performed in the same discharge at the same radial position in the H-mode. The peak at 120 kHz can be clearly observed in both figures.

The density fluctuation measured by the reflectometer differs from that measured by probes in terms of the measurable wavenumber. The measurable range of wavenumber in the perpendicular direction to the launched wave of the reflectometer $K_\perp$ is $\lesssim 0.7\text{cm}^{-1}$ because of the geometry of the antenna. The measurable range of wavenumber in the radial direction K_r is $\lesssim 2\pi/\lambda_0 \sim 5\text{cm}^{-1}$. The measurable range of wavenumber with the probe is $K_\perp \lesssim 30\text{cm}^{-1}$ and $K_r \lesssim 15\text{cm}^{-1}$. The agreement of the results derived from the reflectometer and the probes suggests that the wavenumber of the fluctuations is small enough to be detected by both the reflectometer and the probe.

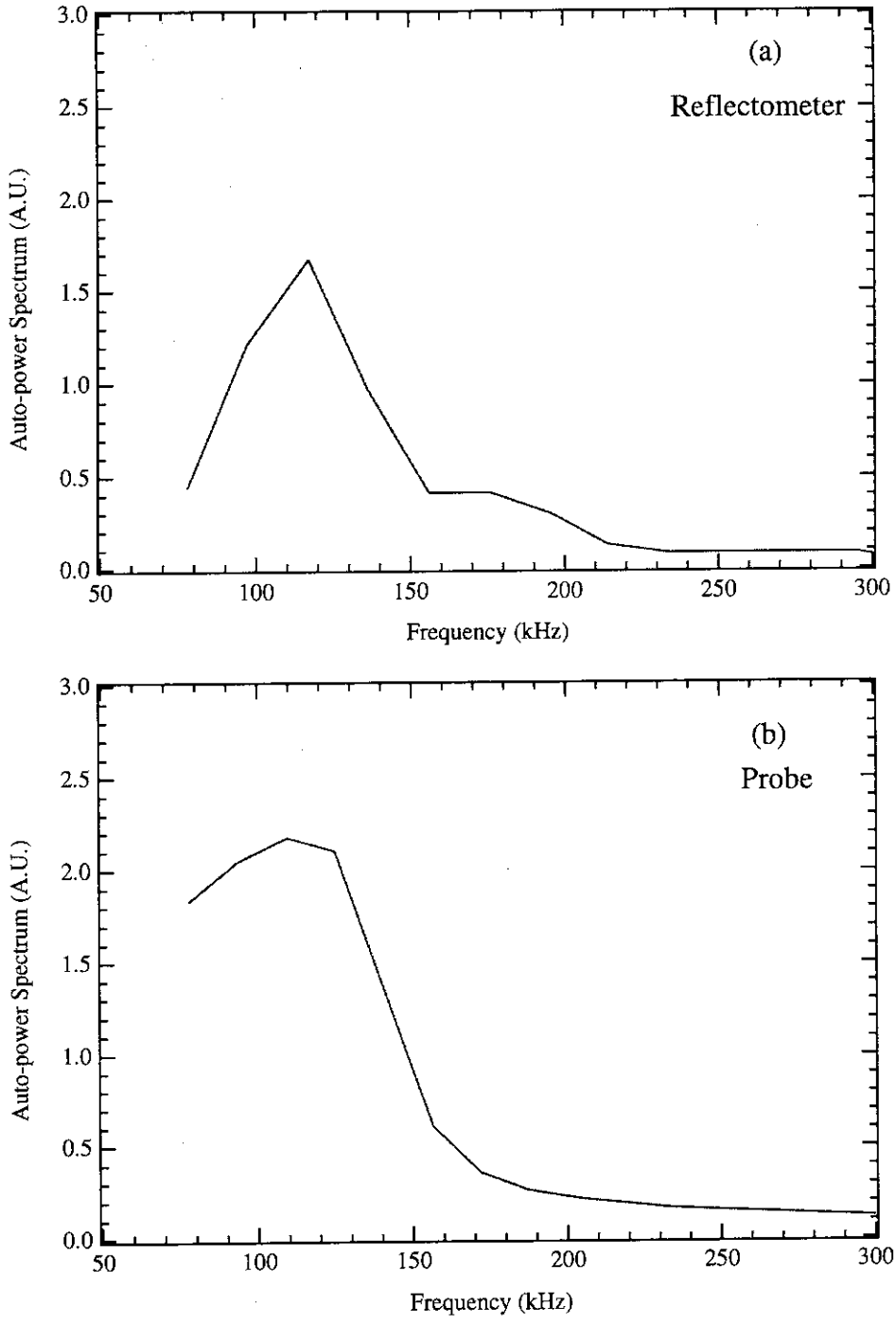

Figure 5.2: (a) and (b) show the auto-power spectrums of the density fluctuations measured by the reflectometer and the probes, respectively. The similar peak around 120 kHz is seen.

5.2 Time Evolution of Fluctuation Level

We have introduced a new indicator to show the degree of the runaway phase phenomena as below:

$$c(t) = \frac{1}{T_s}\int_{-\infty}^{\infty} Phase(t+\tau)h(\tau)d\tau, \tag{5.1}$$

where

$$h(\tau) = \begin{cases} -1 & (-T_s \leq \tau < 0) \\ 0 & (\tau = 0) \\ 1 & (0 < \tau \leq T_s) \end{cases} \tag{5.2}$$

We have automatically rejected the periods during which the runaway phase occurs because these periods can be deduced from this indicator data. The details of this indicator is given in Appendix E.

The analysis of this section is based on this method.

5.2.1 Result of the 50 GHz Reflectometer System

We show the result of the 50 GHz, 1 channel, heterodyne reflectometer system. The cut-off density of the probe wave is $3.1 \times 10^{19}\mathrm{m}^{-3}$.

Figure 5.3(a) shows the time evolution of the phase. Figure 5.3(b) shows the time evolution of $c(t)$ defined by Eq. 5.1. The value of $c(t)$ becomes large when the runaway phase occurs. The non-runaway phase periods are deduced from $c(t)$. We collect samples at the time when $|c(t)|$ is less than 5.8 radian and obtain the non-runaway phase data. The durations of the periods are all different. Figure 5.3(c) shows the time evolution of the fluctuation of the phase using the phase data during the non-runaway phase period. There are certain periods over which the time evolution of the fluctuation remains constant but the durations of such periods differ from one to the next. This is because the fluctuations are time-averaged over each non-runaway phase period. We do not split the data which is relatively large because the result obtained from all the data is more accurate than that obtained from the split small data. The runaway phase occurs frequently when the fluctuations of the phase are relatively large. Figure 5.3(d) shows the time evolution of the intensity of the signal of H_α line. The L to H transition has occurred at about 750 ms and the H to L transition has occurred at about 815 ms. We can see two ELMs around 800 ms. The fluctuations of the phase increase in about 5 ms after the H to L transition and the ELM has occurred. However the fluctuations of the phase gradually decrease after L to H transition has occurred. It takes about $15 \sim 20$ ms. The reproducibility of this feature is good. (The check of the reproducibility for many shots has been realistic owing to the above mentioned automatic runaway phase rejecting method.)

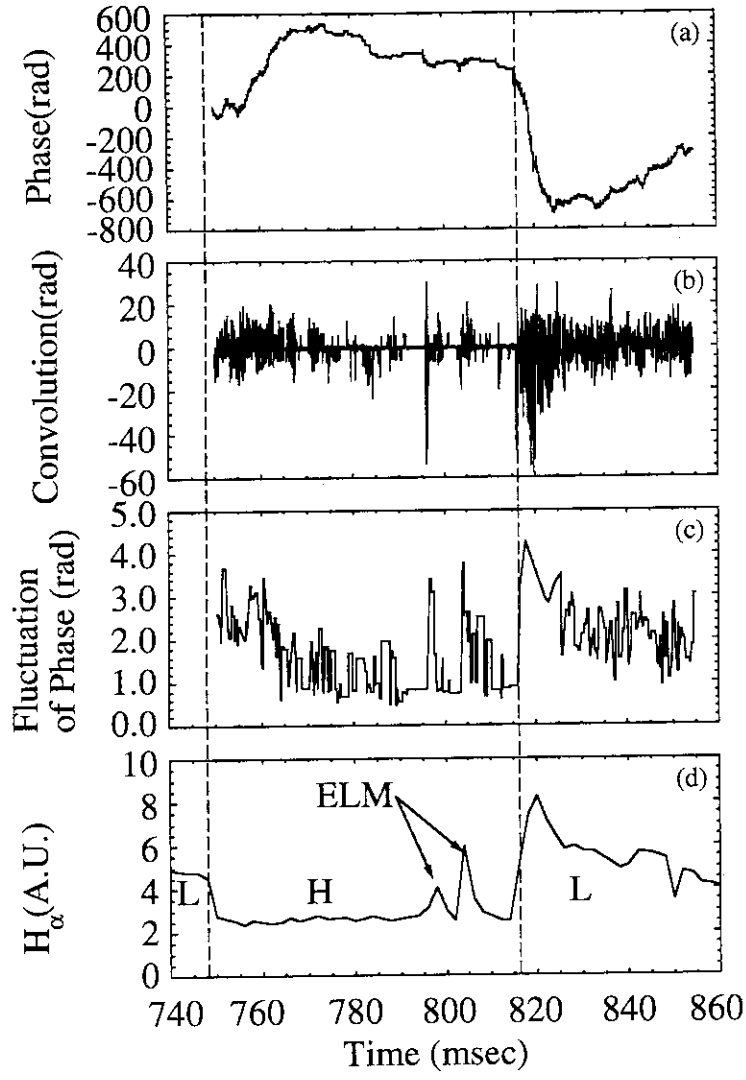

Figure 5.3: (a) shows the time evolution of the phase measured by the reflectometer. (b) shows the time evolution of $c(t)$ defined by Eq. 5.1. The value of $c(t)$ become large when the runaway phase occurs. (c) shows the time evolution of the fluctuation of the phase. (d) shows the time evolution of the intensity of the signal of H_α line. The L to H transition has occurred at about 750 ms and the H to L transition has occurred at about 815 ms. We can see two ELMs around 800 ms. The discharge gas is D_2, $B_T = 1.3$ T, $I_p = 190$ kA, NB which consists of D_2 is injected from 700 ms to 850 ms and the injected power is 650 kW. The configuration is the upper single null.

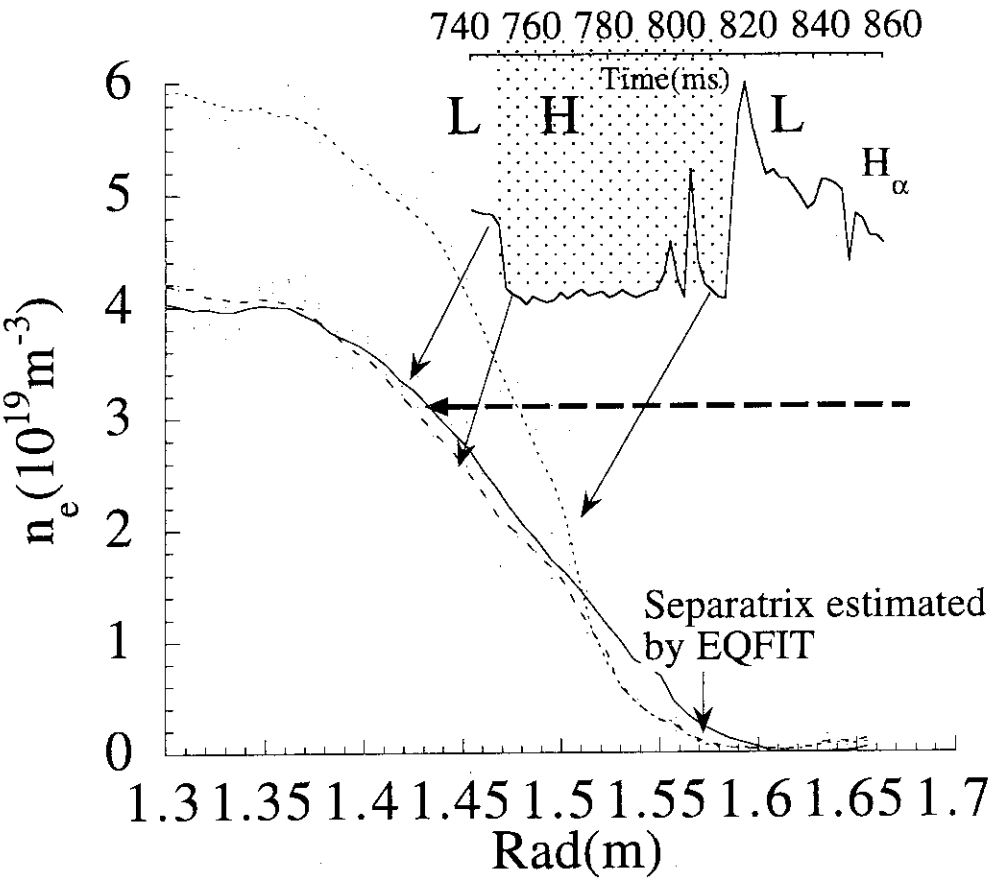

Figure 5.4: The time evolution of the density profile measured by TV Thomson scattering system shot by shot. The profile does not change in the core region just before and after the L to H transition. The reflectometer observes the density fluctuation at the cut-off layer whose density is 3.1×10^{19} m^{-3}, and thus observes almost the same position radially just at transition.

The reflectometer data appear to be inconsistent with the Langmuir probe data. The probe measurements at the edge region show that the density fluctuations are reduced in tens of μs after L to H transition.

The cut-off density of the reflectometer is $n_e = 3.1 \times 10^{19}$ m^{-3}. This layer is usually located around $r/a \sim 0.5$ as shown in Fig. 5.4 at the time when L to H transition occurs. It is inferred that the fluctuations of the phase do not change just after L to H transition because the mechanism of the L to H transition does not contribute to the suppression of the density fluctuations in this region. This may indicate that L to H transition is localized at the edge region. Multichannel system and incident waves with lower frequency are needed in order to know the spatial dependence of the reduction of the fluctuation. This experiment has been performed by the 2 channel reflectometer system. The results is described below.

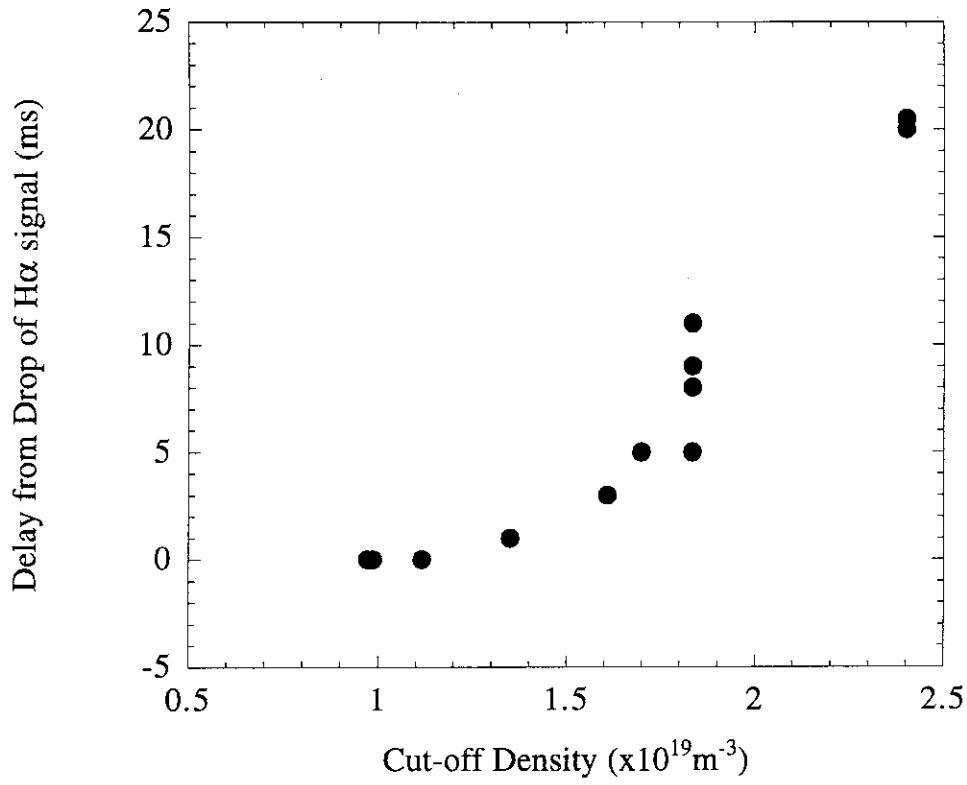

Figure 5.5: Delay of the reduction of the density fluctuation from L to H transition. The reduction of the fluctuation at the higher cut-off density than $1.5 \times 10^{19}\mathrm{m}^{-3}$ is delayed compared with the reduction of the H_α signal. The injected power of NB is about 750 kW. The H-mode begins about 30 ms after NB is injected. The configuration of the plasma is lower single null divertor configuration. B_T is 1.15 T and I_p is 180 kA. The discharge gas is D_2.

5.2.2 Delay of Reduction of Density Fluctuation

The frequency of the incident wave is changeable in 2 channel heterodyne system. We have investigated the delay of the reduction of the density fluctuation.

The frequency of the incident wave was changed from 28 to 44 GHz. The time when the fluctuation is reduced depends on the frequency of the incident wave, namely the cut-off density. The reduction of the fluctuation at the higher cut-off density than $1.5 \times 10^{19}\mathrm{m}^{-3}$ is delayed compared with the reduction of the H_α signal as shown in Fig. 5.5. The relative delay between the two channels can be measured. The delay between the channel whose frequency is set at 28 GHz and the other whose frequency is swept was also investigated and the results were same; the reduction of the fluctuation at the higher cut-off density than $1.5 \times 10^{19}\mathrm{m}^{-3}$ is delayed compared with the reduction of the fluctuation at the cut-off density $0.97 \times 10^{19}\mathrm{m}^{-3}$ which corresponds to the probe frequency of 28 GHz.

In the inner region, this result is consistent with the result of the 50 GHz reflectometer which shows the delay. In the edge region, this result is consistent with the result of the

Langmuir probe which shows no delay. These results show that the reduction of the density fluctuation just at L to H transition occurs only in the edge region.

5.3 Time Evolution of Complex Spectrum

It is difficult to measure the time evolution of the spectrum of the fluctuation from the phase difference since each duration of the non-runaway phase period differs and the time when the non-runaway phase period occurs is not periodic. Furthermore the duration of the non-runaway phase period is too short, typically 100 μs, to obtain enough frequency resolution.

Analysis using the rotary spectrum and the complex spectrum is proposed in Chapter 4. Here we use the complex spectrum (see Appendix D). The complex amplitude $E_R(t)$ of the reflected wave $E_R(t)e^{i\omega_0 t}$ is obtained in our case as below:

$$\begin{aligned} E_R(t) &= (\text{ cosine output of phase sensitive detector }) \\ &+ i(\text{ sine output of phase sensitive detector }), \end{aligned} \tag{5.3}$$

where ω_0 is the frequency of the incident wave.

Time evolutions of complex auto-power spectrum are shown in Fig. 5.6 – 5.8. The cut-off densities in Fig. 5.6 – 5.8(a) are $1.43\times10^{19}\mathrm{m}^{-3}$, $1.70\times10^{19}\mathrm{m}^{-3}$ and $1.83\times10^{19}\mathrm{m}^{-3}$, respectively. All of the cut-off densities in Fig. 5.6 – 5.8(b) is $0.97\times10^{19}\mathrm{m}^{-3}$. These auto-power spectrums are drawn in the range of frequency from -400 kHz to 400 kHz in order to observe the low frequency feature.

The power is log-scaled. The amplitude becomes large as the color becomes black, dark purple, red, orange, yellow, white and blue like the color of a fixed star.

Two interesting features can be observed. One is the delay of the reduction of the main fluctuations with the low frequency, $f \lesssim 100$ kHz. The other is the coherent mode which appears from about 10 ms after L to H transition. These features are discussed later.

5.3.1 Reduction of Edge Turbulence

The density fluctuations are reduced in the low frequency range, $f \lesssim 100$kHz, in the case of cut-off density lower than $1.5\times10^{19}\mathrm{m}^{-3}$ at the time when the signal of H_α drops as shown in Fig. 5.6, while the reduction of the density fluctuations with low frequency is delayed in the case of cut-off density higher than $1.5\times10^{19}\mathrm{m}^{-3}$ as shown in Fig. 5.8.

The detected signals ($\propto \cos\varphi(t)$) have been low-pass-filtered with 90 kHz cut-off frequency based on the results that the reduction of fluctuation levels at L to H transition mainly comes from fluctuations with low frequency. These filtered signals are shown in

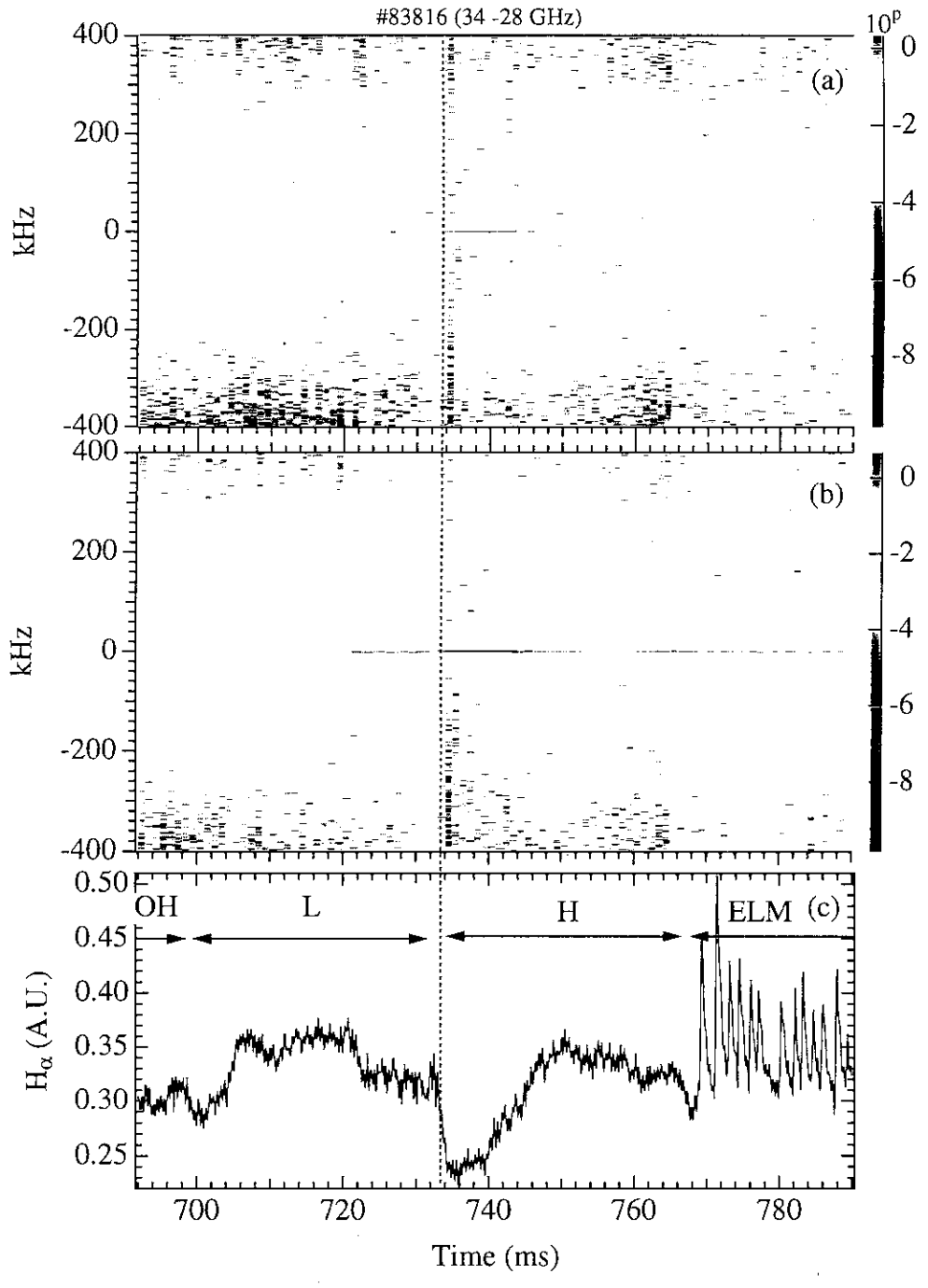

Figure 5.6: Time evolution of the complex auto-power spectrum. (a) shows the spectrum of the reflected wave from the cut-off layer of $1.43 \times 10^{19}\mathrm{m}^{-3}$. (b) shows the spectrum of the reflected wave from the cut-off layer of $0.97 \times 10^{19}\mathrm{m}^{-3}$. The power is log-scaled. The amplitude becomes large as the color becomes black, dark purple, red, orange, yellow, white and blue like the color of a fixed star. The right label shows the exponent when the base is 10. (c) shows the signal of H_α.

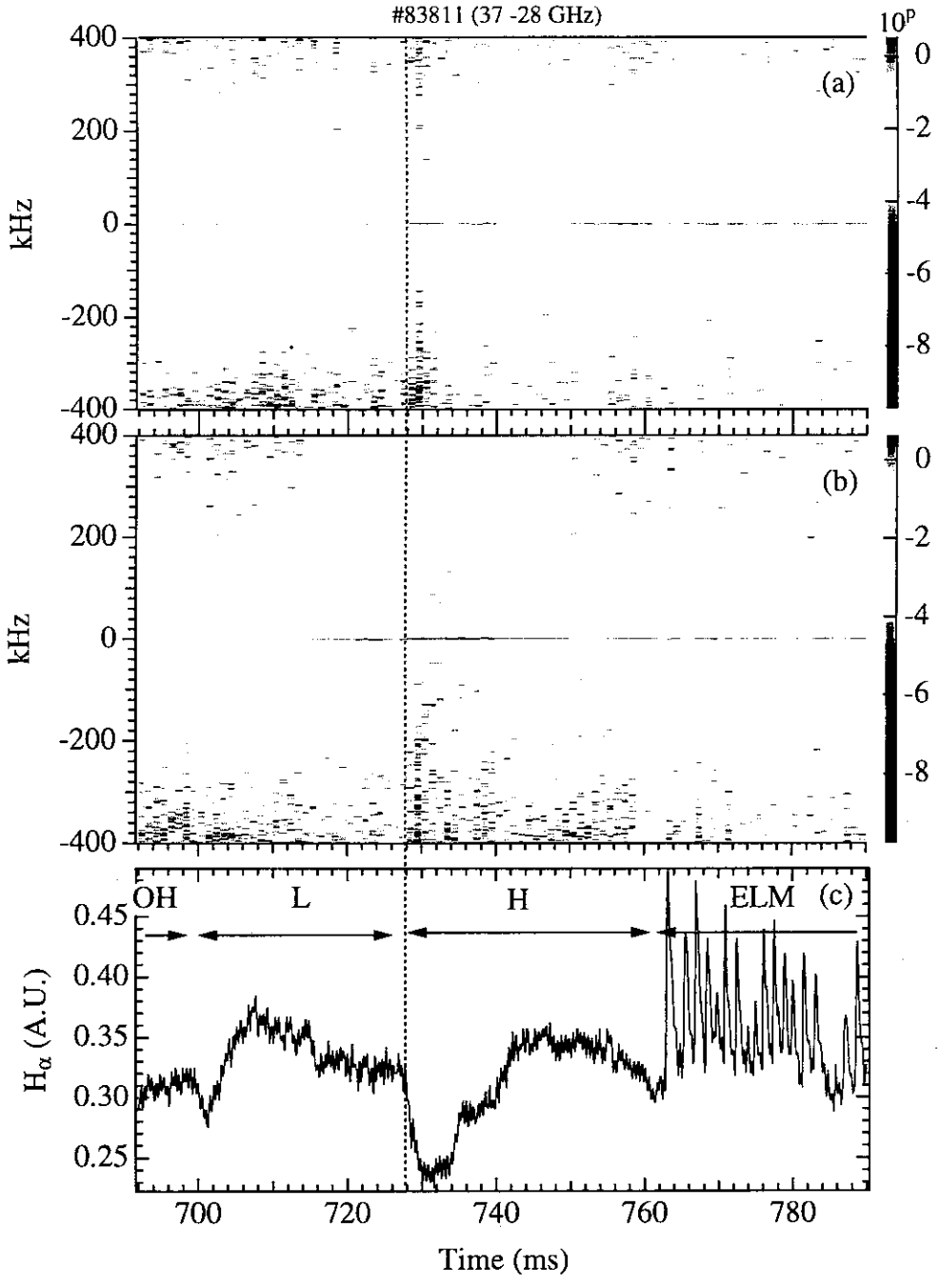

Figure 5.7: Time evolution of the complex auto-power spectrum. (a) shows the spectrum of the reflected wave from the cut-off layer of $1.70 \times 10^{19}\mathrm{m}^{-3}$. (b) shows the spectrum of the reflected wave from the cut-off layer of $0.97 \times 10^{19}\mathrm{m}^{-3}$. (c) shows the signal of H_α.

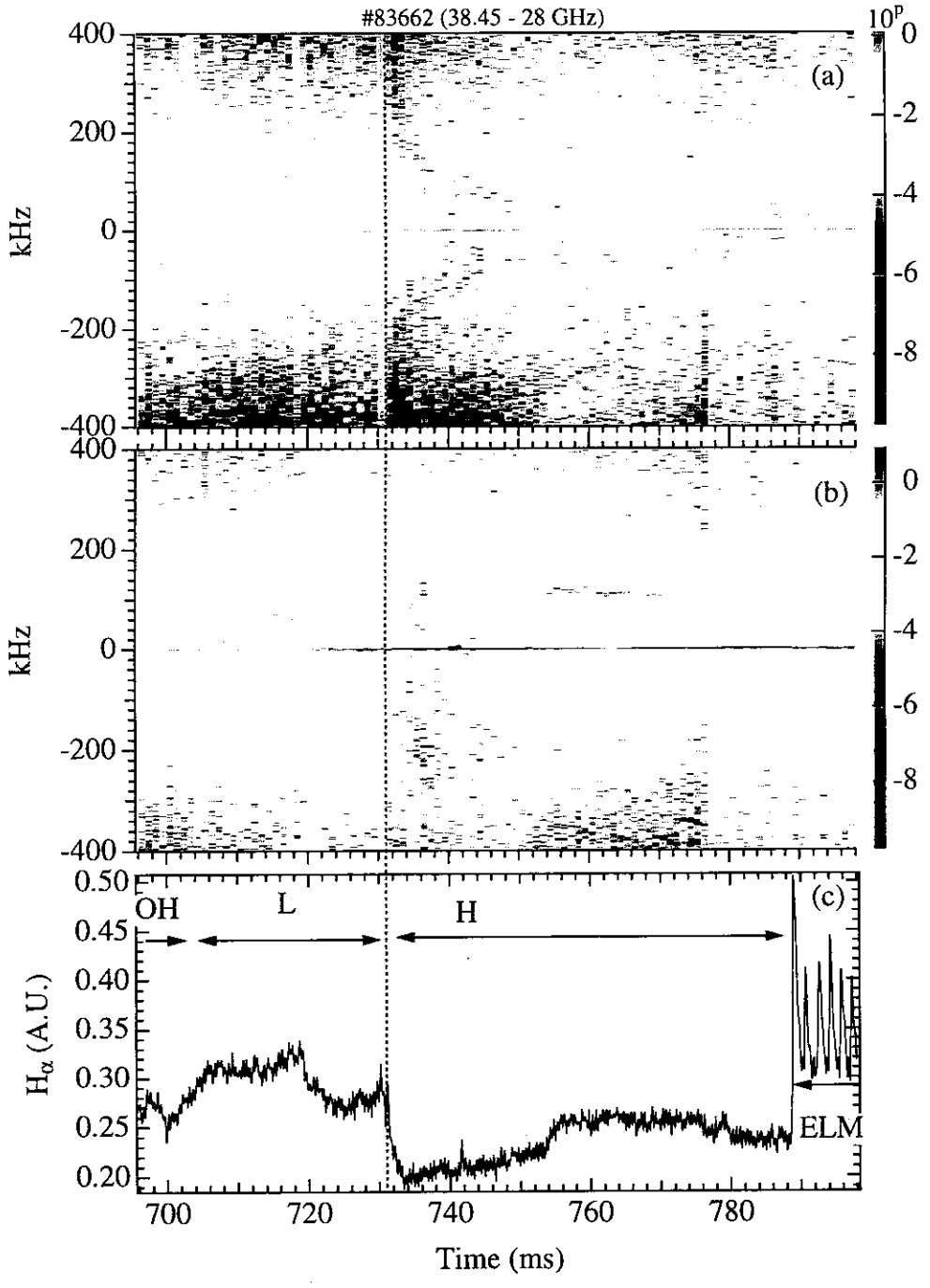

Figure 5.8: Time evolution of the complex auto-power spectrum. (a) shows the spectrum of the reflected wave from the cut-off layer of $1.83 \times 10^{19}\mathrm{m}^{-3}$. (b) shows the spectrum of the reflected wave from the cut-off layer of $0.97 \times 10^{19}\mathrm{m}^{-3}$. (c) shows the signal of H_α.

Fig. 5.9(a),(b). The movements of the cut-off layers estimated by using the low pass filter (the cut-off frequency is 1 kHz) are shown in Fig. 5.9 (c). The absolute position of the cut-off layer is not obtained by the reflectometer of this type. We determine the absolute position of the cut-off layer by using the typical edge density profile measured by the TV Thomson scattering system at the time when the edge profile has become the steady profile in H-mode. The error of the absolute position is about $\pm$ 5 mm due to the errors of the TV Thomson scattering system and the reproducibility of the discharge. The position of the cut-off layer is shown as the relative position, ds, from the separatrix. The sign of ds is negative inside and positive outside the separatrix. The error of the estimation of the position of the separatrix is about $\pm$ 5 mm.

The width of the line shows the fluctuation levels in Fig. 5.9 (a),(b). The slow change of the Fig. 5.9 (a) with the time scale of $\gtrsim$ 1 ms is caused by the change of the phase coming from the movement of the cut-off layer as observed in Fig. 5.9 (c). The reduction of the fluctuation of the signals occur in the edge. The edge region is less than 3 cm which corresponds to the ion poloidal Larmor radius, $\rho_i = M_i v_i / eB_p$, where M_i is the mass of the ion, v_i is the thermal velocity of the ion and B_p is the poloidal magnetic field. This region coincides with the region where a negative electric field is expected to be produced by the ion orbit loss [144] and also with the region where the shear of the electric field has been observed by using charge-exchange spectroscopy measurement [134] as shown in Fig. 5.10.

This results support the model of the turbulence stabilization by the $E \times B$-induced poloidal flow shear; coupling between poloidal shearing and turbulent radial scattering of fluctuations results in the reduction of the radial correlation length and the quenching of fluctuations [23].

The turbulence could be driven by inhomogeneity such as a density gradient. It seems that the steep gradient of the density profile in the edge region may enhance the turbulence in the H-mode, but the enhancement does not happen in the very edge region of ds$\gtrsim -2$ cm. This is because there is the shear of the radial electric field E_r and the $E \times B$-induced shear flow which prevents the turbulence from growing in this region.

5.3.2 Coherent Mode

The coherent feature (about 100 kHz) is seen about 10 ms after L to H transition. This mode is also detected by a Langmuir probe at the edge as shown in Fig. 5.11. The coherent feature resemble the fluctuation on ASDEX [16] and PBX [24]. A Steep density gradient exists and the cut-off layer exists in this steep density gradient region when this mode occurs. This mode can be caused by the steep density gradient or by a steep pressure gradient.

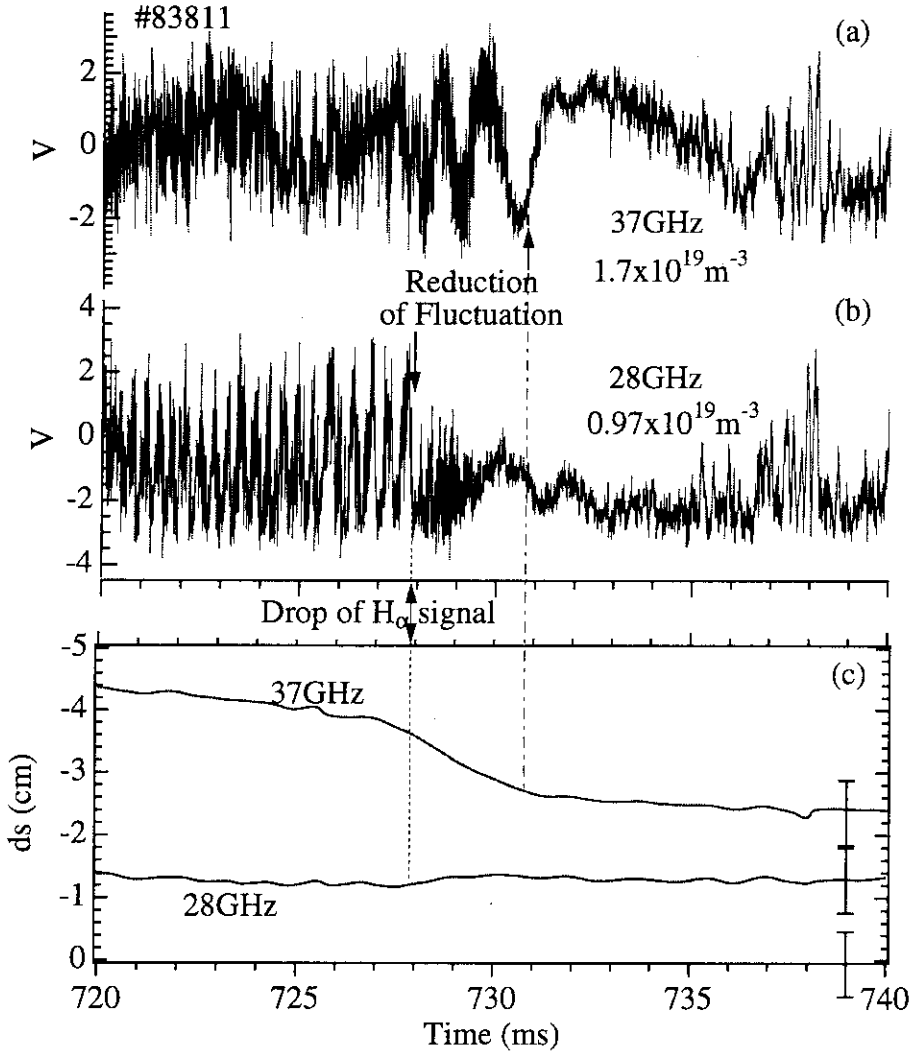

Figure 5.9: Reduction of turbulence. The signals ($\propto \cos\varphi(t)$) which are passed through the low-pass filter with 90 kHz cut-off frequency are shown in (a), (b). The width of the line shows the fluctuation levels. (c) shows the movement of the corresponding cut-off layer. The position of the cut-off layer is shown as the relative position, ds, from the separatrix. The sign of ds is negative inside the separatrix. The error of the position of the cut-off layer is about $\pm$ 5 mm and the error of the position of the separatrix is about $\pm$ 5 mm.

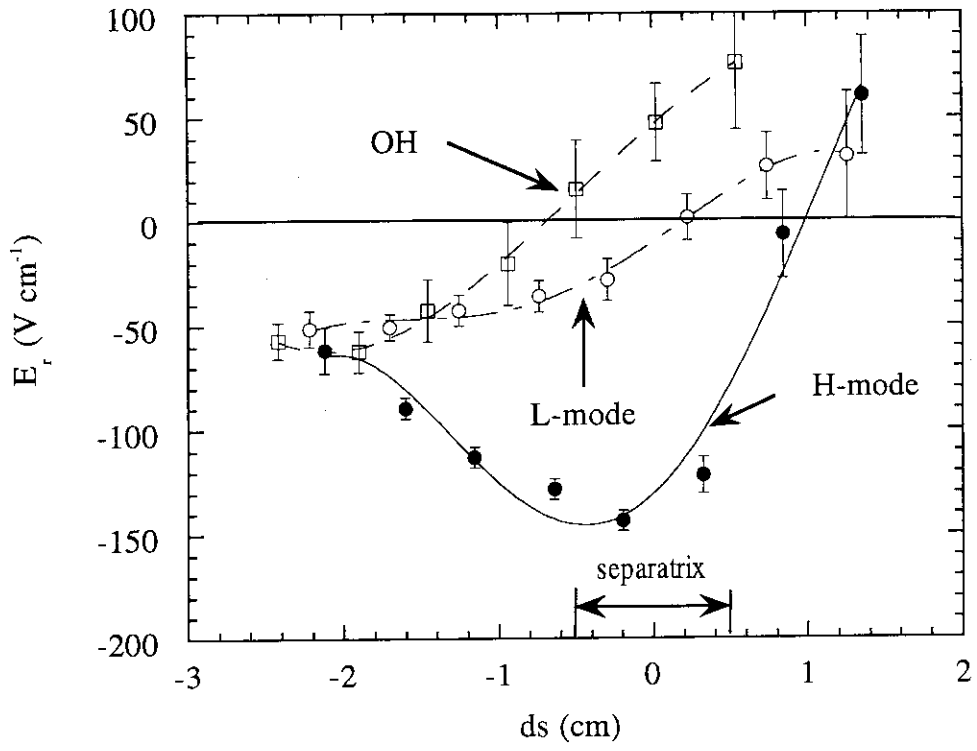

Figure 5.10: Radial profile of edge electric field as a function of the distance from the separatrix, for OH (open square), L-mode (open circle) and H-mode (closed circle) plasmas. The sign of ds is negative inside and positive outside the separatrix. (quoted from Ref. [145])

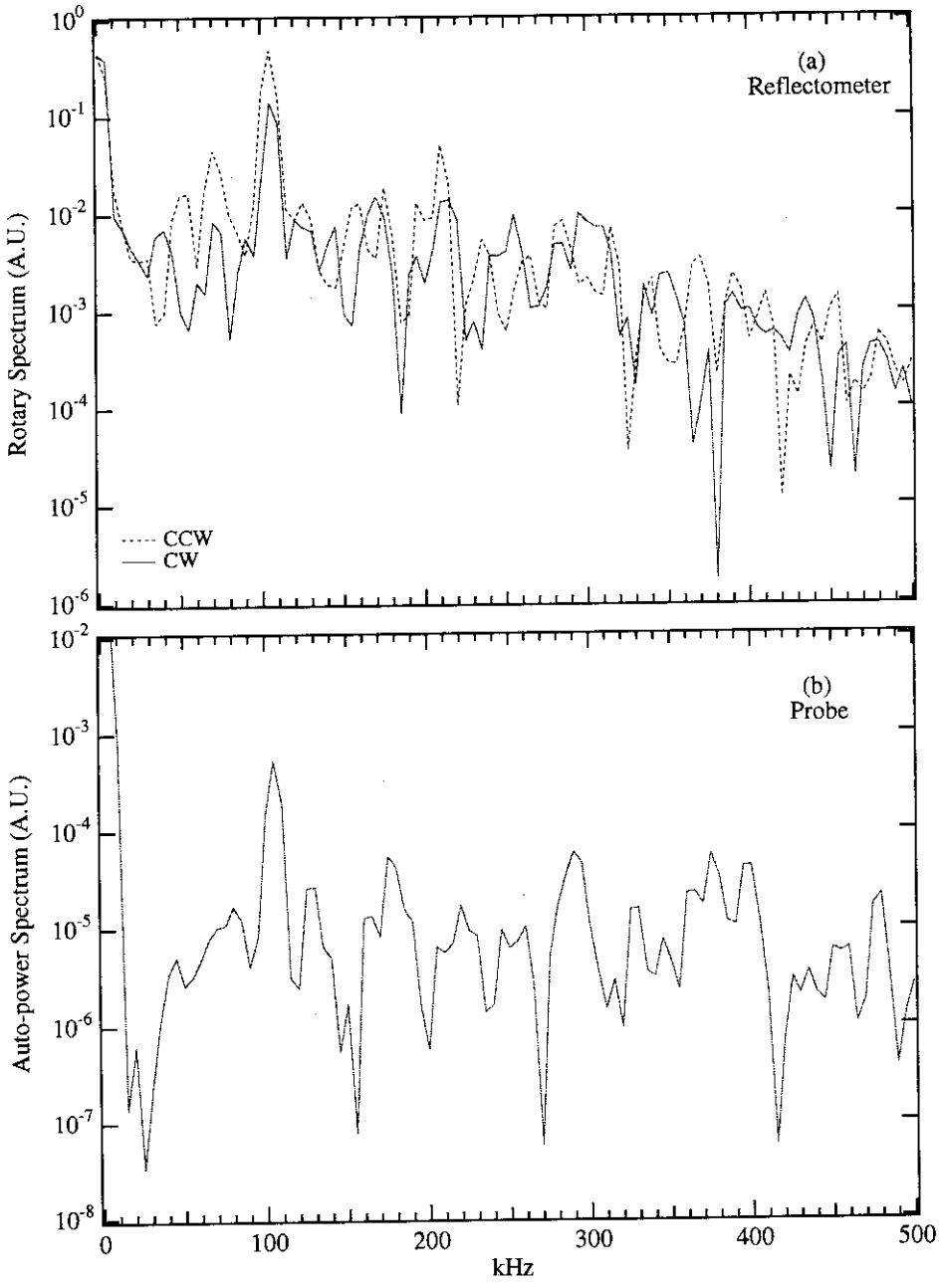

Figure 5.11: The coherent mode whose frequency is about 100 kHz is observed in H-mode from about 10 ms after L to H transition. (a) is the spectrum of the data measured by the reflectometer whose probe frequency is 38 GHz and corresponds to the cut-off density of $1.79 \times 10^{19}\mathrm{m}^{-3}$. The position of the cut-off layer is about 2 cm inside the separatrix. (b) is the spectrum of the data measured by the Langmuir probe. The measured position is about 1 cm inside the separatrix.

The frequency of the mode is about 80 kHz just before the H_α signal increase as shown in Fig. 5.12. The frequency drop at H-L transition may mean the decrease of the poloidal rotation if this mode is almost standing on the system which moves with the plasma. It can be helpful to know the role of the poloidal rotation in H-mode.

This is the expected range for drift wave type instabilities. Assuming the peak at 100 kHz comes from a drift wave, the wavelength of the drift wave can be estimated as $\sim$ 80 mm ($K \sim 0.75\mathrm{cm}^{-1}$) using the values $T_e \sim 100\mathrm{eV}, B \sim 1\mathrm{T}$ and $L_n \sim 10\mathrm{mm}$. The wavelength is consistent with the result of the correlation measurement by using a Langmuir probes.

5.4 Correlation Measurement

The measurement of the radial correlation length is interesting at L to H transition related to the reduction of the transport and the fluctuation level.

The profile of $D_{e,r}$ is always estimated indirectly by solving the equations,

$$\frac{\partial n_e}{\partial t} = \frac{1}{r}\frac{\partial}{\partial r}(r\Gamma_e) + S_{e,n} + S_{e,NBI}, \tag{5.4}$$

$$D_{e,r} \equiv -\Gamma_e / \nabla n_e, \tag{5.5}$$

where Γ_e is the electron particle flux, $S_{e,n}$ is the electron source coming from the neutral transport and $S_{e,NBI}$ is the electron source coming from the neutral beam injection. The global information is needed. However, the diffusion coefficient can be estimated directly with random walk,

$$D_r = \frac{{l_r}^2}{2\tau_c}, \tag{5.6}$$

with l_r the radial correlation length and τ_c the correlation time. These values are measured locally. The latter method is useful as it is considered that the drastic improvement of the transport at the L to H transition occurs locally at the edge corresponding to the generation of the electric field.

Biglari et al. [23] say that the radial correlation length is reduced by rotational shearing relative to its value as determined by ambient turbulence alone and that the reduction in the radial correlation length results in the quenching of fluctuations. The relation between the reduction of the fluctuations and the reduction of the radial correlation length is a subject to be investigated.

The 2 channel reflectometer can be used as a correlation reflectometer. In correlation reflectometry, two independent reflectometers operating with microwave frequencies f_1, f_2 probe the plasma along the same line of sight and in the same polarization. The reflecting layers are at R_1 and R_2 separated by a distance δx. The reflected waves come back with the information of density fluctuation of the two cut-off layers. The correlation between these two channels is calculated.

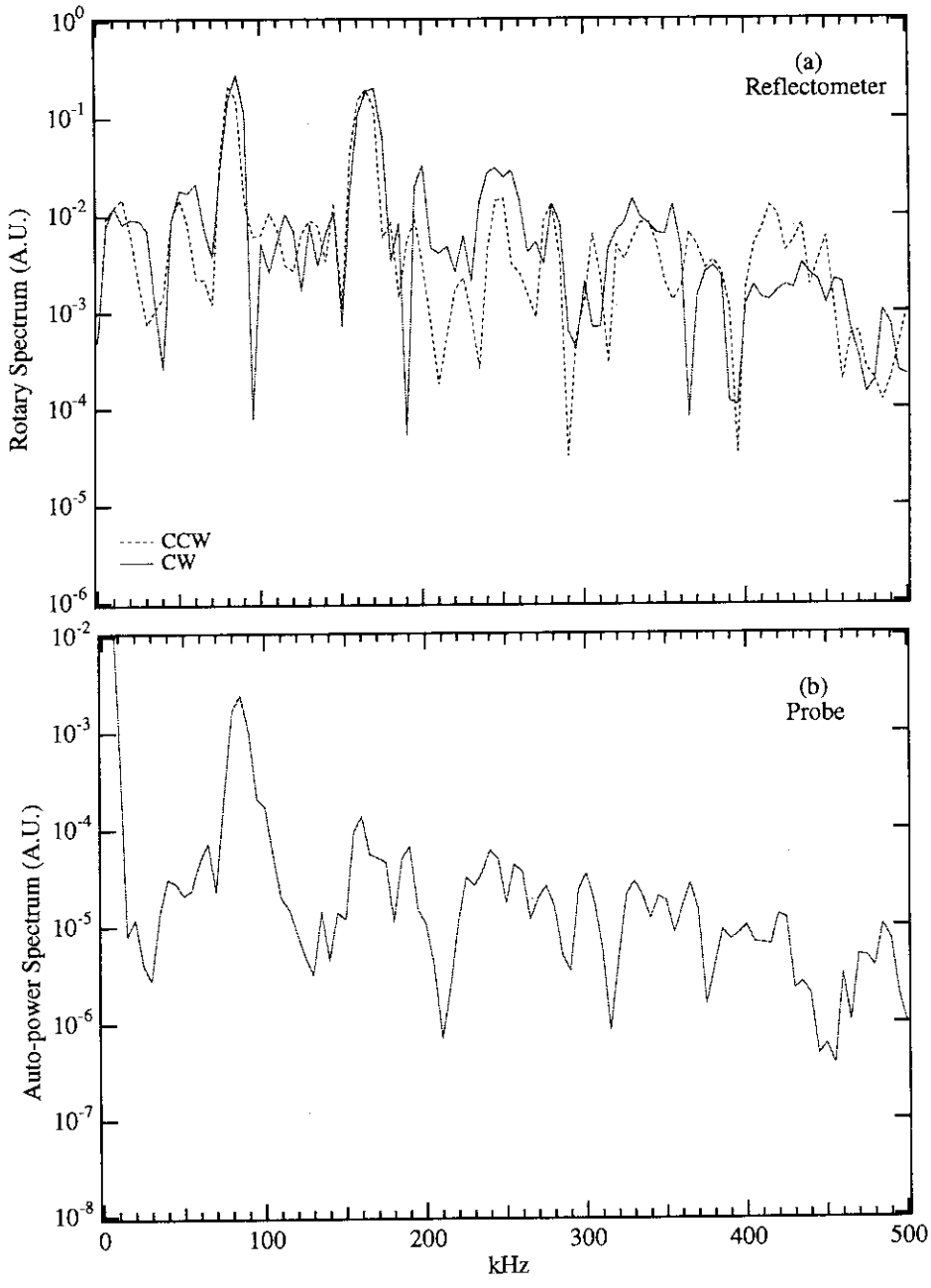

Figure 5.12: The frequency of the coherent mode changes from about 100 kHz to about 80 kHz just before the H_α signal increase. (a) is the spectrum of the data measured by the reflectometer at about 2 cm inside the separatrix. (b) is the spectrum of the data measured by the Langmuir probe at about 1 cm inside the separatrix.

5.4.1 Correlation Length Measurement

The frequency of one reflectometer is set at f_2 corresponding to the position which we want to investigate (Fig. 5.13). The other frequency f_1 is changed shot by shot around the frequency f_2. The correlation is estimated for each cut-off density. The profile of the correlation is determined once density profile is known. The density profile is obtained by TV thomson scattering system. From this profile of the correlation, we can estimate the correlation length, which is usually defined as the e-folding length of the profile of the correlation.

By using the data during the period when the runaway phase does not occur, the profile of the correlation of the measured phase difference is obtained. Figure 5.14(a) corresponds to the case where frequency $f_2 = 38.45$GHz (cut-off density: $1.83 \times 10^{19}\mathrm{m}^{-3}$) and f_1 is varied from 38.3 to 28 GHz. Figure 5.14(b) corresponds to the case where frequency $f_2 = 28$GHz (cut-off density: $0.98 \times 10^{19}\mathrm{m}^{-3}$) and f_1 is varied from 28 to 37 GHz. For the H-mode, the points corresponding to the next 4 ms after L to H transition are plotted. Thus Fig. 5.14(a) shows the profile of the correlation in the region of $r/a \sim 0.8$, about 5 cm inside the separatrix and Fig. 5.14(b) shows the profile of the correlation in the region of $r/a \lesssim 1$, just inside the separatrix. The periods without the runaway phase are short and typically shorter than 100 μs on the points in the Fig. 5.14.

The coherence analysis based on the fast Fourier transfer method (Eq. B.5) has not been used because of the following reason: as it is important to perform enough ensemble average on this method, Eq. B.5 becomes

$$\begin{aligned} \gamma(f) &= \frac{|S_{ab}(f)|}{(S_{aa}(f)S_{bb}(f))^{1/2}} \\ &= \frac{\left|A(f)e^{-i\theta_a(f)}B(f)e^{i\theta_b(f)}\right|}{|A(f)|\,|B(f)|} \\ &= \left|e^{i(\theta_b(f)-\theta_a(f))}\right| = 1, \end{aligned} \tag{5.7}$$

if the ensemble average is not performed. The value of $\theta_b(f) - \theta_a(f)$ in Eq. 5.7 can have a shot dependence because of, for example, a little difference in the position of the cut-off layer. Therefore the ensemble average should be performed by time averaging, not by shot averaging. However in our case, it is difficult to know the characteristic of the coherence because the period when the runaway phase does not occur is short and the frequency resolution is not good.

We used the correlation function,

$$C_{ab}(\tau) \equiv \frac{< a(t+\tau)b(t) >}{\sqrt{< a^2(t) >< b^2(t) >}} \tag{5.8}$$

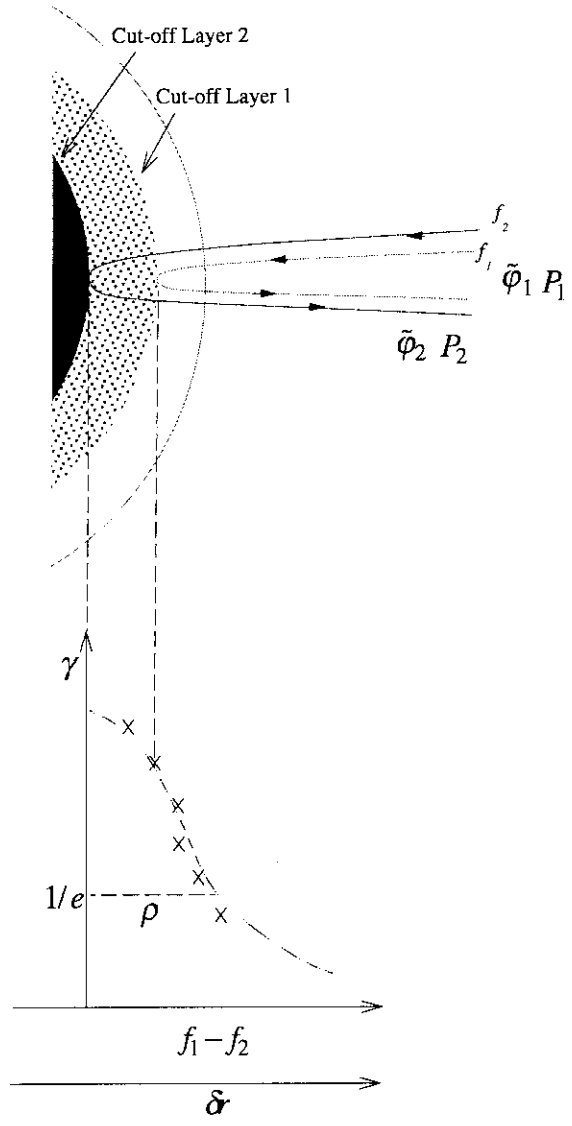

Figure 5.13: Principle of the correlation length measurement. The profile of the correlation can be obtained by changing the frequency f_1 of the one channel with the frequency f_2 of the other channel fixed.

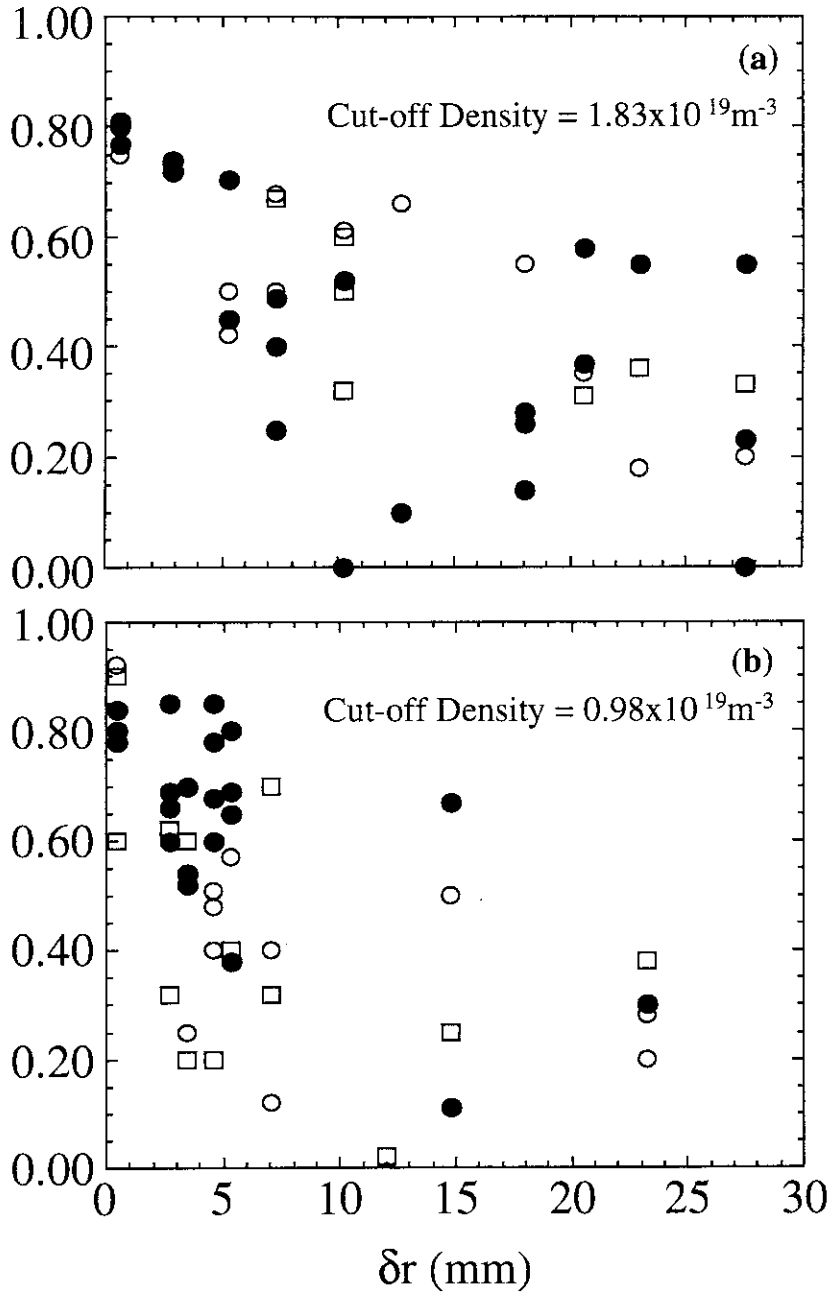

Figure 5.14: (a) is the profile of the correlation in the region of $r/a \sim 0.8$, about 5 cm inside the separatrix. (b) is the profile of the correlation in the region of $r/a \sim 1$, just inside the separatrix. On each graph, open circle , ○, shows the OH phase, open square , □, shows the L-mode phase and filled circle , ●, shows the H-mode phase. For the H-mode, the points corresponding to the next 4 ms after L to H transition are plotted.

$$= \frac{\int_{-T/2}^{T/2} a(t+\tau)b(t)dt}{\sqrt{\int_{-T/2}^{T/2} a^2(t)dt \int_{-T/2}^{T/2} b^2(t)dt}}, \tag{5.9}$$

where T is the duration of the period when the runaway phase does not occur. $C_{ab}(\tau)$ is reliable in the range of the $\tau \ll T$, which is less than 20 μs in our case ($T \lesssim 100\mu$s).

As the scattering is large in Fig. 5.14, it is difficult to differentiate among OH,L-mode and H-mode. The reason why the scattering is large is considered as below:

- Only the phenomena higher than 50 kHz can be observed by the method of Eq. 5.9 in our case, however it is expected that the fluctuations with the frequency lower than 50 kHz is essential.

- The zero level has to be calculated by time averaging over the phase data we actually measured. We can not determine the correct zero level since the large fluctuations with low frequency exist partially.

It seems that the correlation length, $l_r \sim$ 10mm, in the outer region is shorter than that, $l_r \sim$ 15mm, in the inner region though the scattering is large. The diffusivity can be estimated with random walk (Eq. 5.6). The diffusivity is smaller in the outer region than inner region if we assume the correlation time is not changed, because the correlation length in the outer region is shorter than that in the inner region. This result is inconsistent with the well-known results [146,147]. The turbulence with frequency higher than 50 kHz may not contribute to the transport.

5.4.2 Coherence of the Complex Amplitude

The coherence estimated by using the phase difference does not show the difference between L-mode and H-mode. However, the coherence of the complex amplitude is clearly reduced in the range of frequency lower than 80 kHz at the L to H transition and in H-mode as shown in Fig. 5.15(a) when the frequencies of the probe waves are 38 GHz and 39 GHz, respectively. On the other hand, the coherence is not reduced as shown in Fig. 5.16(a) when the frequency of the probe wave is 28 GHz and 29 GHz, respectively.

The coherence around 100 kHz is enhanced in both figures in H-mode though the asymmetry of the spectrum is large in Fig. 5.16. The frequency corresponds to the frequency of the above mentioned coherent mode.

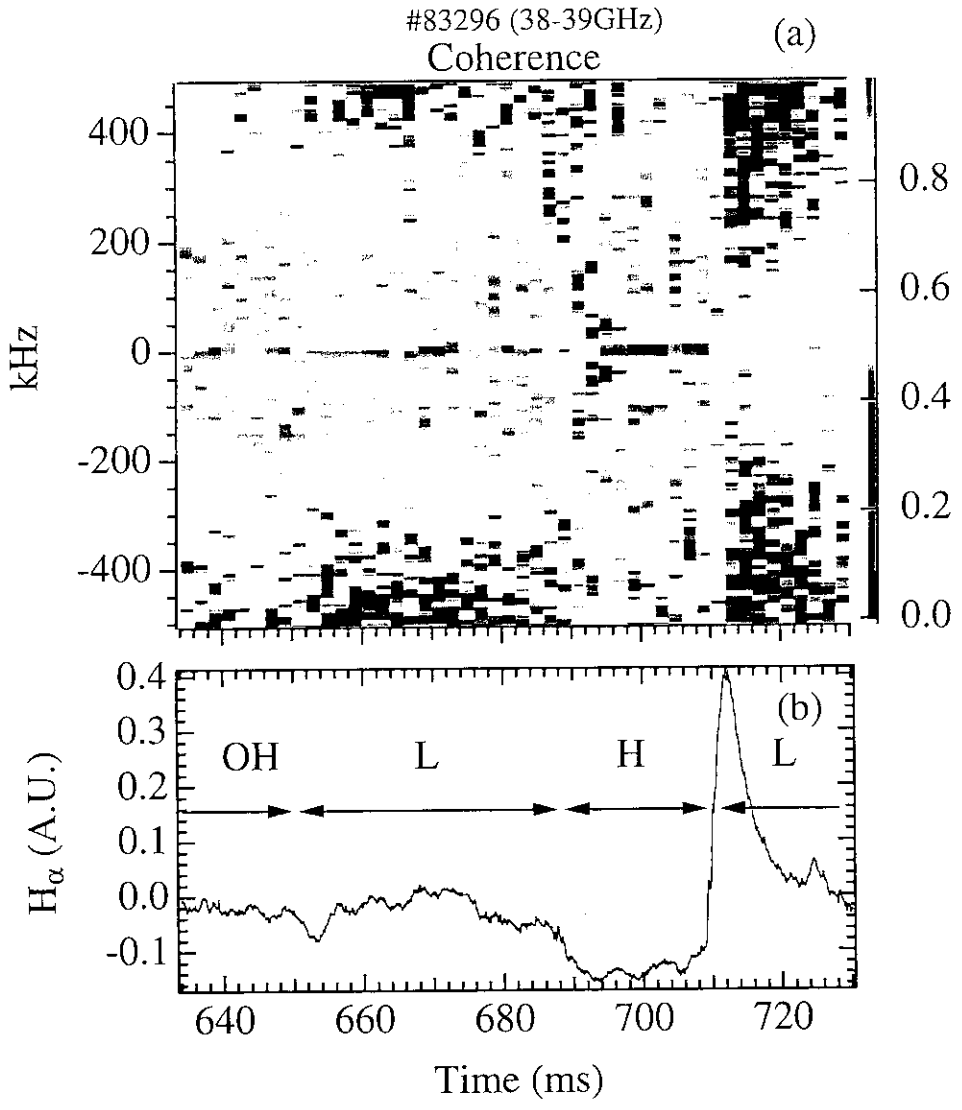

Figure 5.15: Time evolution of the coherence of the complex amplitude. (a) is linear scaled image plot of the coherence between the cut-off layer of $1.79 \times 10^{19}\mathrm{m}^{-3}$ (38 GHz) and that of $1.89 \times 10^{19}\mathrm{m}^{-3}$ (39 GHz). The amplitude changes from 0 to 1 as the color becomes black, dark purple, red, orange, yellow, white and blue. (b) is the signal of H_α.

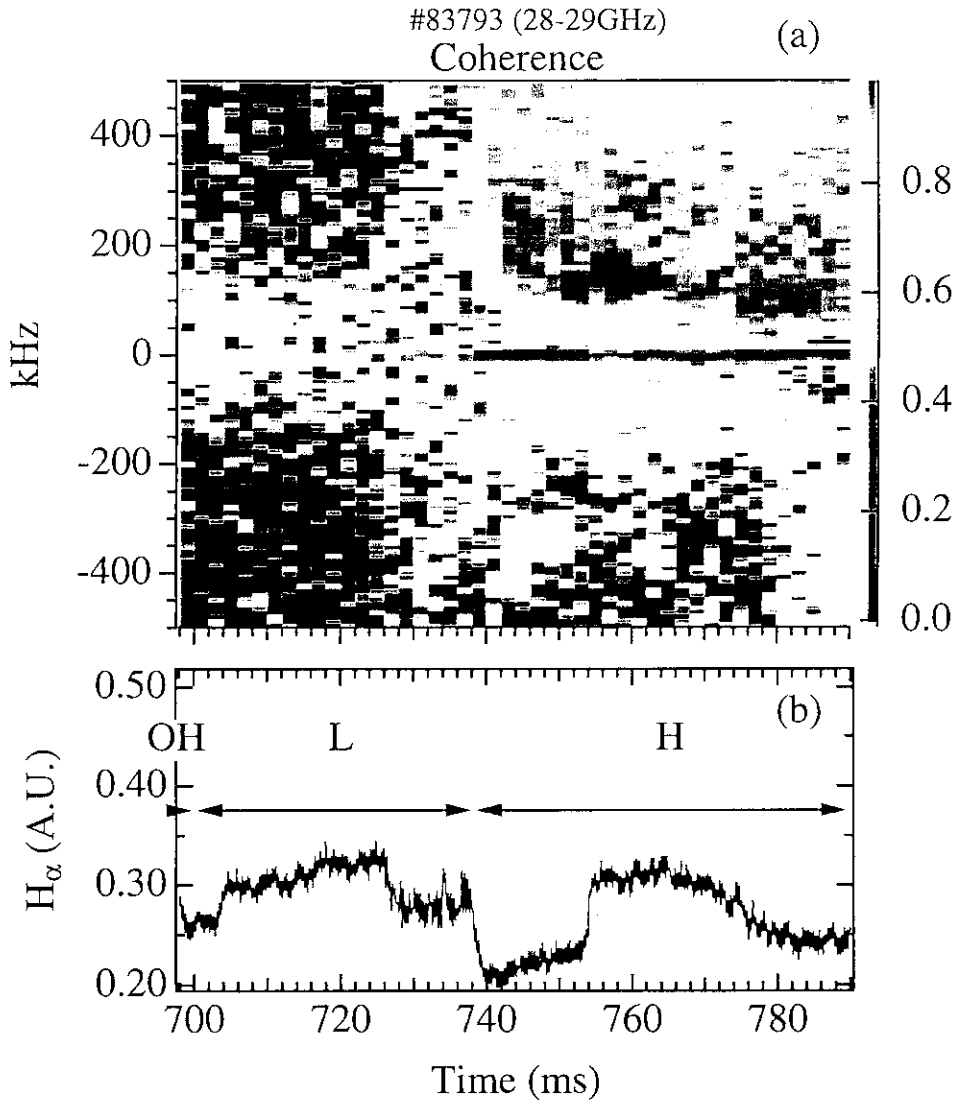

Figure 5.16: Time evolution of the coherence of the complex amplitude. (a) is linear scaled image plot of the coherence between the cut-off layer of $0.97 \times 10^{19}\mathrm{m}^{-3}$ (28 GHz) and that of $1.04 \times 10^{19}\mathrm{m}^{-3}$ (29 GHz). (b) is the signal of H_α.

5.5 Shape of Spectrum

The H-mode is due to the improved transport and the transport is predicted to be mainly due to the turbulence. It is expected that the reduction of the turbulence is strongly related to the L to H transition. Because of this, the most attention has been paid to the reduction of the fluctuation level at the L to H transition.

The dashed line shows the spectrum of the density fluctuation in L-mode, and the solid line shows the spectrum of the density fluctuation just after the H_α drops, namely the L to H transition, in Fig. 5.17. Here the total spectrum of the rotary spectrum is used as the auto-power spectrum (see Appendix C). The components with the frequency higher than about 300 kHz are enhanced while the components with the frequency lower than about 300 kHz, which are the main components of the fluctuations, are clearly reduced. This feature is unchanged even if the coherent mode with the frequency of 100 kHz appears. This characteristic frequency has changed from 300 to 600 kHz shot by shot.

Figure 5.17 shows the case where the cut-off density is $0.97 \times 10^{19}\mathrm{m}^{-3}$. The same feature is observed in the spectrum at other cut-off densities.

The enhancement of the fluctuations with the frequency higher than 300 kHz has never been reported and may give us some information about the mechanism of the transport caused by the turbulence. It is an interesting feature to investigate in future works.

Another interesting feature is the slope of the spectrum. The slopes of the spectrums in the range of frequency of $\gtrsim$ 800 kHz in L-mode, $\gtrsim$ 1 MHz in H-mode and $\lesssim$ 20 kHz in H-mode always resemble each other. In other range of frequency, the slope does not always resemble these slopes. The spectrums it the range of frequency of $\gtrsim$ 800 kHz (L-mode), $\gtrsim$ 1 MHz (H-mode) and $\lesssim$ 20 kHz (H-mode) are fitted with the form

$$S(f) \propto f^{-6\pm2}. \tag{5.10}$$

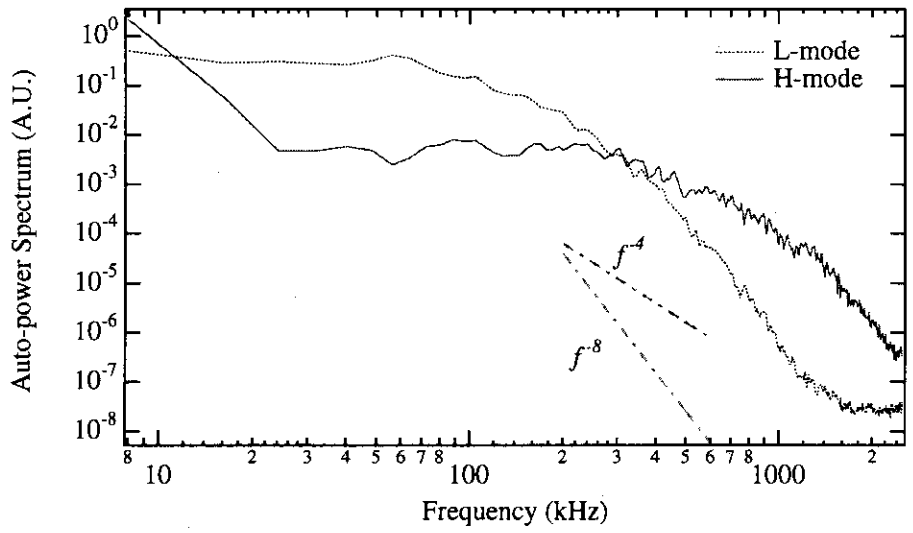

Figure 5.17: Characteristic of the shape of the spectrum. The dashed line shows the spectrum of the density fluctuation in L-mode, and the solid line shows the spectrum of the density fluctuation just after the L to H transition. These spectrums are log-log scaled. The enhancement of the components with the frequency higher than about 300 kHz is observed.

6. Discussions

6.1 Coherent Mode

The coherent mode structure is observed around 100 kHz in H-mode. The mode appears about 10 ms after L to H transition. This timing corresponds to the formation of the steep density and temperature gradient in the edge region.

The coherent mode is detected throughout the range of the operation frequency of our reflectometer system, from 28 GHz to 50 GHz. The range of the corresponding cut-off density is from $0.97 \times 10^{19}\mathrm{m}^{-3}$ to $3.1 \times 10^{19}\mathrm{m}^{-3}$. These cut-off layers lie in the region from just inside the separatrix to 5 cm inside the separatrix. The trajectory of the complex amplitude of the reflected wave draws the arc shape when the mode occurs. The mode is also detected by Langmuir probe at just inside the separatrix. The coherent mode is detected in the very wide region, $0.8 \lesssim r/a \lesssim 1$ where a is the minor radius of the plasma. This wide region corresponds to the region in which the density and temperature profiles have a steep gradient. The global feature is consistent with the fact that the trajectory of the complex amplitude of the reflected wave draws the arc shape when the mode occurs.

The similar mode structure have been detected by the magnetic probe.

From these facts, it is inferred that the coherent mode is the global MHD activity which is caused by the steep profile of the density or the temperature, or both. The mode may be driven in the interior region where there is no E_r shear, so that this mode is not suppressed in H-mode and only the global effect may be detected in the very edge region.

6.2 Coherence

In the model of the turbulence stabilization by the $E \times B$-induced poloidal flow shear, the radial correlation length is "reduced" by rotational shearing relative to its value as determined by ambient turbulence alone and the reduction in the radial correlation length results in the quenching of fluctuations and a reduction in the transport level [23].

The reduction of the coherence has been expected at the L to H transition, especially in the edge region where the radial electric field is enhanced. The experimental result shown in Fig. 5.16 is inconsistent with this expectation. The coherence is relatively low in L-mode and has not been reduced in H-mode. The cut-off density is about $1.0 \times 10^{19}\mathrm{m}^{-3}$. It is expected the cut-off layer lie in the region where the radial electric field is enhanced.

This low coherence feature in L-mode may be explained by the random phase screen model [93].

This model is based on the 1D geometrical optics. In this mode, two reflected wave is written in the form,

$$E_1 = e^{i\varphi_1}, \tag{6.1}$$

$$E_2 = e^{i\varphi_2}, \tag{6.2}$$

where φ_i is the phase of the reflected wave. The fluctuation of φ_i corresponds to the density fluctuation in this scheme. The coherence is written in the form,

$$\gamma_E = \frac{e^{\sigma_\varphi^2 \gamma_\varphi} - 1}{e^{\sigma_\varphi^2} - 1}, \tag{6.3}$$

where γ_φ is the coherence of the phase and $\sigma_\varphi = \langle \varphi^2 \rangle^{1/2}$. For large σ_φ, taking $\gamma_\varphi \approx \exp(-r^2/2l_\varphi^2)$ and making approximation $\gamma_\varphi \approx 1 - r^2/2l_\varphi^2$ for small r (i.e., for small cut-off layer separations compared to the correlation length of the phase screen l_φ) leads to the result,

$$\gamma_E \approx \exp(-r^2\sigma_\varphi^2/2l_\varphi^2). \tag{6.4}$$

Equation 6.4 says that the coherence is reduced if the density fluctuation is large. In the edge region in L-mode, the coherence γ_E can be small because the density fluctuation is large.

Though this model is based on the 1D geometrical optics, the same analogy can be kept in our model based on the scattering through φ_s in Eq. 4.1. We have not yet been able to understand the physical significance of φ_s. This is a future work

6.3 Shape of Spectrum

Kolmogorov spectrum,

$$S(k) \propto k^{-5/3}, \tag{6.5}$$

is satisfied on the wavenumber spectrum $S(k)$ when the local isotropy is satisfied. Kolmogorov-Kraichnan two-dimensional type spectrum,

$$S(k) \propto k^{-3}, \tag{6.6}$$

is satisfied when two-dimensional isotropy is satisfied.

If we assume $f \propto k$ like the dispersion relation of the sound wave, Eq. 6.5 becomes $f^{-5/3}$ and Eq. 6.6 becomes f^{-3}.

The the complex auto-power spectrums in the range of frequency higher than about 800 kHz in L-mode, higher than about 1 MHz in H-mode and lower than 20 kHz in H-mode are fitted with the form

$$S(f) \propto f^{-6\pm2}. \tag{6.7}$$

This is far from $f^{-5/3}$ or f^{-3}. This fact may indicate the turbulence is not isotropic in these frequency regions.

If we assume Eq. 6.7 is consistent with Eq. 6.5 or Eq. 6.6, we obtain the dispersion relation of $f \propto k^{0.3\pm0.1}$ or $f \propto k^{0.5\pm0.25}$. The feature of these dispersion relation resembles that of the dispersion relation of the electromagnetic wave in plasma in the range of the frequency $\omega \lesssim 0.8\omega_{ci}$, where ω_{ci} is the ion cyclotron frequency and about 10 MHz in our case.

7. Conclusion

The runaway phase phenomena is explained as follows: the complex amplitude E_R as the signal of the detector is described in the form,

$$E_R = E_0 \exp(i\varphi_0) + \sum_s E(\Omega_s) \exp i(\Omega_s t + \varphi_s), \tag{7.1}$$

where the first term is the reflected wave coming from the geometrical optics and the other terms are the waves scattered by the density fluctuations whose frequencies are Ω_s. The ratio of $E(\Omega_s)$ to E_0 is,

$$\left|\frac{E(\Omega_s)}{E_0}\right| \sim 10 \left.\frac{\tilde{n}(\Omega_s)}{n_c}\right|_{rms}, \tag{7.2}$$

when the density fluctuation of frequency Ω_s exists at the cut-off layer. Equation 7.2 means the contribution of the term with the frequency of Ω_s is larger than that of the first term in Eq. 7.1 when the level of the density fluctuation of frequency Ω_s is larger than 10 %. The complex amplitude E_R can rotate around the origin on the Gauss plane when the density fluctuation level is larger than 10 %. This is the runaway phase. We should take a new approach instead of the conventional phase measurement in order to derive the information of the density fluctuation from the data with the runaway phase. The data with the runaway phase should be analyzed as the data of the scattered wave. Furthermore the fluctuation measurement by the reflectometer should also be performed by regarding the received signals as the data of the scattered wave. The rotary spectrum and the complex spectrum analyses are tools to analyze such data.

The reflectometry based on the geometrical optics is realized by setting the receiving antenna far from the plasma in order to avoid the effect of the scattering waves caused by the fluctuations propagating in a direction perpendicular to the wavenumber vector of the incident wave. However this will be difficult because the alignment of the antenna is difficult.

The density fluctuation in L-mode and H-mode plasmas is discussed. The density fluctuation is analyzed by two methods. One is a conventional method which uses the data in the period when the runaway phase does not exist. The other is our new method. The results obtained by this new method are consistent with those obtained by using the data in the non-runaway phase periods and also give us additional information about the fluctuation. We have confirmed this method is effective especially when there exists the runaway phase.

We have observed that the reduction of the density fluctuation is localized in the edge region where the sheared electric field is produced. This supports Biglari's model that the sheared flow caused by the sheared electric field reduce the fluctuations [23]. The fluctuations in the range of frequency lower than 100 kHz are mainly reduced.

Two interesting features have been observed. One is the detection of the coherent mode around 100 kHz in H-mode. This mode appears about 10 ms after L to H transition. The timing corresponds to the formation of a steep density and temperature gradient in the edge region. The other is the enhancement of the fluctuations with the frequency higher than 300 kHz in H-mode in contrast to the well-known reduction of the fluctuations with the frequency lower than 100 kHz. This result has never been reported. The investigation of these two features remains as future work to be investigated.

The feature of the Doppler shift is observed in the complex auto-power spectrum of the reflected wave when the plasma is actively moved. We have confirmed that the movement of the plasma is appropriately measured by using the low pass filter. The reflectometer can be used to measure the density profile by using a low pass filter.

Acknowledgment

I would like to express my sincere gratitude to Professor H. Toyama for his continuous encouragement to do experiments and advice on this work. I would like to thank Dr. K. Hanada for his valuable comments and help.

I am very grateful to Dr. N. Suzuki (JAERI), Dr. K. Hoshino (JAERI), Dr. Y. Miura (JAERI), Dr. T. Yamauchi (JAERI) and JFT-2M Group for their support of my experiment and useful discussion.

The collaboration with Mr. S. Shiraiwa is greatly appreciated. I also thank Mr. Yamagishi, Ms. S. Duorah, Mr. H. Totsuka, Mr. E. Ishiyama, Mr. M. Hasegawa, Mr. H. Saito, Mr. I. Nakajima and Mr. M. Ushigome for various help.

I greatly appreciate fruitful discussions with Dr. A. Mase (GAMMA 10), Dr. T. Fukuda (JAERI) and Dr. A. Ejiri (NIFS). I also want to dedicate this thesis to the memory of Dr. H. Maeda (JAERI).

I wish to thank my parents and brother for various support.

Finally, I am grateful to my wife Keiko.

References

[1] K. Nishikawa and M. Wakatani, *Plasma Physics*, Springer-Verlag, 1990.

[2] L. A. Artsimovich, Nucl. Fusion **12**, 215 (1972).

[3] P. C. Liewer, Nucl. Fusion **25**, 543 (1985).

[4] A. J. Wooton and R. Fonck, Fluctuations and local transport – latest developments, in *International School of Plasma Physics "PERO CALDIROLA" (Proceedings of the Cource and Workshop held in Varenna, Italy)*, pages 201–222, Bologna, 1993, Editrice Compositori.

[5] F. Wagner et al., Phys. Rev. Lett. **49**, 1408 (1982).

[6] F. X. Söldner et al., Phys. Rev. Lett. **61**, 1105 (1988).

[7] Y. Koide et al., Phys. Rev. Lett. **72**, 3662 (1994).

[8] G. L. Jackson et al., Phys. Rev. Lett. **67**, 3098 (1991).

[9] E. J. Strait et al., Phys. Rev. Lett. **75**, 4421 (1995).

[10] F. M. Levinton et al., Phys. Rev. Lett. **75**, 4417 (1995).

[11] M. Mori et al., Nucl. Fusion **34**, 1045 (1994).

[12] F. F. Chen, *Introduction to PLASMA PHYSICS AND CONTROLLED FUSION*, volume 1, Plenum Press, second edition, 1984.

[13] K. Hanada et al., Phys. Rev. Lett. **66**, 1974 (1991).

[14] J. Team, JET latest results and future prospects, in *Plasma Physics and Controlled Nuclear Fusion Research (Proc. 11th Int. Conf. Kyoto), IAEA-CN-47/A-I-2*, Vienna, 1986, IAEA.

[15] H. Eubank et al., Phys. Rev. Lett. **43**, 270 (1979).

[16] F. Wagner et al., Recent results of H-mode studies on ASDEX, in *Plasma Physics and Controlled Nuclear Fusion Research (Proc. 13th Int. Conf. Seville), IAEA-CN-53/A-IV-2*, pages 277–290, Washington, D.C., 1990, IAEA.

[17] K. H. Burrell et al., Phys. Fluids B **2**, 1405 (1990).

[18] K. H. Burrell et al., H-mode and VH-mode confinement improvement in DIII-D: Improvements of turbulence, local transport and acrive control of the shear in the $E \times B$ flow, in *Plasma Physics and Controlled Nuclear Fusion Research (Proc. 15th Int. Conf. Seville), IAEA-CN-60/A2-5*, pages 221–239, Vienna, 1994, IAEA.

[19] P. Gohil et al., Nucl. Fusion **34**, 1057 (1994).

[20] R. A. Moyer et al., Phys. Plasmas **2**, 2397 (1995).

[21] S.-I. Itoh and K. Itoh, Phys. Rev. Lett. **60**, 2276 (1988).

[22] K. C. Shaing and E. C. Crume, Jr., Phys. Rev. Lett. **63**, 2369 (1989).

[23] H. Biglari, P. H. Diamond, and P. W. Terry, Phys. Fluids **2**, 1 (1990).

[24] G. R. Tynan et al., Phys. Plasmas **1**, 3301 (1994).

[25] C. Hidalgo et al., Nucl. Fusion **30** (1990).

[26] H. J. Knuze, *Plasma Diagnostics*, chapter 9, North-Holland Publishing Company, 1968.

[27] J. Sheffield, *Plasma Scattering of Electromagnetic Radiation*, chapter Scattered Power Spectrum, pages 23–36, Academic Press, New York, 1975.

[28] E. Mazzucato, Phys. Rev. Lett. **36**, 792 (1976).

[29] R. E. Slusher and C. M. Surko, Phys. Fluids **23**, 472 (1980).

[30] N. L. Bretz, R. Nazikian, and K. L. Wong, Density fluctuation measurements from microwave scattering on TFTR, in *Proceedings of 17th EPS Conf. on Control. Fusion and Plasma Phys.*, volume 14B, pages 1544–1547, European Physical Society, 1990.

[31] R. J. Fonck, P. A. Duperrex, and S. F. Paul, Rev. Sci. Instrum. **61**, 3487 (1990).

[32] R. J. Fonck et al., Phys. Rev. Lett. **70**, 3736 (1993).

[33] P. M. Schoch et al., Rev. Sci. Instrum. **59**, 1646 (1988).

[34] M. E. Manso, Plasma Phys. Controlled Fusion **35**, B141 (1993).

[35] N. L. Bretz, Nucl. Fusion **34**, 1283 (1994).

[36] A. E. Costley, Diagnosis of fusion plasma using reflectometry, in *International School of Plasma Physics "PERO CALDIROLA" (Proceedings of the Cource and Workshop held in Varenna, Italy)*, pages 379–396, Bologna, 1986, Editrice Compositori.

[37] C. Laviron, A. J. H. Donné, M. E. Manso, and J. Sanchez, Plasma Phys. Controlled Fusion **38**, 905 (1996).

[38] H. Bottollier-Curtet and G. Ichtchenko, Rev. Sci. Instrum. **58**, 539 (1987).

[39] F. Simonet, Rev. Sci. Instrum. **56**, 664 (1985).

[40] E. TFR, Nucl. Fusion **18**, 647 (1978).

[41] J. L. Doane, E. Mazzucato, and G. L. Schmidt, Rev. Sci. Instrum. **52**, 12 (1981).

[42] A. E. Hubbard, A. E. Costley, and C. W. Gowers, J. Phys. E: Sci. Instrum. **20**, 423 (1987).

[43] E. Anabitarte et al., J. Phys. D: Appl. Phys. **21**, 1384 (1988).

[44] M. E. Manso et al., Broadband microwave reflectometry on ASDEX, in *Proceedings of 16th EPS Conf. on Control. Fusion and Plasma Phys.*, volume 13B, pages 1517–1520, European Physical Society, 1989.

[45] T. Fukuda, Reflectometric measurements of the JT-60 tokamak, in *Proceedings of the 4th International Symposium on Laser-aided Plasma Diagnostics*, volume 2, pages 13–16, Kyushu, 1989.

[46] A. E. Costley, P. Cripwell, R. Prentice, and A. C. C. Sips, Rev. Sci. Instrum. **61**, 2823 (1990).

[47] E. J. Doyle, T. Lehecka, N. C. Luhmann, Jr, W. A. Peebles, and the DIII-D Group, X-mode broadband reflectometric density profile measurements on DIII-D, in *Proceedings of 17th EPS Conf. on Control. Fusion and Plasma Phys.*, volume 14B, pages 1596–1599, European Physical Society, 1990.

[48] G. R. Hanson, J. B. Wilgen, T. S. Bigelow, I. Collazo, and C. E. Thomas, Rev. Sci. Instrum. **63**, 4658 (1992).

[49] A. C. C. Sips and G. J. Kramer, Plasma Phys. Controlled Fusion **35**, 743 (1993).

[50] J. Sanchez et al., Plasma Phys. Rep. **20**, 1 (1994).

[51] A. I. Skibenko, O. S. Pavlichenko, R. O. Pavlichneko, and I. P. Fomin, Plasma Phys. Rep. **20**, 7 (1994).

[52] E. de la Luna et al., Rev. Sci. Instrum. **66**, 403 (1995).

[53] M. Moresco, R. Cavazzana, A. Sardella, and E. Spada, Rev. Sci. Instrum. **66**, 406 (1995).

[54] P. Buratti, M. Zerbini, Y. Brodsky, N. Kovalev, and A. Shtanuk, Rev. Sci. Instrum. **66**, 409 (1995).

[55] T. Tokuzawa et al., Jpn. J. Appl. Phys. **34**, L76 (1995).

[56] K. W. Kim et al., Rev. Sci. Instrum. **66**, 1229 (1995).

[57] M. E. Manso, Density profile and fluctuation measurements in ASDEX Upgrade with ultrafast FM-broadband reflectometry, in *Proceedings of the 7th International Symposium on Laser-aided Plasma Diagnostics*, pages 246–253, Kyushu, 1995.

[58] M. Hirsch, H. J. Hartfuss, T. Geist, and E. de la Luna, Rev. Sci. Instrum. **67**, 1807 (1996).

[59] A. Silva et al., A microwave reflectometer system for tokamak ASDEX Upgrade, in *Proceedings of 19th EPS Conf. on Control. Fusion and Plasma Phys.*, volume 16, pages 1063–1066, European Physical Society, 1992.

[60] J. L. Doane, Rev. Sci. Instrum. **51**, 317 (1980).

[61] J. Sánchez, B. Brañas, T. Estrada, E. de la Luna, and V. Zhuravlev, Rev. Sci. Instrum. **63**, 4654 (1992).

[62] C. A. J. Hugenholtz and S. H. Heijnen, Rev. Sci. Instrum. **62**, 1100 (1991).

[63] C. W. Domier et al., Rev. Sci. Instrum. **63**, 4666 (1992).

[64] V. F. Shevchenko, A. A. Petrov, V. G. Petrov, and Y. A. Chaplygin, Plasma Phys. Rep. **20**, 27 (1994).

[65] C. W. Domier, N. C. Luhmann, Jr., A. E. Chou, W.-M. Zhang, and A. J. Romanowsky, Rev. Sci. Instrum. **66**, 339 (1995).

[66] S. H. Heijnen et al., Rev. Sci. Instrum. **66**, 419 (1995).

[67] A. J. H. Donné, S. H. Heijnen, and C. A. J. Hugenholtz, Fusion Eng. Design (1997), (to be published).

[68] E. Mazzucato, Density fluctuations in the adiabatic toroidal compressor, Princeton Plasma Physics Laboratory, Princeton University, Report MATT-1151,1975.

[69] S. M. Hamberger, L. E. Sharp, J. B. Lister, and S. Mrowka, Phys. Rev. Lett. **37**, 1345 (1976).

[70] TFR Group, Plasma Phys. Controlled Fusion **27**, 1299 (1985).

[71] I. Sanchez, E. Anabitarte, A. P. Navapro, and H. J. Hartfuss, Broadband microwave reflectometry on Wendelstein VII-AS stellarator, in *Proceedings of 16th EPS Conf. on Control. Fusion and Plasma Phys.*, volume 13B, pages 1565–1568, European Physical Society, 1989.

[72] T. Lehechka et al., Results from the DIII-D millimeter-wave reflectometer, in *Proceedings of 16th EPS Conf. on Control. Fusion and Plasma Phys.*, volume 13B, pages 123–126, European Physical Society, 1989.

[73] T. Estrada, J. Sánchez, B. Brañas, and A. P. Navarro, Rev. Sci. Instrum. **61**, 3034 (1990).

[74] J. Sanchez Sanz et al., Nucl. Fusion **30**, 2383 (1990).

[75] E. J. Doyle et al., Rev. Sci. Instrum. **61**, 3016 (1990).

[76] T. Fukuda et al., Rev. Sci. Instrum. **61**, 3524 (1990).

[77] G. R. Hanson et al., Nucl. Fusion **32**, 1593 (1992).

[78] E. Mazzucato, R. Nazikian, and the TFTR-Group, The application of X-mode reflectometry to the study of large scale fluctuations in TFTR, in *Proceedings of 19th EPS Conf. on Control. Fusion and Plasma Phys.*, volume 16, pages 1055–1058, European Physical Society, 1992.

[79] R. Cesario et al., Nucl. Fusion **32**, 2127 (1992).

[80] A. Ejiri, K. Kawahata, T. Seki, T. Watari, and K. Tanaka, Density fluctuation measurements by homodyne reflectometer during IBW injection, NIFS report, 154, (1994).

[81] H. Hartfuss, T. Estrada, M. Hirsch, and T. Geist, Rev. Sci. Instrum. **7**, 2284 (1994).

[82] V. A. Vershkov et al., Resutls of turbulence investigations on T-10 with correlation reflectometry and multipine Langmuir probe, in *Plasma Physics and Controlled Nuclear Fusion Research (Proc. 15th Int. Conf. Seville), IAEA-CN-60/A2/A4-P8*, pages 65–71, Vienna, 1994, IAEA.

[83] G. D. Conway, L. Schott, and A. Hirose, Plasma Phys. Controlled Fusion **38**, 451 (1996).

[84] E. Mazzucato et al., Phys. Rev. Lett. **77**, 3145 (1996).

[85] S. H. Nazikian, R. Batha et al., Observation of alpha-particle driven toroidal Alfven eignemodes in TFTR DT plasmas, in *Plasma Physics and Controlled Nuclear Fusion Research 1996 (Proc. 16th Int. Conf. Montéal, 1996), IAEA-CN-64/A2-4*, pages –, Vienna, 1996, IAEA.

[86] T. L. Rhodes, R. J. Taylor, E. J. Doyle, N. C. Luhmann, Jr., and W. A. Peebles, Nucl. Fusion **33**, 1787 (1993).

[87] A. C. Sips, A. E. Costley, J. C. M. de Haas, and R. Prentice, Measurements of the electron particle diffusion coefficient with the JET multichannel reflectometer, in *Proceedings of 16th EPS Conf. on Control. Fusion and Plasma Phys.*, volume 13B, pages 99–102, European Physical Society, 1989.

[88] R. Schubert et al., Edge density X-mode reflectometer of RF-heated plasmas on ASDEX, in *Proceedings of 17th EPS Conf. on Control. Fusion and Plasma Phys.*, volume 14B, pages 1552–1555, European Physical Society, 1990.

[89] E. J. Doyle, T. L. Rhodes, J. L. Doane, and W. A. Peebles, Rev. Sci. Instrum. **66**, 1233 (1995).

[90] P. Cripwell, A. E. Costley, and A. E. Hubbard, Correlation reflectometer, in *Proceedings of 16th EPS Conf. on Control. Fusion and Plasma Phys.*, volume 13B, pages 75–78, European Physical Society, 1989.

[91] G. R. Hanson et al., Rev. Sci. Instrum. **61**, 3049 (1990).

[92] T. L. Rhodes, W. A. Peebles, and E. J. Doyle, Rev. Sci. Instrum. **63**, 4661 (1992).

[93] E. Mazzucato and R. Nazikian, Phys. Rev. Lett. **71**, 1840 (1993).

[94] J. Sanchez, B. Brañas, E. de la Luna, and T. Estrada, Rev. Sci. Instrum. **64**, 487 (1993).

[95] J. D. Strachan et al., Phys. Rev. Lett. **58**, 1004 (1987).

[96] S. Baang, C. W. Domier, N. C. Luhmann, Jr., W. Peebles, and T. L. Rhodes, Rev. Sci. Instrum. **61**, 3013 (1990).

[97] T. L. Rhodes et al., Rev. Sci. Instrum. **63**, 4599 (1992).

[98] N. Bretz, Phys. Fluids B **4**, 2414 (1992).

[99] V. N. Budnikov et al., Fusion Eng. Design (1997), (to be published).

[100] A. Mase et al., Phys. Fluids B **5**, 1677 (1993).

[101] J. H. Lee et al., Rev. Sci. Instrum. **66**, 1225 (1995).

[102] K. Shinohara, Measurement of density fluctuations by the reflectometer on JFT-2M, REPUTE-1 Annual Report 1994, 33.

[103] A. Ejiri, K. Kawahata, and K. Tanaka, Heterodyne microwave reflectometer, NIFS report, 155, (1994).

[104] K. Shinohara et al., Fusion Eng. Design (1997), (to be published).

[105] V. V. Bulanin and D. O. Korneev, Plasma Phys. Rep. **20**, 14 (1994).

[106] B. Brañas et al., Frequency shift of reflectometer signals due to rotation of density turbulence in W7-AS, in *Proceedings of 23th EPS Conf. on Control. Fusion and Plasma Phys.*, volume 20, European Physical Society, 1996.

[107] M. Hirch et al., Edge transport barrier and edge turbulence during H-mode operation in the W7-AS stellarator, in *Plasma Physics and Controlled Nuclear Fusion Research 1996 (Proc. 16th Int. Conf. Montéal, 1996), IAEA-CN-60/A2/A4-P8, IAEA*, Vienna, 1996, IAEA.

[108] J. H. Irby and P. Stek, Rev. Sci. Instrum. **61**, 3052 (1990).

[109] I. H. Hutchinson, Plasma Phys. Controlled Fusion **34**, 1225 (1992).

[110] J. P. Garcia, M. E. Manso, J. T. Mendoça, and F. M. Serra, Scattering effects of small-scale density fluctuations on reflectometric measurements in a tokamak plasma, in *Proceedings of 16th EPS Conf. on Control. Fusion and Plasma Phys.*, volume 13B, pages 1521–1524, European Physical Society, 1989.

[111] E. Mazzucato and R. Nazikian, Plasma Phys. Controlled Fusion **33**, 261 (1991).

[112] X. L. Zou, L. Laurent, and J. M. Rax, Plasma Phys. Controlled Fusion **33**, 903 (1991).

[113] P. Michelson and H. Pécseli, Simulation of correlation reflectometry, in *Proceedings of 19th EPS Conf. on Control. Fusion and Plasma Phys.*, volume 16, pages 1067–1070, European Physical Society, 1992.

[114] A. E. Chou, B. B. Afeyan, and B. I. Cohen, Rev. Sci. Instrum. **66**, 1216 (1995).

[115] B. B. Afeyan, A. E. Chou, and B. I. Cohen, Plasma Phys. Controlled Fusion **37**, 315 (1995).

[116] C. Fanack et al., Plasma Phys. Controlled Fusion **38**, 1915 (1996).

[117] J. Irby, S. Horne, I. H. Hutchinson, and P. C. Stek, Plasma Phys. Controlled Fusion **35**, 601 (1993).

[118] L. G. Bruskin, A. Mase, and T. Tamano, Plasma Phys. Controlled Fusion **37**, 255 (1995).

[119] E. Mazzucato and R. Nazikian, Rev. Sci. Instrum. **66**, 1237 (1995).

[120] G. D. Conway, L. Schott, and A. Hirose, Rev. Sci. Instrum. **67**, 3861 (1996).

[121] R. Nazikian and E. Mazzucato, Rev. Sci. Instrum. **66**, 392 (1995).

[122] L. G. Bruskin, A. Mase, and T. Tamano, J. Plasma Fusion Research **72**, 356 (1996).

[123] M. Brambilla and M. Moresco, Plasma Phys. Controlled Fusion **29**, 381 (1987).

[124] M. Moresco, R. O' Dubhghaill, and E. Spada, Int. J. Infrared Millimeter Waves **12**, 609 (1992).

[125] A. Ejiri and K. Nagasaki, Optimum poralization for microwave reflectometry in a sheared magnetic field, NIFS report, 196, (1994).

[126] L. G. Bruskin, A. Mase, and T. Tamano, Plasma Phys. Controlled Fusion **36**, 681 (1994).

[127] M. Nagatsu, T. Hayashi, Y. Matsuhisa, and T. Tsukishima, Jpn. J. Appl. Phys. **33**, 45 (1994).

[128] B. I. Cohen, B. B. Afeyan, A. E. Chou, and N. C. Luhmann, Jr, Rev. Sci. Instrum. **66**, 1241 (1995).

[129] T. Shoji et al., Proceedings of 11th EPS Conf. on Control. Fusion and Plasma Phys. **7D**, 55 (1983).

[130] K. Odajima et al., Confinement studies of additionally heated plasma in the JFT-2M tokamak, in *Plasma Physics and Controlled Nuclear Fusion Research (Proc. 11th Int. Conf. Kyoto), IAEA-CN-47/A-III-2*, pages 151–157, Vienna, 1986, IAEA.

[131] K. Hoshino et al., Phys. Lett. A **124**, 299 (1987).

[132] N. Suzuki et al., Confinement studies of the H-mode on JFT-2M, in *Plasma Physics and Controlled Nuclear Fusion Research (Proc. 12th Int. Conf. Nice), IAEA-CN-50/A-III-5*, pages 207–213, Vienna, 1988, IAEA.

[133] K. Hoshino et al., Phys. Rev. Lett. **63**, 770 (1989).

[134] K. Ida et al., Phys. Rev. Lett. **65**, 1364 (1990).

[135] Y. Miura et al., Phys. Rev. Lett. **69**, 2216 (1992).

[136] Y. Miura et al., Divertor biasing effects to reduce L/H power threshold in the JFT-2M tokamak, in *Plasma Physics and Controlled Nuclear Fusion Research (Proc. 16th Int. Conf. Montéal), IAEA-CN-64/O2-4*, Vienna, 1996, IAEA.

[137] R. J. King, *Microwave Homodyne Systems*, chapter Principles of coherent detection, Peter Peregrinus Ltd., Stevenage, 1978.

[138] V. L. Ginzburg, *The Propagation of Electromagnetic Waves in Plasmas*, Oxford:Pergamon, 1964.

[139] M. L. Pitteway, Proc. Roy. Soc. **A246**, 556 (1958).

[140] X. L. Zou, L. Laurent, T. Lehner, and R. M. Rax, Localization of fluctuation measurement by wave scattering close to a cut off layer, in *Proceedings of 17th EPS Conf. on Control. Fusion and Plasma Phys.*, volume 14B, pages 1693–1696, European Physical Society, 1990.

[141] J. D. Jackson, *Classical Electrodynamics*, Jhon Wiley & Sons, Inc, New York, second edition, 1975.

[142] H. Toyama et al., Observation of turbulence suppression and transport reduction in the presence of sheared flow, in *Plasma Physics and Controlled Nuclear Fusion Research (Proc. 15th Int. Conf. Seville), IAEA-CN-60/A-4-II-3*, pages 575–581, Vienna, 1994, IAEA.

[143] T. Yamauchi et al., Jpn. J. Appl. Phys. **31**, 2255 (1992).

[144] S. I. Itoh and K. Itoh, J. Phys. Soc. Jpn **59**, 3815 (1990).

[145] K. Ida et al., Phys. Fluids **4**, 2552 (1992).

[146] E. J. Synakowski et al., Particle and energy transport studies on TFTR and implications for helium ash in future fusion devices, in *Plasma Physics and Controlled Nuclear Fusion Research (Proc. 14th Int. Conf. Würzburg), IAEA-CN-56/A-7-16*, pages 541–550, Vienna, 1992, IAEA.

[147] J. O'Rourke et al., Plasma Phys. Controlled Fusion **35**, 585 (1993).

[148] M. Hino, *Sectrum Analysis*, Asakura Shoten, 1977, [in Japanese].

[149] A. Ejiri and K. Kawahata, Phase runaway phenomena in micorwave reflectometry, NIFS report, 194, (1995).

[150] A. Ejiri, K. Kawahata, K. Tanaka, and JIPP TII-U group, Fusion Eng. Design (1997), (to be published).

Appendix A

Tokamak Coordinate

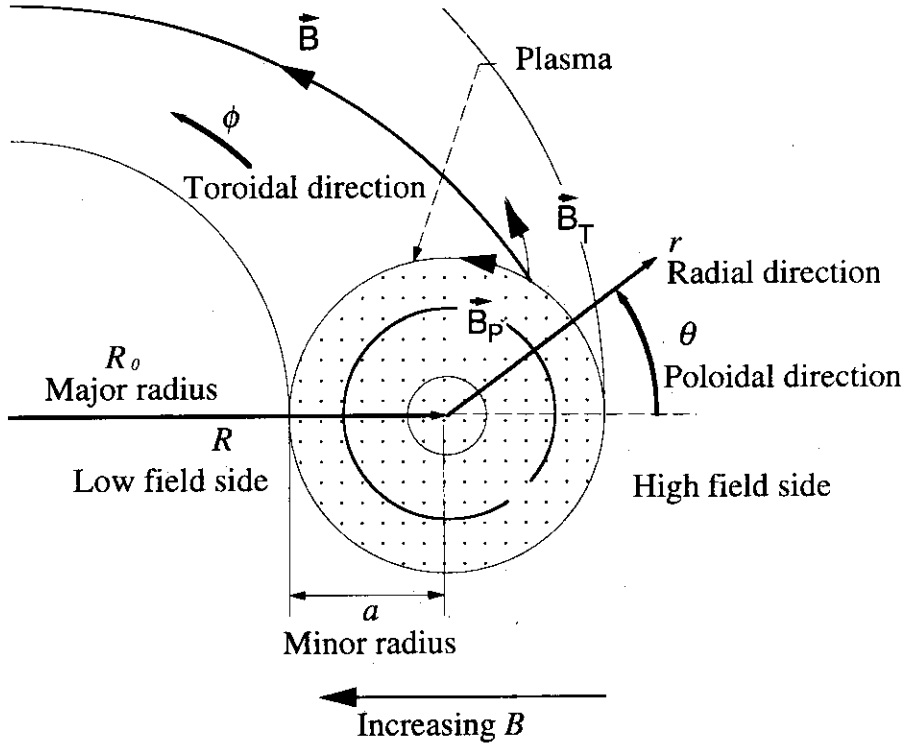

Figure A.1: Tokamak coordinate

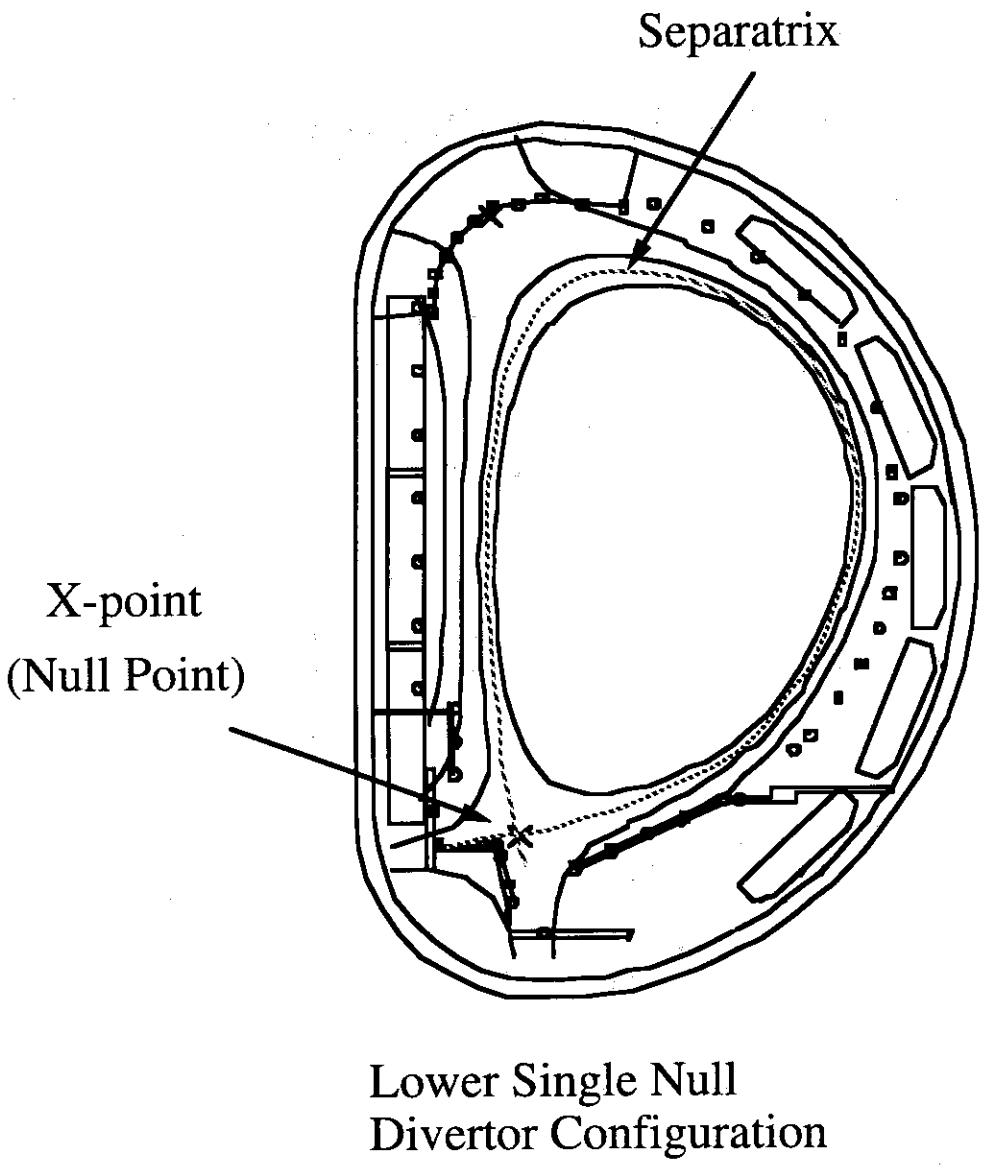

Figure A.2: Divertor Configuration: X-point (Null Point) is the point where the poloidal magnetic field becomes zero. Separatrix is the flux surface which pass through the X-point. Lower single null (LSN) configuration has the X-point in lower side of the equatorial plane. Upper single null (USN) configuration has the X-point in upper side of the equatorial plane.

Appendix B

Spectrum of Scalar Time Series [148]

The auto-power spectrum, the cross spectrum and the coherence of two scalar (real) time series $a(t)$ and $b(t)$ are defined as below:

Auto-power spectrum:

$$S_{aa}(\omega) = 2\pi \langle A(\omega)A^*(\omega)\rangle /T \tag{B.1}$$

$$S_{bb}(\omega) = 2\pi \langle B(\omega)B^*(\omega)\rangle /T \tag{B.2}$$

Cross spectrum:

$$S_{ab}(\omega) = 2\pi \langle A(\omega)B^*(\omega)\rangle /T \tag{B.3}$$

Coherence:

$$\begin{aligned} \mathrm{Coh}(\omega) &= |\mathrm{Coh}(\omega)|\, e^{i\theta_{ab}(\omega)} \\ &= S_{ab}(\omega)/(S_{aa}(\omega)S_{bb}(\omega))^{1/2} \end{aligned} \tag{B.4}$$

$$\gamma = |\mathrm{Coh}(\omega)| \qquad \text{:Coherency} \tag{B.5}$$

$$\theta_{ab}(\omega) \qquad \text{:Cross phase} \tag{B.6}$$

where <> means the ensemble average.

Here $A(\omega)$ and $B(\omega)$ satisfy the following equations:

$$\begin{aligned} A(\omega) &= \frac{1}{2\pi}\int_{-\infty}^{\infty} d\omega a(t)e^{-i\omega t}, \\ B(\omega) &= \frac{1}{2\pi}\int_{-\infty}^{\infty} d\omega b(t)e^{-i\omega t}. \end{aligned}$$

The equation,

$$A(-\omega) = \frac{1}{2\pi}\int_{-\infty}^{\infty} d\omega a(t)e^{i\omega t} = A^*(\omega), \tag{B.7}$$

holds because $a(t)$ is real. Thus auto-power spectrum of the scalar time series has symmetry of $S_{aa}(-\omega) = S_{aa}(\omega)$.

Appendix C

Rotary Spectrum [148]

The time series of $z(t) = x(t) + iy(t)$ is the complex time series, or vector time series. We define $Z_{ccw}(\omega)$ and $Z_{cw}(\omega)$ so that they satisfy the following relation:

$$\begin{aligned} z(t) &= x(t) + iy(i) \\ &= \frac{1}{2\pi}\int_0^\infty d\omega \left[Z_{ccw}(\omega)e^{i\omega t} + Z_{cw}(\omega)e^{-i\omega t} \right]. \end{aligned} \tag{C.1}$$

In this appendix, we set $\omega \geq 0$.

We define $\theta_{ccw}(\omega)$, $\theta_{cw}(\omega)$, $W_{ccw}(\omega)$ and $W_{cw}(\omega)$ as

$$Z_{ccw}(\omega) = |Z_{ccw}(\omega)|\, e^{i\theta_{ccw}(\omega)}, \tag{C.2}$$

$$Z_{cw}(\omega) = |Z_{cw}(\omega)|\, e^{i\theta_{cw}(\omega)}, \tag{C.3}$$

$$W_{ccw}(\omega) = |Z_{ccw}(\omega)|\,, \tag{C.4}$$

$$W_{cw}(\omega) = |Z_{cw}(\omega)|\,. \tag{C.5}$$

Eq. C.1 is rewritten using $\theta_{ccw}(\omega)$, $\theta_{cw}(\omega)$, $W_{ccw}(\omega)$ and $W_{cw}(\omega)$ as below:

$$x(t) = \frac{1}{2\pi}\int_0^\infty d\omega \left[W_{ccw}(\omega)\cos(\omega t + \theta_{ccw}(\omega)) + W_{cw}(\omega)\cos(-\omega t + \theta_{cw}(\omega)) \right], \tag{C.6}$$

$$y(t) = \frac{1}{2\pi}\int_0^\infty d\omega \left[W_{ccw}(\omega)\sin(\omega t + \theta_{ccw}(\omega)) + W_{cw}(\omega)\sin(-\omega t + \theta_{cw}(\omega)) \right]. \tag{C.7}$$

From these expressions, we notice that $z(t)$ consists of many circular motions. One of them rotates in the counter clockwise (CCW) direction with the angular frequency ω and the radius $W_{ccw}(\omega)$ and another of them rotates in the clockwise (CW) direction with the angular frequency ω and the radius $W_{cw}(\omega)$.

We consider the circular motions for each frequency. At first, we consider the case where $\theta_{ccw}(\omega) = \theta_{cw}(\omega) = 0$. We define $X(\omega)$ and $Y(\omega)$ as

$$\begin{pmatrix} X(\omega) \\ Y(\omega) \end{pmatrix} = W_{ccw}(\omega) \begin{pmatrix} \cos(\omega t) \\ \sin(\omega t) \end{pmatrix} + W_{cw}(\omega) \begin{pmatrix} \cos(-\omega t) \\ \sin(-\omega t) \end{pmatrix}, \tag{C.8}$$

and thus obtain,

$$\frac{X^2}{(W_{ccw} + W_{cw})^2} + \frac{Y^2}{(W_{ccw} - W_{cw})^2} = 1. \tag{C.9}$$

This is an ellipse with the principal axis coinciding with the real axis.

We consider the case where $\theta_{ccw}(\omega) \neq 0$ and $\theta_{cw}(\omega) \neq 0$ and redefine $X(\omega)$ and $Y(\omega)$ as

$$\begin{aligned} X(\omega) &= W_{ccw}(\omega)\cos(\omega t + \theta_{ccw}) + W_{cw}(\omega)\cos(-\omega t + \theta_{cw}) \\ Y(\omega) &= W_{ccw}(\omega)\sin(\omega t + \theta_{ccw}) + W_{cw}(\omega)\sin(-\omega t + \theta_{cw}) \end{aligned} \tag{C.10}$$

We set $t = t' + (\theta_{cw}(\omega) - \theta_{ccw}(\omega))/2\omega$ in each frequency of Eq. C.6 and C.7, then,

$$\begin{pmatrix} X(\omega) \\ Y(\omega) \end{pmatrix} = \begin{pmatrix} \cos\left((\theta_{ccw} + \theta_{cw})/2\right) & -\sin\left((\theta_{ccw} + \theta_{cw})/2\right) \\ \sin\left((\theta_{ccw} + \theta_{cw})/2\right) & \cos\left((\theta_{ccw} + \theta_{cw})/2\right) \end{pmatrix} \times \left[W_{ccw}(\omega) \begin{pmatrix} \cos(\omega t') \\ \sin(\omega t') \end{pmatrix} + W_{cw}(\omega) \begin{pmatrix} \cos(-\omega t') \\ \sin(-\omega t') \end{pmatrix} \right]. \quad \text{(C.11)}$$

Comparing with Eq. C.8, we know this equation draws an ellipse with the principal axis making an angle of $(\theta_{cw}(\omega) - \theta_{ccw}(\omega))/2$ radian with the real axis.

Therefore Eq. C.10 or $Z(\omega) = Z_{ccw}(\omega) + Z_{cw}(\omega)$ means that the point $(X(\omega), Y(\omega))$ rotates with a period of $2\pi/\omega$ on the ellipse with the principal axis making an angle of $(\theta_{cw}(\omega) - \theta_{ccw}(\omega))/2$ radian with the real axis.

We can now understand the meaning of rotary spectrum defined as follows: (<> means the ensemble average.)

Counter clockwise spectrum:

$$S_{ccw}(\omega) = 2\pi \left\langle Z^*_{ccw}(\omega) Z_{ccw}(\omega) \right\rangle / T. \quad \text{(C.12)}$$

This corresponds to the positive frequency component of the complex auto-power spectrum (see Appendix D).

Clockwise spectrum:

$$S_{cw}(\omega) = 2\pi \left\langle Z^*_{cw}(\omega) Z_{cw}(\omega) \right\rangle / T. \quad \text{(C.13)}$$

This corresponds to the negative frequency component of the complex auto-power spectrum.

Total spectrum:

$$S_t(\omega) = S_{ccw} + S_{cw}. \quad \text{(C.14)}$$

Rotary coefficient:

$$C_R(\omega) = \left(S_{ccw}(\omega) - S_{cw}(\omega)\right) / S_t(\omega), \quad \text{(C.15)}$$

which means the ratio of the power of the rotation to the total power. (The value of $S_{ccw}(\omega) - S_{cw}(\omega)$ is proportional to the area of the ellipse.) A perfect circle coming from CCW motion is drawn if $C_R(\omega) = 1$. A perfect circle coming from CW motion is drawn if $C_R(\omega) = -1$. A line whose gradient is $\tan(\theta_{ccw} + \theta_{cw})/2$ is drawn if $C_R(\omega) = 0$.

Appendix D

Complex Spectrum [148]

We can also define the auto-power spectrum and the cross spectrum of two complex time series, or vector time series,$z(t) = x(t) + iy(t)$ and $w(t) = u(t) + iv(t)$ in the same way as two scalar (real) time series. (<> means the ensemble average.)

Auto-power spectrum:

$$S_{ww}(\omega) = 2\pi \langle W(\omega)W^*(\omega)\rangle /T \tag{D.1}$$

$$S_{zz}(\omega) = 2\pi \langle Z(\omega)Z^*(\omega)\rangle /T \tag{D.2}$$

Cross spectrum:

$$S_{wz}(\omega) = 2\pi \langle W(\omega)Z^*(\omega)\rangle /T \tag{D.3}$$

Coherence:

$$\begin{aligned} \mathrm{Coh}(\omega) &= |\mathrm{Coh}(\omega)|\, e^{i\theta_{wz}(\omega)} \\ &= S_{wz}(\omega)/(S_{ww}(\omega)S_{zz}(\omega))^{1/2} \end{aligned} \tag{D.4}$$

$$\gamma = |\mathrm{Coh}(\omega)| \qquad \text{:Coherency} \tag{D.5}$$

$$\theta_{wz}(\omega) \qquad \text{:Cross phase} \tag{D.6}$$

Here $W(\omega)$ and $Z(\omega)$ satisfy the next equations:

$$w(t) = \int_{-\infty}^{\infty} d\omega W(\omega)e^{i\omega t},$$

$$z(t) = \int_{-\infty}^{\infty} d\omega Z(\omega)e^{i\omega t}.$$

The positive frequency components and the negative frequency components of the complex spectrum do not have symmetry while those of the spectrum of the scalar time series have symmetry (Appendix B). The value of $S_{ww}(\omega)$ $(\omega > 0)$ shows the power of the counter clockwise rotation with frequency ω, included in the movement of the complex time series $w(t)$, on the Gaussian plane and the value of $S_{ww}(\omega)$ $(\omega < 0)$ shows the power of the clockwise rotation. (see also Appendix C)

To apply the method of the complex spectrum to data from our reflectometer, we set,

$$\begin{aligned} z(t) &= (\text{ cosine output of phase sensitive detector of ch.1}) \\ &+ i(\text{ sine output of phase sensitive detector of ch.1}), \end{aligned} \tag{D.7}$$

$$\begin{aligned} w(t) &= (\text{ cosine output of phase sensitive detector of ch.2}) \\ &+ i(\text{ sine output of phase sensitive detector of ch.2}), \end{aligned} \tag{D.8}$$

where $z(t)$ and $w(t)$ show the complex amplitude $E_R(t)$ of the received signal $E_R(t)e^{i\omega_0 t}$, and ω_0 is the frequency of the incident wave.

Appendix E

Automatic Method of Rejecting Runaway Phase Period

We have obtained the evaluation of the spectrum and the level of the fluctuation from the phase data obtained during the flat phase in the step-like runaway phase as shown in Fig. 3.3. This method of excluding the phase runaway have been performed manually.

The time scale of the step-like structure varies from a few μs to tens of μs, while there are changes of fluctuating phase whose differential coefficient with respect to time is similar to that of the step-like structure. It is inappropriate to reject the change of the phase by setting the upper limit in the phase difference between the sequential data points or in the differential coefficient of the change of the phase with respect to time. For example, we let the upper limit be $\pi/2$ in the phase difference between the sequential data points. We can not obtain the density fluctuation whose frequency is 100 kHz and $\tilde{n}/n \sim 8\%$ because this fluctuation change no less than $2\pi/3$ radian during a period, 0.2 μ, between two sequential data points at the peak.

There appears a difference between the time averages of phase before and after the runaway occur. The difference between the time averages of phase can be a good indicator of the appearance of the runaway phase. The data without the runaway phase is obtained, when the threshold is set to the difference and we collect only the data at the time when the difference is smaller than the threshold. Automatically we can exclude the data which include the runaway phase by using this method. The difference between the time averages of phase is described by the following equation:

$$c(t) = \frac{1}{T_s}\int_{-\infty}^{\infty} Phase(t+\tau)h(\tau)d\tau. \tag{E.1}$$

Here

$$h(\tau) = \begin{cases} -1 & (-T_s \leq \tau < 0) \\ 0 & (\tau = 0) \\ 1 & (0 < \tau \leq T_s) \end{cases}, \tag{E.2}$$

and T_s is the time needed by the averaging. This equation has a form of convolution of the time evolution of phase, $Phase(\tau)$, and the kernel function, $h(\tau)$ [149, 150]. This means that Eq. E.1 can be used to classify the way of runaway phase by using various $h(\tau)$. It is an interesting extension, however we only use Eq. E.2 as $h(\tau)$ here.

Fig. E.1(a) and (b) show $Phase(t)$ and $c(t)$, respectively. $c(t)$ has a large value when the runaway phase occurs and is a good indicator of the runaway phase.

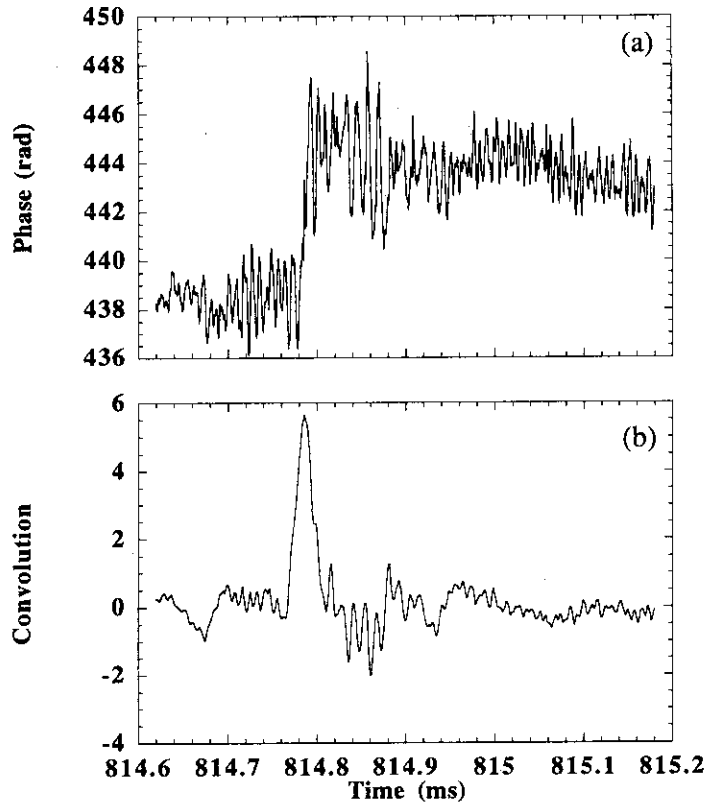

Figure E.1: (a) shows the time evolution of phase. The step-like runaway phase occurs at 814.79 ms. (b) shows the time evolution of $c(t)$. $T_s = 60\mu$s is selected as the result of some trials. The value is large when the phase suddenly increases. This shows that $c(t)$ is a good indicator of runaway phase phenomena.